
Measurement of the top quark mass using jet angles in the
lepton+jets $t\bar{t}$ decay channel with simulated $\sqrt{s} = 8$ TeV data of
the ATLAS experiment at the LHC

Messung der Top-Quarkmasse unter Verwendung von Zerfallswinkel
im lepton+jets $t\bar{t}$ -Zerfallskanal mit simulierten $\sqrt{s} = 8$ TeV Daten
des ATLAS Experiments am LHC



Masterarbeit an der Fakultät für Physik
der
Ludwig-Maximilians-Universität München

vorgelegt von

ANGELA MARIA BURGER

geboren in Landshut

München, den 30.03.2015

Gutachter: Prof. Dr. Otmar Biebel

Abstract

In the context of this Master's thesis, a new method for measuring the top quark mass with the ATLAS Experiment, using the lepton+jets $t\bar{t}$ decay, is introduced. The extraordinary high mass of the top quark, which is approximately 35 times the mass of its weak isospin partner, the bottom quark, raises questions and could give hints to possible new physics. Therefore, a precise knowledge of the top quark mass is important on the one hand to check the consistency of the Standard Model and on the other hand to check for signs of physics beyond the Standard Model.

Current measurements are already limited by systematic uncertainties and statistical uncertainties become less and less important because of the increasing size of datasets, in particular due to the "top factory" LHC. Therefore, a greater precision of the top quark mass measurement can only be achieved by either improving the understanding of the systematic uncertainties or by reducing the dependence of the top quark mass measurement on these uncertainties. One of the most dominant systematic uncertainty in the top quark mass measurement is the systematic uncertainty on the absolute Jet Energy Scale. It is difficult to determine the Jet Energy Scale experimentally. An approach to reduce this uncertainty is to make the top quark mass measurement as independent as possible on this contribution.

The analysis presented in this Master's thesis relies on the measurement of jet angles. Jet angles can be determined very precisely and the direction of the jets reflects very well the direction of the initial quark.

The invariant mass ratio of the reconstructed top quark and the W boson, $\frac{m_{\text{top}}}{m_W}$, can be evaluated by measuring the angles between the jets in the top quark rest frame only. However, the angles in the top quark rest frame cannot be measured directly as the top quarks are usually boosted with respect to the laboratory frame. Therefore, a small dependence on the jet energy remains due to the transformation of the measured jet angles to the angles in the top quark rest frame. In order to reduce the dependence on the jet energies, studies based on Monte Carlo simulations have been performed to investigate the functional dependence between the top quark mass estimator and the boost in order to extrapolate to the case of top quarks at rest. Subsequent studies on the method calibration are made in order to prepare the method for an application to 2012 ATLAS data with a center of mass energy of $\sqrt{s} = 8 \text{ TeV}$ and a luminosity of $\mathcal{L} = 20.3 \text{ fb}^{-1}$.

Contents

1. Introduction	6
2. Theoretical Framework of Top Quark Physics	8
2.1. Overview over the Standard Model	8
2.1.1. General Principles	8
2.1.2. The Particle Content of the Standard Model	9
2.2. Electroweak Theory	10
2.3. Quantum Chromodynamics	13
3. The Top Quark	15
3.1. Top Quark Production	15
3.1.1. Top Quark Production via the Strong Interaction	15
3.1.2. Electroweak Single Top Quark Production	16
3.2. Top Quark Decay	17
4. The Large Hadron Collider and the ATLAS experiment	21
4.1. The Large Hadron Collider	21
4.2. The ATLAS experiment	23
4.2.1. The ATLAS coordinate system	23
4.2.2. The inner detector	24
4.2.3. Calorimeters	25
4.2.4. The ATLAS muon system	26
4.2.5. The trigger	26
5. Physics Object Definition	27
5.1. Pile-up and Underlying Event	27
5.2. Electrons	28
5.3. Muons	29
5.4. Jets	29
5.4.1. Jet Object Definition	29
5.4.2. Jet Reconstruction Algorithm	30
5.4.3. The Jet Energy Scale	31
5.4.4. b-Tagging	32
5.5. Missing Transverse Energy	33
6. Simulated Data Sets	34
7. Event Selection and Reconstruction	35
7.1. Pre-Selection Cuts	35
7.2. Selection Cuts	36
7.3. Jet-Parton Matching	38
8. The Top Quark Mass Estimator $m_{\text{top}}^{\text{angle}}$	39

9. Monte-Carlo Studies on the Angle Method	42
9.1. The Functional Dependence of $m_{\text{top}}^{\text{angle}}$ on $\beta\gamma$	42
9.2. Analysis using low- $\beta\gamma$ Top Quarks	44
9.3. The Angle Method for Top Quarks with Non-Zero Boost	46
9.4. Studies on Parton Level	46
9.5. Analysis Strategy	51
9.6. Results Obtained with Jet-Parton Matched Objects	53
9.7. JSF-Variation Studies	56
10. Preparation of the Application of the Angle Method to ATLAS Data	57
10.1. Event Reconstruction Algorithm and Combinatorial Background	57
10.2. The adapted Top Quark Mass Estimator	61
10.3. Calibration of the Angle Method	67
10.4. Evaluation of the Uncertainty due to the Jet Energy Scale	73
10.5. Method Validation	74
11. Improving the Analysis Method	78
11.1. Improving the $t\bar{t}$ -pair Reconstruction Algorithm	78
11.2. The New Top Quark Mass Estimator	80
12. Conclusion and Outlook	87
A. The Crystal Ball Function	88
B. The Lorentz-Transformation	89

1. Introduction

The top quark is the heaviest quark as well as currently the heaviest known elementary particle in the Standard Model. The top quark mass is an important parameter of the Standard Model and a precise measurement on the one hand provides consistency checks of the value of other Standard Model parameters like the Higgs mass due to the relation of the top quark mass, the W-boson mass and the Higgs boson mass via loop contributions [1].

On the other hand, the precise determination of the top quark mass might lead to hints of new physics and the energy scale at which this new physics is expected: The shape of the Higgs potential depends very strongly on the value of the Yukawa-coupling y_t of the top quark to the Higgs field due to the relatively high value of y_t which is a consequence of the high mass of the top quark. Small variations of y_t might result either in a more stable Higgs-potential minimum at higher values of the Higgs-field or at no minimum at all. Our vacuum might thus only be meta-stable or even unstable according to the top quark mass. So its experimental and theoretical uncertainties matter. To make the Standard Model potentially consistent with observations, new physics might be necessary [2].

In 2014, the first world average of the top quark mass

$$m_{\text{top}} = 173.34 \pm 0.27(\text{stat.}) \pm 0.71(\text{syst.}) \text{ GeV.}$$

taking into account selected measurements from the ATLAS and CMS experiments at the LHC and the D0 and CDF experiments at the TEVATRON was published in [3].

With a total uncertainty of 0.76 GeV, the LHC and TEVATRON world average is as precise as 0.44%.

Most top quark mass measurements are dominated by systematic uncertainties. Statistical uncertainties become less and less an issue due to the increasing size of datasets which is a consequence of the increasing luminosity of the colliders and the increasing center-of-mass energy which implies a higher top quark production cross section.

One of the dominant contributions to the systematic uncertainty on the top quark mass measurement is the uncertainty on the jet energy scale i.e. the uncertainty on the conversion of a jet-induced signal in the detector to terms of energy taking into account background processes and modelling uncertainties but to name a few. Therefore, a special effort is directed towards decreasing that uncertainty. There are several approaches for example in-situ calibration of the jet energy scale using the mass of the hadronically decaying W-boson. Another possibility is to decrease the sensitivity of the measurement on the jet energies [1], the approach chosen in this analysis. This analysis method is thus complementary to other default methods of top quark mass determination.

This method can be assigned to the group of template methods. A variable which is sensitive to the top quark mass, the so-called estimator, is calculated and calibrated using Monte-Carlo simulations [1].

Applying geometrical considerations, it is possible to find a relation between $\frac{m_W}{m_{\text{top}}}$ and the angles between the top quark decay products. However, this relation is only valid in the top quark rest frame. Therefore, by transforming the system in the top quark rest

frame via a Lorentz transformation, a dependence on the jet energies is introduced. This dependence can be parametrized and the top quark mass estimator can be extrapolated to the case of top quarks at rest for which the method is found to be valid. Studies are performed regarding the feasibility of the method for $\sqrt{s} = 8 \text{ TeV}$ ATLAS data with an integrated luminosity of 20.3 fb^{-1} .

This thesis is organized as follows: In section 2 and 3, the underlying framework of top quark physics is introduced briefly, in section 4, the ATLAS experiment is described, section 5 gives details on the definition of physics objects and in section 6, the simulated datasets used for the analysis are described. In section 7, details on the reconstruction of the top quark and on the applied section cuts are given, section 8 motivates the estimator, the analysis using simulated data is described in section 9-11 and in section 12, a conclusion is provided.

2. Theoretical Framework of Top Quark Physics

2.1. Overview over the Standard Model

2.1.1. General Principles

The Standard Model of Particle Physics (SM) is a Quantum Field Theory. This states that all particles in the SM are associated with fields. Fields are required in order to explain creation and annihilation of particles and the non-conservation of particle numbers. This also implies that the principles of special relativity have to be valid, particularly, the conversion of energy to mass.

The Standard Model furthermore has to be Lorentz-invariant, this postulates that fundamental physics laws as for example momentum and energy conservation and the constancy of the speed of light have to be valid in all reference frames.

A crucial requirement on any predictable theory is renormalizability, which states that the predicted cross-sections and decay rates stay finite at all energies and if including higher-order corrections. Divergences can occur but it must be possible to absorb these in existing constants like masses or coupling constants [4].

The Standard Model is a gauge-theory, i.e. invariant under gauge-transformations. Interactions in the SM are a consequence of invariance under local phase transformations. Invariance under local phase transformation implies a conserved current in the interaction. In the SM, interactions are mediated by exchange bosons. These gauge bosons compensate the local phase shift introduced by the interaction.

Being an important principle, gauge-invariance should be demonstrated once at the example of QED (Quantum Electrodynamics) [5]. The Lagrangian of QED, the Dirac Lagrangian

$$\mathcal{L} = i\hbar c \bar{\psi} \gamma^\mu \partial_\mu \psi - mc^2 \bar{\psi} \psi \quad (1)$$

is invariant under a global phase transformation $\psi \rightarrow e^{i\theta} \psi$ where θ is a global phase shift. But, if introducing a local phase transformation, i.e. $\theta = \theta(x)$, an extra term is obtained and the Lagrangian becomes

$$\mathcal{L} \rightarrow \mathcal{L} - \hbar c (\partial_\mu \theta) \bar{\psi} \gamma^\mu \psi \quad (2)$$

and therefore, the Lagrangian is not locally gauge invariant which should hold if all interactions are independent on each other. This phase can be compensated by introducing a new field A_μ in the Lagrangian:

$$\mathcal{L} = [i\hbar c \bar{\psi} \gamma^\mu \partial_\mu \psi - mc^2 \bar{\psi} \psi] + \hbar c \bar{\psi} \gamma^\mu \psi A_\mu \quad (3)$$

The phase of A_μ is shifted as well if a local phase transformation occurs:

$$A_\mu \rightarrow A_\mu + \partial_\mu \theta(x) \quad (4)$$

Local gauge invariance of the Lagrangian can be achieved by introducing the covariant derivative and replacing the derivative ∂_μ in equation (1) by

$$\mathcal{D}_\mu \equiv \partial_\mu - iA_\mu \quad (5)$$

But the Lagrangian must also contain the free vector field A_μ which obeys the Proca equation, so the complete Lagrangian becomes:

$$\mathcal{L} = -\frac{1}{16\pi}F^{\mu\nu}F_{\mu\nu} + \frac{1}{8\pi}\left(\frac{m_A c}{\hbar}\right)^2 A^\nu A_\nu + [i\hbar c\bar{\psi}\gamma^\mu\partial_\mu\psi - mc^2\bar{\psi}\psi] + \hbar c\bar{\psi}\gamma^\mu\psi A_\mu \quad (6)$$

Note that (6) is not invariant under local phase transformation. It is only locally phase invariant if the mass of the vector field m_A equals 0. Therefore, local phase invariance can be achieved but only if the gauge boson mediating the interaction is massless [5]. This can also be understood intuitively, if requiring that a local phase transformation has to be compensated in the entire universe and only a massless particle has infinite reach [6]. Gauge bosons are not necessarily massless. Therefore a mechanism needs to be introduced in order to make the observations consistent with theory.

Interactions are described as rotations in abstract space and conserved quantities, as required in a locally gauge-invariant theory, are invariant under a rotation in the corresponding space. The description of the SM is based on the symmetry group $SU(3)_C \times SU(2)_L \times U(1)_Y$. The first term represents a rotation in colour space which is described by Quantum-Chromodynamics (QCD) and $SU(2)_L \times U(1)_Y$ describes a unified electroweak theory of QED and the weak interaction. The subscript L denotes that the weak force only acts on left-handed particles, and Y the charge which the boson of $U(1)$ couples to [6].

2.1.2. The Particle Content of the Standard Model

There are two kinds of elementary particles which matter is made of in the Standard Model: quarks and leptons. Both are fermions, spin 1/2-particles. The particles can be ordered into three so-called families consisting each of 2 quarks and two leptons (see Fig. 1).

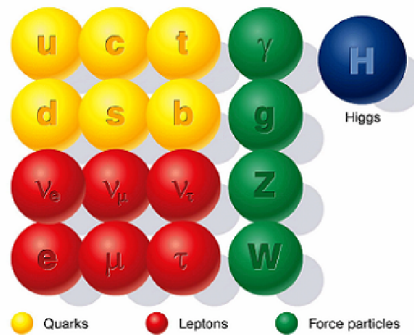


Figure 1: Overview over the matter and force particles of the Standard Model. From [7].

Each family contains a onefold charged lepton and a neutral lepton, called neutrino. According to the original concept of the Standard Model, neutrinos are considered massless

Generation	Flavour	Charge [e]	Mass [MeV]
1st	up (u)	+2/3	$2.3^{+0.7}_{-0.5}$
	down (d)	-1/3	$4.8^{+0.5}_{-0.3}$
2nd	charm (c)	+2/3	1275 ± 25
	strange (s)	-1/3	95 ± 5
3rd	top (t)	+2/3	$173340 \pm 270(\text{stat.}) \pm 710(\text{sys.})$
	bottom (b)	-1/3	4180 ± 30

Table 1: Quarks and their properties. Data extracted from [8], top quark mass from [3].

Generation	Flavour	Charge [e]	Mass [MeV]	Lepton Number
1st	e (electron)	-1	$0.510998928 \pm 0.000000011$	$L_e = 1$
	ν_e	0	≈ 0	$L_e = 1$
2nd	μ (muon)	-1	$105.6583715 \pm 0.0000035$	$L_\mu = 1$
	ν_μ	0	≈ 0	$L_\mu = 1$
3rd	τ (tau)	-1	1776.82 ± 0.16	$L_\tau = 1$
	ν_τ	0	≈ 0	$L_\tau = 1$

Table 2: Leptons and their properties. From [8].

and furthermore, a lepton number conservation holds within each lepton family. Quarks have non-integer charge and each family contains one quark of charge +2/3 and one quark of charge -1/3, adding up in total to 6 so-called quark-flavours. Besides from the matter particles, there are force fields represented by integer-spin particles: bosons. These particles mediate the fundamental forces in the SM: the electromagnetic interaction, mediated by the massless photon, the weak interaction, mediated by the W^\pm and the Z-boson, the strong force, mediated by the massless gluon and the scalar Higgs-field providing the particles with masses [5].

The particles of the SM and their properties can be extracted from Tab. 1 (quarks), Tab. 2 (leptons) and Tab. 3 (gauge bosons). Note that a corresponding antiparticle exists for each of the quarks and leptons. Their charge-like quantum numbers differ by sign.

2.2. Electroweak Theory

The electroweak theory comprises the weak and the electromagnetic interaction to one unified theory. The weak interaction couples to all particles carrying weak force, that is, all quarks and leptons and the electromagnetic force couples to all particles carrying charge. It has been shown by C.S. Wu in her famous experiment [9], that weak interactions are parity-violating: only left-handed particles and right-handed antiparticles couple to the weak force. Massive particles can be regarded as mixture of right and left handed components whereas massless particles can only occur as either right- or left-handed particles.

Gauge Boson	Mediated Force	Charge [e]	Spin	Mass [GeV]	Couples to
photon (γ)	electromagnetic	0	1	0	all charged particles
W^\pm	weak	± 1	1	80.385 ± 0.015	all quarks and leptons, itself, Z-boson, photon, Higgs
Z-boson	weak	0	1	91.1876 ± 0.0021	all quarks and leptons, itself, W-boson, Higgs
gluon	strong	0	1	0	all quarks, itself
Higgs	-	0	0	125.7 ± 0.4	all particles carrying mass, itself

Table 3: Gauge bosons and their properties. From [8] and [6].

A consequence of lepton number conservation is that in the perspective of the weak interaction, leptons of one family are doublets under the weak interaction. The underlying symmetry of weak interaction is therefore SU(2) [6]. It was shown by Yang and Mills, that the introduction of 3 massless gauge fields $\mathbf{W}_\mu = (W_\mu^1, W_\mu^2, W_\mu^3)$ is necessary to describe a local gauge-invariant SU(2) theory [5]. These fields compensate any local phase transformation caused by the weak interaction.

Furthermore, it has been shown that weak and electromagnetic interaction cannot be treated as separate theories. At some energy, their coupling strengths are equal and their symmetry is just broken at low energies. The underlying symmetry of the electromagnetic theory is U(1)_{em}, the gauge boson of U(1)_{em} is the photon, and the conserved quantity as consequence of invariance under phase transformation is the electric charge. The symmetry of the unified electroweak theory was found to be SU(2)_L × U(1)_Y. This symmetry is spontaneously broken at low energy which results in the formation of W^\pm , Z^0 and γ . The SU(2)_L W_μ^3 -boson mixes with the B-boson to generate physically observable gauge bosons, the photon and the Z-boson. W_μ^1, W_μ^2 mix and form the two bosons W^\pm :

$$W_\mu^\pm = \frac{1}{\sqrt{2}}(W_\mu^1 \mp iW_\mu^2) \quad (7)$$

$$A_\mu = B_\mu \cos(\theta_W) + W_\mu^3 \sin(\theta_W) \quad (8)$$

$$Z_\mu = -B_\mu \sin(\theta_W) + W_\mu^3 \cos(\theta_W) \quad (9)$$

where θ_W is the weak mixing angle which is measured experimentally to 28.75° . The hypercharge Y is defined by

$$Y = 2 \cdot (Q - T_3) \quad (10)$$

where Q is the electric charge and T_3 is the third component of the weak isospin [5].

The complete Lagrangian of the electroweak interaction is given by

$$\begin{aligned}
 \mathcal{L} = & -\frac{1}{4}W_{\mu\nu}^i W_i^{\mu\nu} - \frac{1}{4}B_{\mu\nu}B^{\mu\nu} + \\
 & \bar{\psi}_L(i\gamma^\mu\partial_\mu - g_W\frac{\tau_i}{2}\gamma^\mu W_\mu^i - g'\frac{Y}{2}\gamma^\mu B_\mu)\psi_L + \\
 & \bar{\psi}_R(i\gamma^\mu\partial_\mu - g'\frac{Y}{2}\gamma^\mu B_\mu)\psi_R
 \end{aligned}
 \tag{11}$$

where $W_{\mu\nu}$ and $B_{\mu\nu}$ are the field strength tensors of SU(2) and U(1) respectively. The first and the second term represent the free gauge fields. g_W is the coupling strength of the SU(2) gauge fields and g' the coupling constant to the U(1) field and τ_i , $i \in \{1, 2, 3\}$ represent the Pauli spin matrices. The W_μ^i fields, the gauge fields of SU(2), only couple to the left-handed chiral component of the fermionic fields ψ , indicated by the subscript L in equation 11 while the B_μ fields couple to both left- and right-handed chiral states with a strength proportional to the particle's hypercharge Y [10].

But, as it turned out, in contrary to the requirements stated in section 2.1.1, the gauge bosons W and the Z have a mass (see table 3). Therefore, it is necessary to introduce a mechanism which endows the exchange bosons with mass, commonly referred to as the Higgs-mechanism.

A scalar boson field potential with a symmetric ground-state such as in Fig. 2 is postulated. The vacuum expectation value has to take a value unequal to zero. Then, if the system chooses one specific ground-state, the symmetry is broken. If additionally requiring local gauge invariance, the vector bosons acquire masses [5].

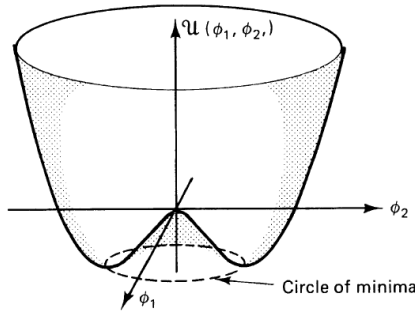


Figure 2: The Higgs potential, from [5].

While lepton flavour is conserved in the weak interaction, quark flavour is not. In fact, flavour mixing is possible by coupling to the W-boson, the degree of mixing is described by the CKM-Matrix:

$$\begin{pmatrix} d' \\ s' \\ b' \end{pmatrix} = \begin{pmatrix} V_{ud} & V_{us} & V_{ub} \\ V_{cd} & V_{cs} & V_{cb} \\ V_{td} & V_{ts} & V_{tb} \end{pmatrix} \begin{pmatrix} d \\ s \\ b \end{pmatrix} = \begin{pmatrix} 0.974 & 0.227 & 0.004 \\ 0.227 & 0.973 & 0.042 \\ 0.008 & 0.042 & 0.999 \end{pmatrix} \begin{pmatrix} d \\ s \\ b \end{pmatrix}$$

The pairs

$$\begin{pmatrix} u \\ d' \end{pmatrix}, \begin{pmatrix} c \\ s' \end{pmatrix}, \begin{pmatrix} t \\ b' \end{pmatrix}$$

are doublets with respect to the weak interaction but d' , s' and b' are linear combinations of quarks given by the CKM-Matrix [5].

The absolute values of the matrix elements V_{td} , V_{ts} and V_{tb} are a measure of the couplings of the top quark to the up, strange and b-quark, respectively. Note that a decay of the top quark to an up-type quark like itself is not possible as there are no flavour-changing neutral currents. The matrix element V_{tb} is nearly unity and all the other elements are very small compared to V_{tb} . As a consequence, in almost all cases, the top quark decays to a b-quark, effects from decays to other down-type quarks are negligible.

2.3. Quantum Chromodynamics

Experiments (for examples, see [6]), have shown, that quarks carry three colours, namely "red", "green" and "blue" and the corresponding anticolours. Colour is a conserved quantity in QCD and interactions are regarded as rotations in 3-dimensional colour space. The relevant symmetry is SU(3) due to which 8 gauge bosons which are called gluons are introduced [4]. The QCD-Lagrangian denotes to

$$\mathcal{L}_{\text{QCD}} = \bar{\psi}(i\gamma_{\mu}D^{\mu} - m)\psi - \frac{1}{4}G_{\mu\nu}^{\vec{\lambda}}G^{\mu\nu\vec{\lambda}} \quad (12)$$

where $D_{\mu} = \partial_{\mu} + \frac{1}{2}ig_s\vec{\lambda}\vec{G}_{\mu}$ is the covariant derivative analogously to equation (5) with g_s , the strong coupling constant, $\vec{\lambda}$, the generators of SU(3) which are the Gell-Mann-Matrices and $G^{\mu\nu}$, the gluon field strength tensor (see [5] and [6]).

In the Yang-Mills theory, gauge boson-self interaction is a consequence of the non-abelian nature of the underlying symmetry group [5]. The gluons therefore can couple to each other and they themselves carry colour-charge. In fact, in a gluon-radiation process such as $q \rightarrow q + g$, the colour-charge of the quark can change. But as interactions in QCD are colour-conserving, the gluon has to carry two colour-charges [5]. Out of the nine possible colour-anticolour combinations¹, 8 have a net-colour charge and one is a colour-neutral singlet ($\frac{1}{\sqrt{3}}(r\bar{r} + b\bar{b} + g\bar{g})$) [5].

Renormalizability requires that divergences issuing from intermediate virtual states can

¹ $\frac{1}{\sqrt{2}}(r\bar{b}-b\bar{r})$, $\frac{-i}{\sqrt{2}}(r\bar{g}-g\bar{r})$, $\frac{1}{\sqrt{2}}(r\bar{g}+g\bar{r})$, $\frac{1}{\sqrt{2}}(b\bar{g}+g\bar{b})$, $\frac{-i}{\sqrt{2}}(b\bar{g}-g\bar{b})$, $\frac{-i}{\sqrt{2}}(r\bar{b}-b\bar{r})$, $\frac{1}{\sqrt{2}}(r\bar{r}-b\bar{b})$, $\frac{1}{\sqrt{6}}(r\bar{r}+b\bar{b}-2g\bar{g})$ [5].

be absorbed by a constant. As a consequence, the coupling constant of the strong interaction, α_s depends on the momentum transfer. Additional self-coupling causes the potential to decrease at short distances or high momentum transfer and to increase at large distances or small momentum transfer [5]. Equation (13) shows the behaviour of the strong coupling constant α_s with the momentum transfer Q .

$$\alpha_s = \frac{12\pi}{(33 - 2N_f)\ln(\frac{Q^2}{\Lambda^2})}(1 + \dots) \quad (13)$$

where N_f is the number of accessible quark flavours for the momentum transfer ($2m_f < |Q|$) and Λ is a free parameter [6].

At high momentum transfer or short distances, the quarks behave like free particles, as the case in hadrons. This is called asymptotic freedom.

At low Q^2 or long distances, the states of quarks are governed by confinement. A single quark cannot be observed but only colourless states (either color-anticolour or $g+b+r$, or $\bar{g} + \bar{b} + \bar{r}$) resulting in mesons (quark-antiquark) or baryons (3 quarks).

If a quark-antiquark pair (like in Fig. 3) is created in an interaction, they will fly apart but their potential energy increases with distance and new quark-antiquark pairs are produced which form bound states, hadrons. Therefore, the typical signature of quark production are jets of hadrons. This process is called hadronization [5].

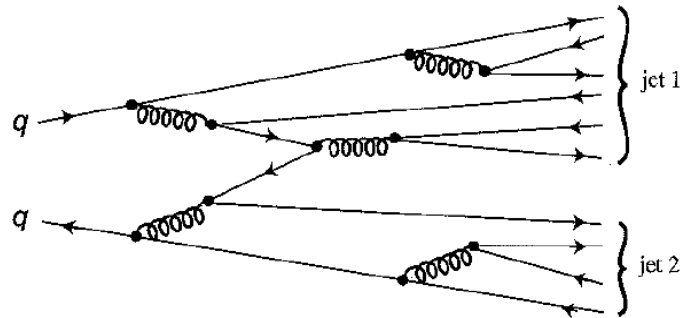


Figure 3: Illustration of hadronization. From [5].

3. The Top Quark

Top quark production proceeds mainly via two processes: Top quark pair production mediated by the strong interaction and single-top production mediated by the charged-current weak interaction. Top quarks are heavy compared to the other quarks and therefore, a higher center-of-mass energy (cms) is necessary to produce them at a collider. Additionally, in proton-proton colliders, the top quarks are produced out of the partons in the proton which only carry a fraction of the proton's energy. The first collider capable of producing top quark was the proton-antiproton collider TEVATRON with a cms energy of 1.8 TeV in Run 1. The production cross section rises with increasing cms energy and thereby the number of produced top quarks [1].

The LHC with a center of mass energy of $\sqrt{s} = 8 \text{ TeV}$ in 2012 provides thus the ideal environment for studying top quarks. In this section, the production and decay channels of the top quark at the LHC are presented.

3.1. Top Quark Production

3.1.1. Top Quark Production via the Strong Interaction

In this Master's thesis, the top quark mass is measured with top quarks produced by the strong interaction. The production mechanism via the strong interaction is much more likely as the value of the coupling constant of the strong interaction is much higher than of the weak coupling constant and the masses of the bosons mediating the weak force are very massive. The leading-order diagrams of the $t\bar{t}$ -production at a proton-proton collider like the LHC are shown in Fig. 4.

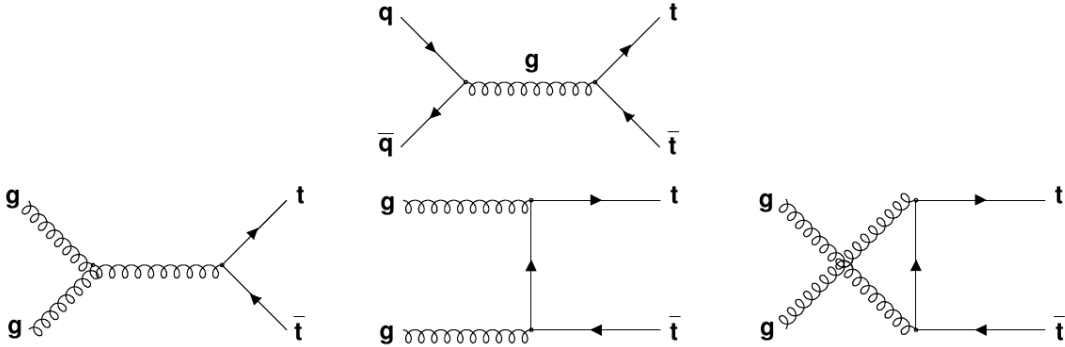


Figure 4: Leading-order diagrams of $t\bar{t}$ -pair production at proton-proton colliders via the strong interaction. From [1].

The upper diagram in Fig. 4 is the Feynman-diagram corresponding to the process $q\bar{q} \rightarrow t\bar{t}$, the annihilation of a quark-antiquark pair into a gluon which subsequently decays into a $t\bar{t}$ -pair. The lower diagrams correspond to the gluon-gluon-fusion process, $gg \rightarrow t\bar{t}$. In case of the LHC with a center-of-mass energy of $\sqrt{s} = 8 \text{ TeV}$, the gluon-fusion

dominates the $t\bar{t}$ -production. This can be motivated by the proton parton distribution function (PDF) shown in Fig. 5.

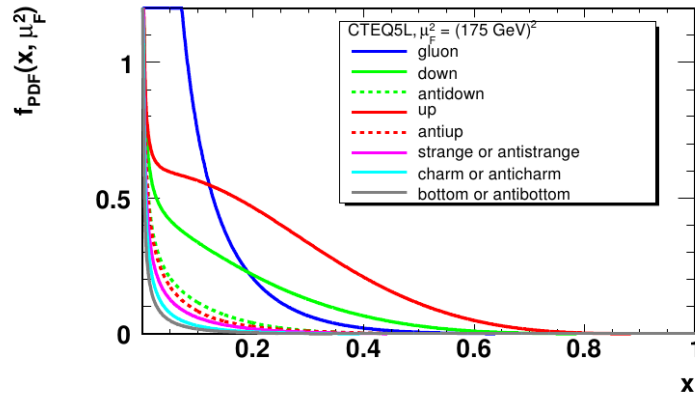


Figure 5: Parton distribution function (PDF) of the proton. From [1].

The partons in the protons each carry only a fraction of the proton momentum. The PDF illustrates the distribution of the hadron momentum fraction x among the partons. In order to produce a $t\bar{t}$ pair, the kinematic condition

$$x_i \cdot x_j \geq \frac{4m_{\text{top}}^2}{s} \quad (14)$$

has to be fulfilled where x_i and x_j denote the energy fraction of the interacting partons with respect to the proton energy and s the cms energy of the collider squared [11]. The LHC collided protons with a cms energy of $\sqrt{s} = 8 \text{ TeV}$ in 2012, thus, the cms energy exceeds the top quark mass ($m_{\text{top}} \approx 173 \text{ GeV}$) by a magnitude. The factor $x_i \cdot x_j$ yields $\approx 2 \cdot 10^{-3}$, so, typically x_i and x_j take values of the order of < 0.1 . The gluon PDF at these small momentum fractions (indicated as "x" in Fig 5) is much larger than the PDF amplitude of the other partons, therefore, the probability of two gluons with small energy fusing is much larger than of other partons [12],[1].

3.1.2. Electroweak Single Top Quark Production

Another possibility to produce top quarks is the single-top production via the electroweak interaction. There are three different production channels in electroweak single-top production. These channels are illustrated in Fig. 6.

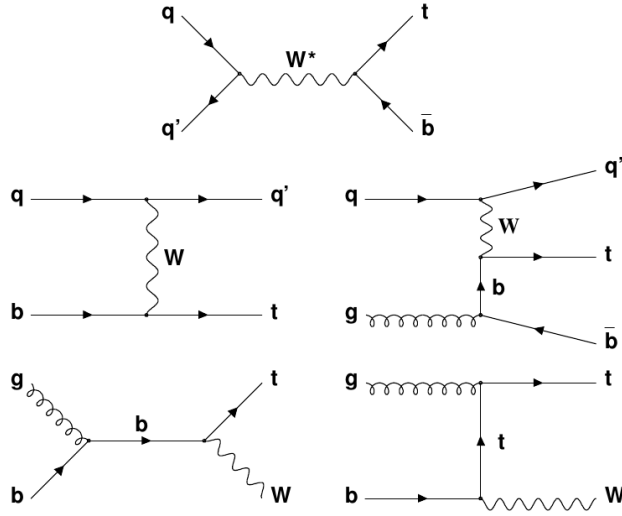


Figure 6: Processes leading to single-top production. Upper panel: s-channel, center: t-channel and bottom panel: associated Wt -production. From: [1]

Single-top production can proceed via the annihilation of two quarks of the same isospin doublet into a W -boson (s-channel, see Fig. 6,top) or when a virtual W -Boson interacts with a sea- b -quark inside the proton whereas the b -quark inside the proton is generated by a gluon splitting into a $b\bar{b}$ -pair (t-channel, Fig. 6, center). In the third possible process, called the associated Wt production, shown in Fig. 6, bottom panel, a top quark and a W -boson are produced when a gluon excites a sea-bottom-quark.

In proton-proton collisions mostly up- and down-quarks coupling to the W -Boson contribute to single-top production but there's also a small contribution from quarks of the second family. At the LHC, the t-channel single-top production is the dominant single-top-production channel [13].

Single-top production was already observed at the TEVATRON but its properties can be measured in detail for the first time at the LHC (see for instance [14]). Its cross section is notably lower than strong top-pair production. For details, see [1].

3.2. Top Quark Decay

In almost all cases, the top quark decays into a b -quark and a W -boson. Decays to lighter quarks (s- or d-quarks) are possible but not very likely, the corresponding CKM-matrix elements, V_{ts} and V_{td} are very small compared to V_{tb} (see section 2.2). Top quarks are the only quarks which do not form hadrons, their lifetime is smaller than the time it takes to form bound states. Consequently, top quarks decay via the weak interaction before they can form hadrons.

Within the scope of this thesis, the top quark mass measurement is performed by examining $t\bar{t}$ decays. Therefore, in the following, the possible decay topologies of $t\bar{t}$ pairs are discussed. As the top quark almost exclusively decays into a W -boson and a b -quark,

the event topology of the $t\bar{t}$ decay depends on the decay modes of the ensuing decay of the two W-bosons: The W-boson can either decay to a lepton and the corresponding neutrino or to a quark-antiquark pair. Hence, three decay modes are possible: the dileptonic decay, the lepton+jets decay and the all-hadronic decay channel [1]. The branching ratio of the $t\bar{t}$ decay can be extracted from Fig. 7.

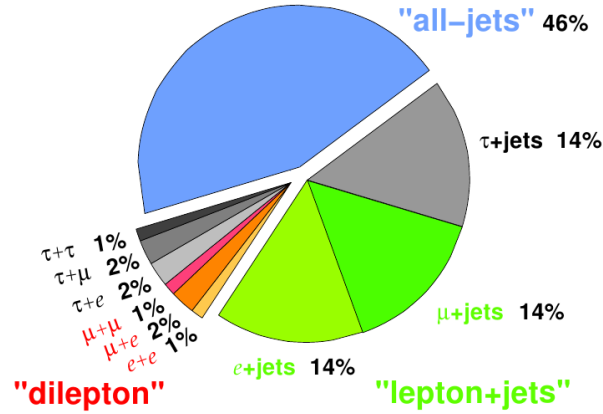


Figure 7: Branching ratio of the decay channels of the $t\bar{t}$. From [1].

The dileptonic channel In case of a dileptonic decay, both W-bosons decay leptonically, emitting each a charged lepton and the corresponding neutrino or antineutrino resulting in an event signature of $t\bar{t} \rightarrow W^+bW^-b \rightarrow l\nu_l b\bar{l}\bar{\nu}_l\bar{b}$. An illustration of the dileptonic decay can be seen in Fig. 8.

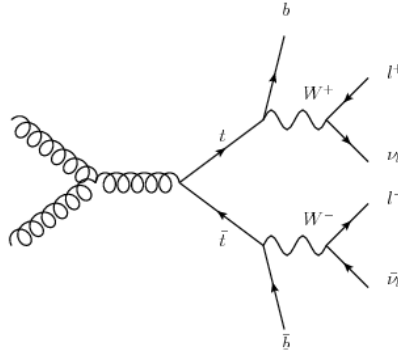


Figure 8: Dileptonic $t\bar{t}$ decay. From: [15].

Thus, the signature of the dileptonic channel are two oppositely charged leptons, two energetic b-jets and missing transverse energy issuing from the neutrinos. Note that lepton means either an electron or a muon, tau-leptons are not considered in most standard analyses in the dileptonic and neither in the lepton+jets decay channel. This

analysis excludes decays of the W-boson to tau leptons as well. Due to their decay, they introduce additional neutrinos [1] and moreover, tau-leptons are difficult to identify as they further decay [12].

The dileptonic decay constitutes about 5% of all top-pair decays [1].

The lepton+jets channel If one of the W-bosons from the top pair decay decays into one lepton and the corresponding neutrino and the other W-boson decays into a quark-antiquark-pair, the decay is assigned to the lepton+jets $t\bar{t}$ decay channel. An example of the topology of this decay, $t\bar{t} \rightarrow W^+bW^-\bar{b} \rightarrow q\bar{q}'b\bar{b} + \bar{l}\nu_l b q \bar{q}'\bar{b}$, which has a branching ratio of 29%, is illustrated in Fig. 9.

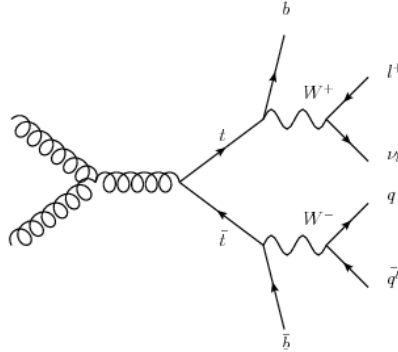


Figure 9: An example of the event topology of the lepton+jets decay. From [15].

Consequently, the event signature is one energetic and isolated lepton and missing transverse energy from the neutrino and in total four energetic jets of the hadronic W-decay and of the two b-quarks of the top quark decay [1].

The all-hadronic channel In 46% of all cases, both W-bosons decay hadronically resulting in an event signature consisting of 6 energetic jets, no charged leptons and no significant missing transverse energy. Thus, the topology of this decay with the highest branching ratio is $t\bar{t} \rightarrow W^+bW^-\bar{b} \rightarrow q\bar{q}'bq''\bar{q}'''\bar{b}$. An illustration of the all-hadronic top quark decay can be seen in Fig. 10.

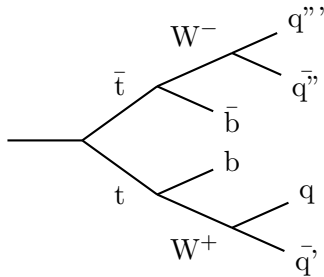


Figure 10: All-hadronic $t\bar{t}$ decay.

Discussion of Top Quark Mass Measurements in the Top Pair Decay Channels The lepton+jets $t\bar{t}$ decay channel provides the best trade-off between a reasonably large branching ratio and a low background fraction [11]. Physics background, events with the same event signature as the signal, is mainly caused in this channel by W+jets events with a leptonically decaying W-boson produced in association with 4 jets and by single-top events [16].

On the one hand, the dileptonic decay has a very low branching ratio but on the other hand, the signal purity is high due to the clear signal in the detector and the low physics background. But as the event kinematic is under-constrained due to the two neutrinos leaving the detector undetected, the event cannot be reconstructed easily [1]. Therefore, the top quark mass in this channel is preferably measured using estimators which do not require a full reconstruction of the $t\bar{t}$ event, see for example [17] and [18].

The all-hadronic decay channel is particularly difficult to analyse in spite of its large branching ratio. The signature of this decay are 6 jets, therefore, background mainly issues from multijet events. But the multijet production cross section is orders of magnitude larger than the signal [11]. Moreover, the multijet background is very difficult to model with Monte-Carlo simulations [1]. For a top quark measurement in this channel, see for instance [11].

This analysis is performed using the lepton+jets $t\bar{t}$ decay channel. The branching ratio is reasonably large resulting in data samples of reasonable size and the top pair can be fully reconstructed which is necessary for this approach as angles have to be measured.

4. The Large Hadron Collider and the ATLAS experiment

The Large Hadron Collider (LHC) is the world's largest circular particle accelerator and collider and is situated at CERN (European Organization for Nuclear Research), Geneva. Proton-proton collisions at unprecedented energy and luminosity happen at the location of the four affiliated detectors ATLAS, CMS, ALICE and LHCb. These experiments probe the building blocks of matter and the fundamental forces between them, pursue the discovery of new particles as well as a precise measurement of the Standard Model of particle physics. Due to the high luminosity of the LHC, processes and new particles can be discovered and investigated which were inaccessible before due to their low cross-section [19]. This section provides an overview of the LHC and the ATLAS experiment whose data were analysed for this thesis.

4.1. The Large Hadron Collider

The LHC, a circular proton-proton collider of 27 km circumference, is the last stage of a series of accelerators (see Fig. 11).

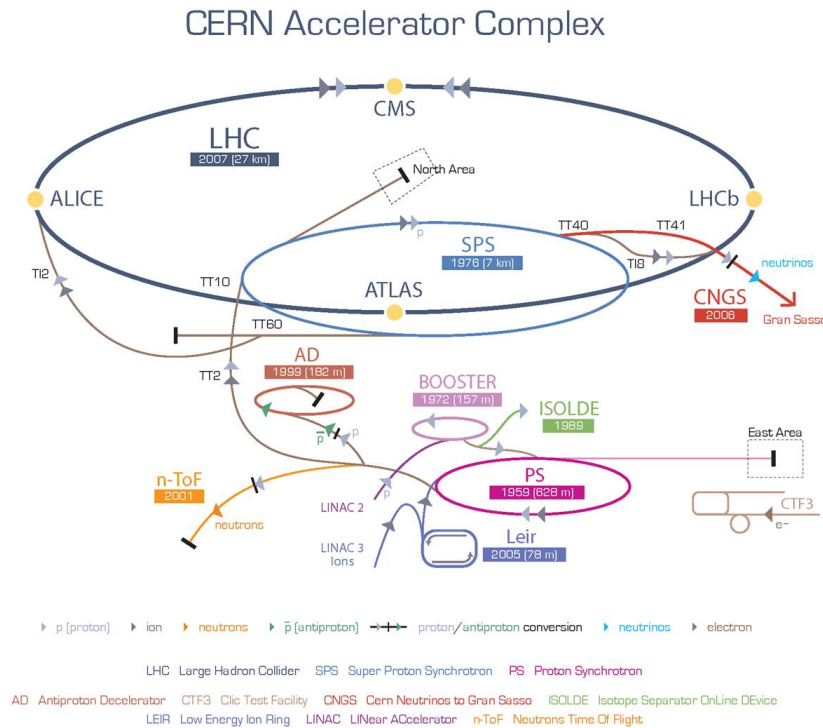


Figure 11: The Large Hadron Collider LHC (dark blue) with its pre-accelerators and affiliated experiments, from [20].

The protons enter the ring after having been accelerated to an energy of 450 GeV by

the pre-accelerators LINAC2, PSB, PS and SPS (see Fig. 11) [21]. In the LHC itself, the proton energy is increased from 450 GeV to 4 TeV, resulting in a center-of-mass energy (cms) of 8 TeV in 2012. The design energy of the LHC is 14 TeV and the design luminosity $10^{34} \frac{1}{\text{cm}^2\text{s}}$. The collider is operated at these beam parameters after the long shut-down LS1 which ends in 2015.

The acceleration is achieved using a radio-frequency acceleration system. The proton beams are kept on their circular path by dipole magnets and focussed by quadrupole magnets along the beam pipe. Due to the high beam energy, a high magnetic field of 8.4 T is necessary which can only be achieved using superconducting magnets. These require a cooling to a temperature of 2 K with superfluid helium. Two beam channels are contained by an iron yoke, the protons run clockwise in one pipe and counter-clockwise in the other pipe. The profile of such a dipole magnet containing the beam pipes is illustrated in Fig. 12.

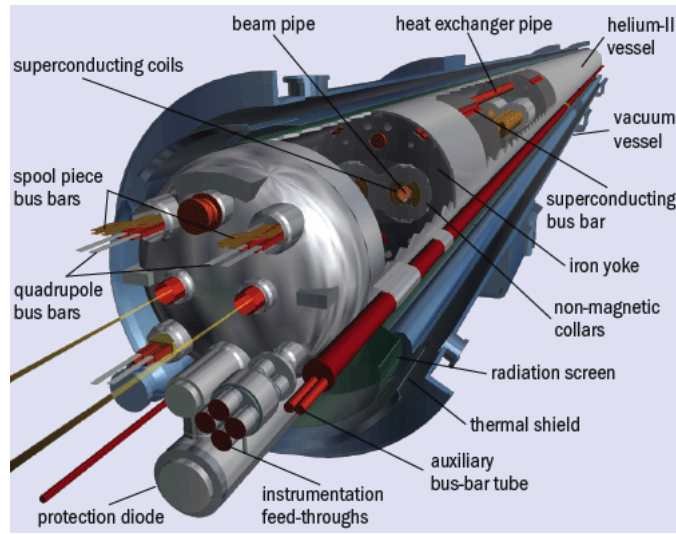


Figure 12: Profile of a LHC dipole magnet. The beam pipes are indicated in bright red. From [22].

The beams cross where the four experiments are located: ATLAS (A Toroidal LHC ApparatuS), CMS (Compact Muon Solenoid), ALICE (A Large Ion Collider Experiment) and LHCb (Large Hadron Collider beauty). CMS and ATLAS are multi-purpose detectors whereas LHCb is specialized on b-quark physics and ALICE investigates heavy-ion-collisions: Not only protons can be collided within the LHC but also lead nuclei [23]. The LHC started operating in 2008 and first collisions at a center-of-mass energy of 7 TeV were initiated in 2010. The center-of-mass energy was increased in 2012 to 8 TeV [24]. The studies in this thesis were performed with Monte-Carlo generated events simulating collisions in the ATLAS detector at 8 TeV.

In 2012 a long shut-down period began, the LHC will be restarted in spring 2015 operating at a cms energy of 13 TeV [25].

4.2. The ATLAS experiment

The ATLAS detector is a multi-purpose detector designed to identify and measure the energy and momenta of all hadronic jets, leptons and photons issuing from inelastic collisions between two partons of the protons. Missing transverse energy, energy of particles which cannot be detected, can be calculated by requiring momentum balance in transverse direction.

The detector is forward-backward symmetric with respect to the collision point and all detector components cover the complete solid angle in order to detect all particles produced in the inelastic collision.

The ATLAS detector is located in a cavern 100 m under the surface. Its shape is cylindrical with a central barrel and end-caps perpendicular to the beam axis. ATLAS is 44 m long and has a diameter of 25 m. A cut-away view of ATLAS can be seen in Fig. 13.

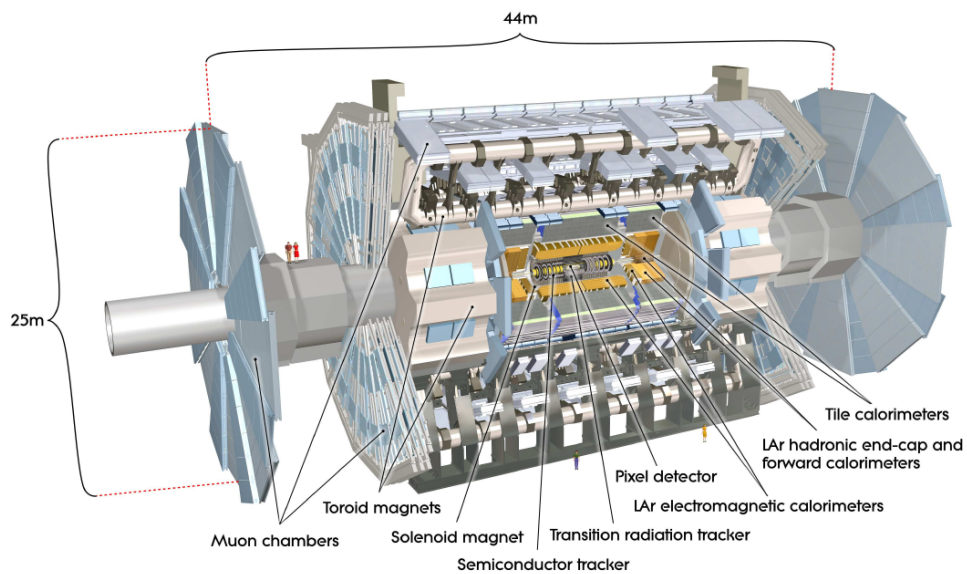


Figure 13: Illustration of the ATLAS detector and its components. From [19].

To examine in detail the entire process happening after an inelastic collision and the particles involved, ATLAS consists of several detector layers with complementary purposes [19]. In the following subsections, a short overview on the detector parts is given.

4.2.1. The ATLAS coordinate system

Coordinates in the ATLAS detector are defined as illustrated in Fig. 14.

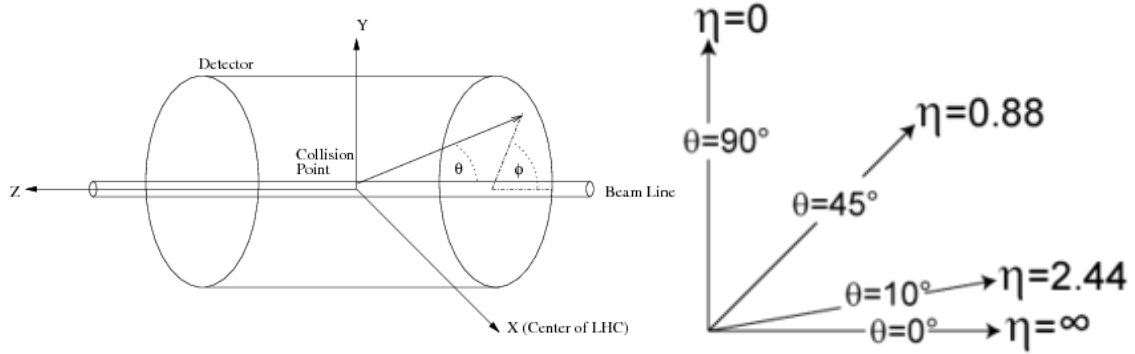


Figure 14: Left panel: Schematic illustration of the ATLAS coordinate system and the assignment of the coordinates Φ (azimuth angle), θ (polar angle) and z (longitudinal direction). Instead of the polar angle θ , the polar coordinate is commonly expressed in terms of the pseudorapidity η (see text) [26]. The η coordinate is visualized in the right panel [27].

The interaction point of the proton beams constitutes the origin of the coordinate system. The direction of the beam pipe is defined as the z -axis. The polar angle θ is the angle between the beam pipe. The pseudorapidity η is defined as $\eta = -\ln \tan \frac{\theta}{2}$ in case of massless particles and as $y = \frac{1}{2} \frac{E+p_z}{E-p_z}$ in case of massive particles and the angle Φ , the azimuthal angle, is the angle around the beam pipe. Distances ΔR between two objects are calculated using the relation $\Delta R = \sqrt{(\Delta\eta)^2 + (\Delta\Phi)^2}$.

In terms of a cubic coordinate system with coordinates (x,y,z) , z is, as before, defined as the direction of the beam axis, y is pointing upwards and x is pointing towards the centre of the LHC. Important quantities are the transverse momentum p_T and energies E_T of objects which are measured in the x,y -plane [19].

4.2.2. The inner detector

In the inner detector, momentum and vertex measurements are performed, tracks are recognized and electrons are identified. For these purposes, the inner detector consists of semiconductor pixel, silicon microstrip trackers (SCT) in the pseudorapidity region $|\eta| < 2.5$ and transition radiation tracker straw tubes (TRT) (up to $|\eta| = 2.0$).

The tracks of particles can be reconstructed using the coordinate information provided by the hit information in the pixel, SCT and TRT detectors and momentum measurement is possible due to the bending of tracks of charged particles by the magnetic field of 2 T produced by the solenoid magnet surrounding the inner detector [19]. In addition to tracking, the TRT is also able to identify electrons by detecting the transition radiation caused by electrons crossing the TRT [28]. The pixel and SCT detectors are allocated on concentric cylinders around the beam axis in the barrel and in the end-caps in discs perpendicular to the beam axis. The straw tubes of the TRT are parallel to the beam axis in the barrel and are mounted radially in the end-caps [19]. Fig. 15(a) shows a schematic view of the inner detector.

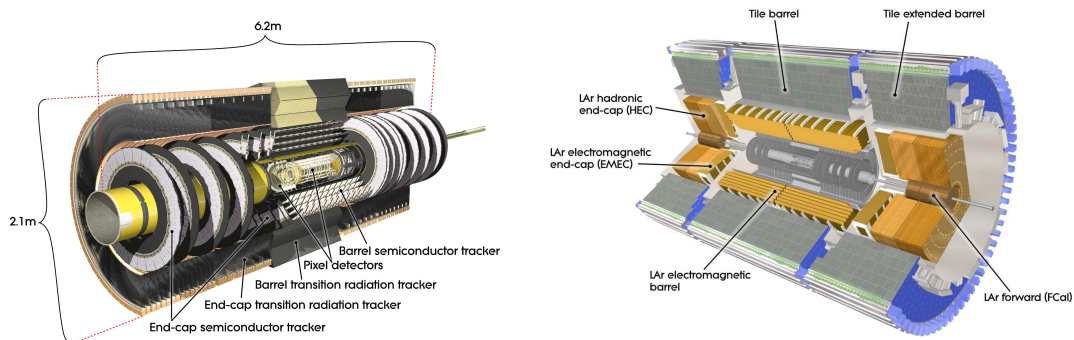


Figure 15: Left panel: The Inner Detector containing Semiconductor Pixel and Microstrip Trackers and Transition radiation tracker straw tubes. Right panel: Illustration of the ATLAS calorimeters. In yellow: Electromagnetic Calorimeter, in gray: Hadronic Calorimeter. From [19].

4.2.3. Calorimeters

ATLAS comprises an electromagnetic calorimeter and a hadronic calorimeter (illustration see Fig. 15(b)). The fine-grained liquid-argon (LAr) electromagnetic calorimeter surrounds the solenoid magnet in the barrel ($|\eta| < 1.475$) and has also a component in the end-caps covering the range $1.375 < |\eta| < 3.2$. The sampling calorimeter with lead as absorber and liquid argon as detection material performs precision measurement on position and energy of photons and electrons.

The more coarse grained hadronic calorimeter reconstructs jets and measures their energy. With its depth of 9.7 interaction length² (10 interaction length in the end-caps), it ensures a good energy resolution for high-energetic jets. Like the electromagnetic calorimeter, the hadronic calorimeter is a sampling calorimeter: The barrel hadronic calorimeter ($|\eta| < 1.7$) uses steel as absorber material and scintillating tiles as detector material whereas the hadronic end-cap calorimeter ($1.5 < |\eta| < 3.2$) installed directly behind the end-cap electromagnetic calorimeter consists of copper absorber with gaps in between for liquid argon for detection.

The ATLAS sampling calorimeters allow for a simultaneous measurement of the particle energy and position of leptons or hadronic jets [19]. Interaction with the absorbing material causes secondary particles in inelastic nuclear processes (hadrons), pair production and Compton scattering (photons) and bremsstrahlung (charged particles) to name just a few, which are then detected by the active material [30].

²The nuclear interaction length is given by the mean path a particle travels before colliding inelastically [29].

4.2.4. The ATLAS muon system

The size of the ATLAS detector is largely determined by the dimension of the muon detectors (see Fig. 13). These are placed cylindrically around the beam axis and in wheels perpendicular to the beam in the end-caps. In total, they cover a pseudorapidity range of $|\eta| < 2.7$ [19]. Effects of multiple scattering are reduced by arranging them in an open structure [31]. Two types of precision muon detectors are used in ATLAS: Monitored Drift Tubes (MDT) and Cathode Strip Chambers (CSC). The latter are applied at large pseudorapidities, i.e. close to the beam axis due to their better resistance to background radiation. For triggering, Resistive Plate Chambers (RPC, in the barrel region) and Thin Gap Chambers (TGC, in the end-cap region) are used. The muon chambers are located in the magnetic field of the toroid magnets. These magnets bend the muon tracks allowing for a momentum measurement via the bending radius of the track whose coordinates are measured by the muon detectors [19].

4.2.5. The trigger

In order to cope with the high luminosity and the resulting high collision and event rate, a trigger has to be applied. The rate for interesting events is very low but a lot of pile-up events occur in the detector: 20 proton-proton collisions happen per bunch crossing causing low-energy background events. The collision rate is 20-40 MHz at a luminosity of nearly $10^{34} \frac{1}{\text{cm}^2\text{s}}$. This has to be reduced to an event rate of 200 Hz, the limit required by the processing time and storage [32].

The trigger consists of 3 Levels, the Level 1 trigger (L1) and two high level triggers, L2 and the event filter (EF). In each step, the event reconstruction is improved and more information on the event is processed. The L1 trigger only searches for events with high transverse momentum, jets, leptons or large missing transverse energy. Having found such an "interesting" event, the L1 trigger passes on information to the L2 trigger on the type of event, the passed selection criteria and also defines a Region of Interest where the interesting signatures were found. The L2 trigger looks at the event in the region of interest with full granularity and precision and selects or rejects the event [19]. The event filter which uses information provided by all detector components and a high quality reconstruction algorithm further reduces the event rate to 200 Hz [32].

5. Physics Object Definition

$t\bar{t}$ -events are the consequence of hard scattering between protons of the incident beam. Hard-scattering processes cause objects with a significant momentum component transverse to the beam direction whose decay products cause high- p_T final-state particles which are then the input to the physics analysis. Objects involved in the event signature of a lepton+jets $t\bar{t}$ -decay are one charged lepton such as an electron or a muon, light- and b-jets and missing transverse energy due to the neutrino. In this section, the identification and reconstruction of these objects on the base of their characteristic signatures in the detector is discussed.

Before that, a detail on proton-proton collisions needs to be discussed.

5.1. Pile-up and Underlying Event

Due to the complex structure of the proton and the high instantaneous luminosity of the LHC, background processes occur which can distort the event topology in the detector and can lead to misinterpretation of physics results. It is therefore vital to understand the background processes happening during a recorded collision, namely pile-up and underlying event.

Underlying Event In addition to the hard collision relevant for physics processes such as $t\bar{t}$ -production, which are caused by coloured interactions between each one parton of the two colliding protons, mostly low-energetic processes can occur between the proton remnants after the hard proton-proton scattering. These include multiple-parton interactions which are coloured interactions within the same proton-proton collision, beam-beam remnants, which are the debris of the protons which participated in the hard scattering, and supplementary initial and final state radiation (see Fig. 16).

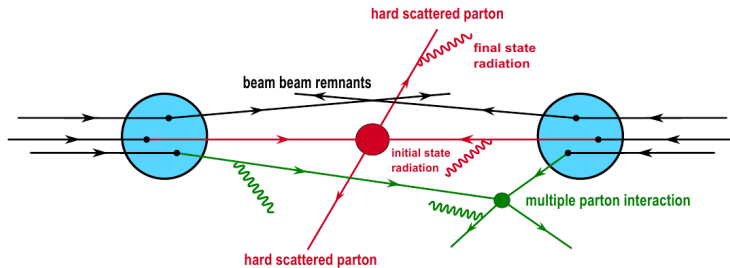


Figure 16: Illustration of the underlying event. In red, the hard scattering process is indicated whereas the remaining partons in the protons cause supplementary, often low-energetic processes (from [33]).

Underlying events are thus a consequence of the complex internal structure of the colliding particles, the protons. Most of the underlying events are low-energetic, i.e. cannot

be described within perturbative QCD theory and are simulated with phenomenological models [33].

Pile-up As a consequence of the high instantaneous luminosity in the LHC (up to $7.7 \cdot 10^{33} \frac{1}{\text{cm}^2\text{s}}$ in 2012), several inelastic proton-proton collisions take place during the same bunch-crossing (in-time pile-up). Crucial factors for the mean number of inelastic proton-proton interaction within the same bunch-crossing are the instantaneous luminosity L , the cross-section for inelastic collisions $\sigma_{\text{inel.}}$ and $N_{\text{bunch}} \cdot f_{\text{LHC}}$ which is the average frequency of bunch crossings in the LHC. The mean number of inelastic proton-proton collisions is evaluated to

$$\langle \mu \rangle = \frac{L \cdot \sigma_{\text{inel.}}}{N_{\text{bunch}} \cdot f_{\text{LHC}}}. \quad (15)$$

With 2012 configuration, the mean number of protons colliding inelastically within a bunch-crossing amounts to $\langle \mu \rangle \approx 20.7$. In-time pile-up is illustrated in Fig. 17.



Figure 17: Example of an event display showing in-time pile-up. The dots are the extrapolated tracks of particles to the vertex issuing from inelastic collisions within the same bunch-crossing (from [34]).

Furthermore, influence from past and future collisions as a consequence of the low bunch-spacing of 50 ns are still present as their energy deposits still affects the signal in the detector (out-of-time pile-up) [35].

5.2. Electrons

For electron³ identification and reconstruction, information provided by the silicon detectors, the transition radiation tracker (TRT), the electromagnetic calorimeter (EM) and the hadronic calorimeter (HCAL)⁴ is used.

At first, clusters of fired EM calorimeter cells are identified by scanning regions of fixed size in order to search for local maxima of energy deposit [36]. Reconstructed tracks in the inner detector are extrapolated in a next step to the electromagnetic calorimeter

³This of course also includes positrons.

⁴For discrimination from hadrons.

middle layer and compared to the seed cluster position in that layer considering a certain displacement due to uncertainty factors. If one track can be matched, the reconstruction is considered as successful and if there are more tracks meeting the requirements, the track with the smallest distance is associated with the electron.

For the energy measurement, the region around the seed cluster is enlarged and the energy deposit is summed up considering contributions of the EM calorimeter, the estimated energy deposits in front and after the EM calorimeter and the estimated energy leakage outside the selected region in longitudinal direction.

Energy calibration is performed on the basis on energy deposit from electrons from $Z \rightarrow ee$, $J/\Psi \rightarrow ee$, $W \rightarrow e\nu$ decays [37].

The electron operating point in this analysis is set to `tight++` [38]. All information from all detector components in question is used in order to gain a good background rejection efficiency. Background is mainly caused by hadrons identified as electrons and converted photons [36]. Stringent criteria on shower shape, a significant signal of transition radiation in the TRT, cluster energy to track momentum ratio, a small leakage in the HCAL, a successful extrapolation to a primary vertex and a signal in the first tracking layer are required among others. Further requirements applied in the "tight++" criteria can be found in [36] and [37].

Isolation criteria are not included in the `tight++` operating point, therefore the isolation criteria `EtCone20@90` and `PtCone30@90` were applied [38].

5.3. Muons

The Muon Spectrometer (MS) is exclusively designed for the detection of muons. It contains detectors of four different technologies which can be classified in two groups: precision tracking chambers and muon triggers (see section 4.2.4) [39].

Muons are reconstructed using a so-called combined reconstruction [38] based on information provided by the Muon Spectrometer as well as by tracks in the Inner Detector using the `muid` algorithm. The muon track is reconstructed by fitting the hits in the Muon Spectrometer considering the inhomogeneous magnetic field and the reconstructed track is extrapolated back to the interaction point. The extrapolated track is matched to tracks in the inner detector [39].

The procedure of combining two independent measurements ensures a better momentum resolution by exploiting the fact that the momentum resolution of the MS and Inner Detector are each superior to the other in complementary p_T -ranges. Furthermore, muons from secondary interactions are rejected more easily [40]. Details on quality cuts required for the muons can be found in [38].

5.4. Jets

5.4.1. Jet Object Definition

Jets manifest itself in the detector as groups of fired calorimeter cells which are topologically related. In general, these can be retraced to tracks of charged particles measured in the inner tracking detector [41].

Jets issue from quarks which hadronize and are measured as particle jets in the detector [1]. These particle jets consist of many particles and contain charged hadrons, leptons, neutrinos and photons, as well as neutral hadrons [30].

Fired calorimeter cells are summarized in radial direction to calorimeter towers. Neighbouring cells with a measured signal form topological cell clusters. A cluster is split if more than one local signal maximum is observed [42].

In the hadronic calorimeter, the jet energy and transverse momentum are measured on the basis of energy deposit in the calorimeter cells attributed to the jet (see next subsection). Only calorimeter cells which give a significant signal above the electronic noise and the noise expected due to pile-up are considered [41].

5.4.2. Jet Reconstruction Algorithm

The jet reconstruction algorithm has to take into account QCD radiation, the emission of gluons, which causes a branching of the jet [43]. Thus, the reconstruction algorithm has to be collinear safe and infrared safe. Collinear safety implies that collinearly emitted particles are attributed to the jet and an infrared safe reconstruction algorithm takes into account soft parton emission [43]. Collinear and infrared safety are achieved by undoing the branching process [44] and successively combining smaller energy deposits to larger energy deposits in its vicinity and therefore cluster soft particles to hard particles [43]. This is the basic idea of the anti- k_T -algorithm used to reconstruct jets in the ATLAS detector.

The algorithm dictates that the distances of all objects to one specific object, i , is calculated. The distance of the object i to the object j is defined as follows:

$$d_{ij} = \min(k_{ti}^{-2}, k_{tj}^{-2}) \frac{\Delta R_{ij}^2}{R^2} \quad (16)$$

$$d_{iB} = k_{ti}^{-2}$$

where k_{ti} is the transverse momentum of the object i , R is a predefined parameter, ΔR_{ij} is the distance between two objects ($\Delta R = \sqrt{\Delta\eta^2 + \Delta\phi^2}$, where η and ϕ are the ATLAS coordinates defined in section 4.2.1). d_{ij} and d_{iB} are evaluated and if d_{ij} is the minimum, the two objects i and j are attributed to the same jet, and if d_{iB} is the minimum, the jet is considered as completely reconstructed and removed from the list.

The distance d_{ij} is smaller than d_{iB} if the factor $\frac{\Delta R_{ij}^2}{R^2}$ is smaller than unity [43]. This implies that the jet cone opening angle has a pre-defined size, which is in case of the analysis in this thesis $R = 0.4$ [38].

The nature of the algorithm causes soft objects to cluster at first with hard object before clustering with other soft objects if a hard object is found within a distance of R . Therefore, the jet energy and direction are determined by hard objects without being altered by soft objects. The shape of jets is conical if no other hard jet is found within a distance of $2R$, otherwise, the two jets will overlap and the conical shape will be distorted. Whereas, if a soft jet is found in the vicinity of a hard jet, a part of the soft jet-cone will be attributed to the hard jet cone. Fig. 18 shows an example of calorimeter

clusters and towers combined to a jet.

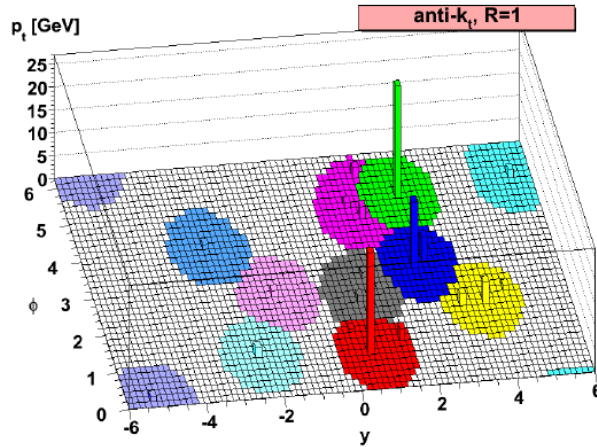


Figure 18: Example of jets reconstructed with the anti- k_T algorithm. It can also be seen by means of this example that in case of soft jets in the vicinity of a hard jet, the overlapping components are always attributed to the hard jet (green and purple jets). From [43].

The jet momentum is obtained by summing up all the 4-momenta of the combined objects [41], consequently, the jet direction is determined mainly by hard objects [43].

5.4.3. The Jet Energy Scale

The measured energy deposit in the cells belonging to the jet must be converted to terms of jet energy. The jet energy scale JES indicates how the summed energy deposits in the calorimeter relate to the jet energy. The precise knowledge of the jet energy scale is fundamental as the jet energy is an input to many physics analysis [1]. Hadronic showers in the calorimeter are very complex and their properties are subject to high fluctuations [30]. This is why the jet energy scale is difficult to determine. Therefore, the uncertainty on the JES is one of the dominant uncertainties in the top quark mass measurement [1].

After the jet reconstruction, the jet energy is corrected for pile-up effects. Pile-up causes a systematic shift towards higher jet energies, therefore, a constant factor is subtracted. This factor is calculated using the estimated jet area and the event energy density. A further correction is applied taking into account the number of reconstructed primary vertices and the expected average number of interactions within one bunch-crossing [38], [41]. Pile-up correction factors are a function of the rapidity and the transverse energy of the reconstructed jet.

In a next step, the jet direction is corrected such that the jet originates from the primary vertex. The jet energy is not sensitive to this correction [41].

Jets with too many constituents associated with it which do not seem to originate from

the primary vertex are discarded. The quantity calculated for this task is called $|JVF|$ which is the p_T sum of the tracks matched to the primary vertex divided by the total p_T associated with the jet. In this analysis, the $|JVF|$ is required to be > 0.5 [38].

The jet energy is calibrated by applying a factor to the measured energy deposit which was obtained from Monte-Carlo simulations, namely MC12a PYTHIA inclusive QCD jet events [38]. Simulated truth jets are compared to the corresponding simulated energy deposition in the calorimeter. This factor also depends on the jet- p_T and η with respect to ATLAS coordinates [41].

Further corrections are applied based on MC simulations as well as on measurement data evaluated requiring p_T -balance and taking well calibrated objects such as photons as reference [41].

Uncertainties on the jet energy scale issue from uncertainty on pile-up [38], modelling uncertainties for very forward jets [45], uncertainties on the modelling of the detector, on the calibration and on the physics models like hadronization [44], to name a few. Another uncertainty factor is the uncertainty on the modelling of the flavour composition and the gluon fraction of the sample [45]. Shower properties, jet fragmentation and the detector response depend on the flavour of the underlying parton [44].

In order to estimate the systematic uncertainty due to the uncertainty on the jet energy scale with a simplified model, the jet scale factor (JSF) is introduced. In this thesis, the JSF takes values in the interval $[0.94;1.06]$ which corresponds to an estimated uncertainty of up to $\pm 6\%$. The 4-momenta of jets of the top quark decay are multiplied with the JSF, thus, jet energy and momentum are varied by some percent. By evaluating the top quark mass as a function of the JSF, the systematic uncertainty on the measured top quark mass due to the uncertainty on the energy scale can be estimated. Note that this is a simplified model as the jet energy scale and its uncertainty depend on the rapidity coordinate η and on the jet- p_T .

5.4.4. b-Tagging

In order to discriminate between b-jets and light jets in the analysis, b-tagging is included. The b-tagging algorithm makes use of the specific properties of jets issuing from b-quarks, like the large branching-ratio into leptons which is about 20% [44] and the longer lifetime which results in a measurable path of flight and a delayed decay at a secondary vertex [38]. A neuronal network-based algorithm called MV1 combining several b-tagging algorithms [44] is employed in the analysis. The nominal efficiency, the fraction of b-tagged jets which indeed issues from a b-quark, is set to 70%. MV1 tagging weights are specified in [46]. The discrimination of light- and b-jets is done on the basis of detector signatures like the calorimeter jets, tracks in the inner detector and the secondary vertex [38]. More details on the b-tagging algorithm can be found in [47].

5.5. Missing Transverse Energy

As the beams entering the detector only possess energy and momentum in longitudinal direction, the momentum before the collision in transverse direction adds up to zero. Therefore, the transverse momentum has to be balanced after the collision as well. The energy deficit is called missing transverse energy $E_{T, \text{miss}}$. In this analysis it is associated with neutrinos which escape the detector undetected [48]. In order to calculate the missing transverse energy, p_T -balance is required and the weighted sum of the E_T of all objects attributed to the event is calculated [38]. Systematic uncertainties on the $E_{T, \text{miss}}$ -measurement arise from systematic uncertainties on the p_T measurement of all reconstructed objects in the event [48].

The signature in the detector of the objects described above is illustrated in Fig. 19.

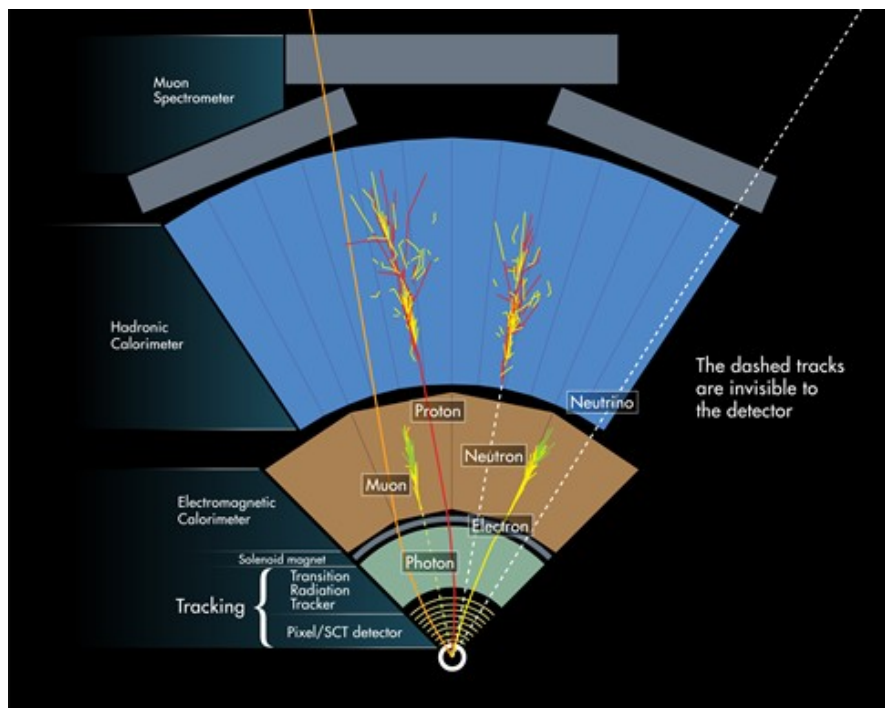


Figure 19: Object signature in the detector of the objects described above. Relevant in this analysis are protons and neutrons as hadrons producing hadronic showers, electrons, muons and neutrinos (from [49]).

6. Simulated Data Sets

Events were generated using PYTHIA 6.426 [50] with P2011C tune based on the CTEQ6L1 PDF set [51] interfaced with POWHEG [52] (CT10 PDF set) [51]. The detector was simulated with a GEANT 4-based [53] ATLAS detector simulation [51].

POWHEG simulates the hard processes occurring during a pp-collision and the production of the outgoing particles, in this case the $t\bar{t}$ -pair, including higher order processes and corrections. PYTHIA resumes from the point of the $t\bar{t}$ -decay to b-quark and W-boson and simulates the succeeding processes such as further decay, showering and hadronization.

A list of all datasets used in the analysis can be found below in Tab. 4. Important parameters are also given: $m_{\text{top}}^{\text{MC}}$ (simulated top quark mass), σ (cross section), k-factor (correction factor to the cross section for higher order processes [54]) and sample statistics (total number of generated events)[51].

$m_{\text{top}}^{\text{MC}}$ [GeV]	σ [pb]	k-factor	sample statistics
165.0	143.21	1.2008	5.988.267
167.5	132.87	1.1997	5.998.058
170.0	123.27	1.1998	5.999.47
172.5	114.49	1.994	14.996.424
175.0	106.46	1.1988	5.998.875
177.5	99.045	1.1984	5.986.769
180.0	92.214	1.1981	5.998.382

Table 4: Properties of the top quark mass variation sample. Based on [51].

7. Event Selection and Reconstruction

The event selection criteria, i.e. the requirements on the events included in the analysis, are presented in this section.

Pre-selection criteria, which are already included in the Monte-Carlo sample, are described in Section 7.1. In 7.2, the analysis-specific selection criteria are listed. Section 7.3 provides a description of the event reconstruction algorithm used for first feasibility studies.

7.1. Pre-Selection Cuts

Several cuts are applied during the processing of a Monte-Carlo sample ensuring a good quality of the events. These cuts are listed hereafter, a detailed description can be found in [55]. Note that all cuts follow the recommendations of the ATLAS Top Working group [38] and [56].

- C1: All events are contained in the GRL, the "Good Run List", a list of all accepted runs during which no problems with the detector or the reconstruction system was registered.
- C2: An event is only kept if there was no problem concerning the Liquid Argon calorimeter like noise bursts or dead cells. Events will be deleted as well if they occur within a certain time span around these failures. If only incomplete detector information is available due to failures of the Liquid Argon Calorimeter system or of the tile calorimeter system, the event is discarded.
- C3: Electrons have to pass either the trigger "EF_e24vhi_medium1" or "EF_e60_medium1" and muons either the trigger "EF_mu24i_tight" or "EF_mu36_tight". For details see [38].
- C4: A primary vertex to which all objects in the event can be retraced is required.
- C5: The event has to contain at least one charged lepton fulfilling either the "tight++" criteria in case of electrons or the "tight" criteria in case of a muon (see [57] for a further definition of the "tight" criteria for muons, and for the "tight++" criteria for electrons see [36]).
- C6: One charged lepton of each flavour passing the "tight++" criteria (electron) or the "tight" criteria (muon) is allowed at the most.
- C7: Only one lepton flavour is allowed. This lepton has to pass the "tight++" criteria in case of electrons or the "tight" criteria in case of a muon.
- C8: This lepton must match the triggered lepton.
- C9: The event is discarded if the inner detector track of any electron or muon coincide.

- Events containing a bad jet, e.g. signals with jets signatures but caused by hardware problems, calorimeter noise, beam-gas-interaction, cosmic rays, etc., are discarded.
- C11: The event has to contain at least one reconstructed jet.
- C12: The event has to contain at least two reconstructed jets.
- C13: The event has to contain at least three reconstructed jets.

The cuts are illustrated in the cut-flow diagram in Fig. 20.

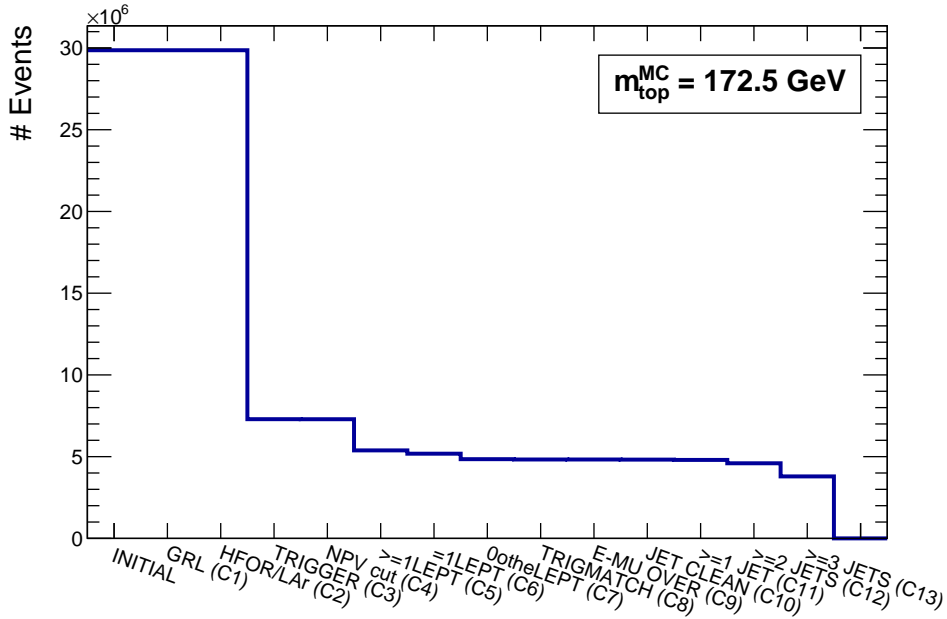


Figure 20: Cutflow diagram for cuts C1-C13 (Pre-Selection Cuts) for the $m_{\text{top}}^{\text{MC}} = 172.5 \text{ GeV}$ sample.

Also, a jet- η cut ($|\eta| < 2.5$) as well as a cut on the lepton- η (see C20 in the next subsection) were implemented but are not included in the pre-selection cuts cutflow diagram.

7.2. Selection Cuts

In order to enhance signal over physics background⁵, further selection cuts adapted to the expected event signatures are required. Event signatures of a $t\bar{t}$ lepton+jets decay are a high- p_T lepton, significant missing transverse energy $E_{T, \text{miss}}$, 4 high- p_T jets thereof

⁵Note that within the scope of this Master's thesis, physics background was not yet examined.

2 b-jets which can be discriminated from light jets with b-tagging algorithms (see section 5.4.4). In this subsection, all further analysis-specific selection cuts are listed.

- C14: The transverse energy of every jet is required to be above 30 GeV.
- C15: All jets in the event are required to be central with $|\eta| < 2.5$.
- C16: The event has to contain at least 4 jets and 6 jets at the most.
- C17: The event has to contain at least 2 b-tagged jets.
- C18: The event has to contain exactly one lepton (either electron or muon)
- C19: In case the lepton is an electron, its energy must be greater than 30 GeV, in case of a muon, its p_T has to be greater than 30 GeV.
- C20: If the event contains a muon, its $|\eta|$ is required to be smaller than 2.5 and if the event contains an electron, it has to be found within a region of $\eta < |2.47|$ excluding the region $1.37 < |\eta| < 1.52$ as limited resolution is to be expected in that pseudorapidity range due to the transition from the barrel to the endcap calorimeter [36].
- C21: Calculation of the missing transverse energy at least has to yield $E_{T, \text{miss}} > 30 \text{ GeV}$

A cut-flow diagram illustrating the event loss due to cuts C14-C21 is shown in Fig. 21.

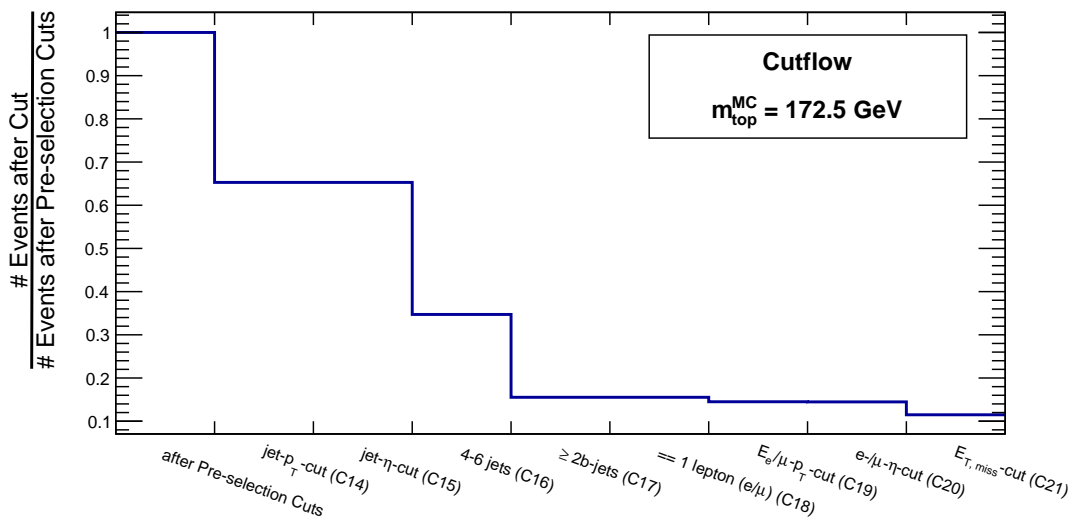


Figure 21: Cutflow diagram illustrating the cuts C14-C21. Note that some of the cuts were already implemented in the Monte-Carlo sample beforehand and therefore do not influence the event number.

7.3. Jet-Parton Matching

After selecting the events, the jets have to be assigned to the partons from the $t\bar{t}$ -decay. In the first part of the analysis, a $t\bar{t}$ reconstruction method is chosen suitable to perform feasibility studies without having to deal with effects from combinatorial background. The approach in the so-called jet-parton matching is to assign the partons to the reconstructed detector jets using coordinate information of the parton and the detector jets and thus their mutual distance. This procedure is only applicable in Monte-Carlo samples as information on the partons is not found in real data.

As a first step, the partons from the $t\bar{t}$ -decay are identified using the information on the parton identity. The top quarks and their final decay products, one bottom quark originating from one top quark each, two light quarks and a lepton and a neutrino from the decay of the two W-bosons are identified that way. The quarks are matched to the jets by collecting all jets within a distance⁶ of $\Delta R < 0.4$ from the parton.

This is motivated by the jet-reconstruction procedure (anti- k_T , see section 5.4.2 and [43]): All energy deposits within a distance $\Delta R < 0.4$ around a high- p_T calorimeter tower are combined to a jet. This jet cone has by definition an opening angle of $\Delta R = 0.4$ unless the jet is distorted by another nearby high- p_T jet.

If exactly one jet is found within a distance of $\Delta R < 0.4$, this jet is assigned to the parton and the jet assignment is considered successful. The jet assignment is considered failed if none or more than one jets are found within the cone with an opening angle of 0.4 around the parton.

The resulting distribution of the 4-momentum invariant mass of the reconstructed top quarks ($m_{\text{top}}^{\text{MC}} = 172.5 \text{ GeV}$) can be found in Fig. 22.

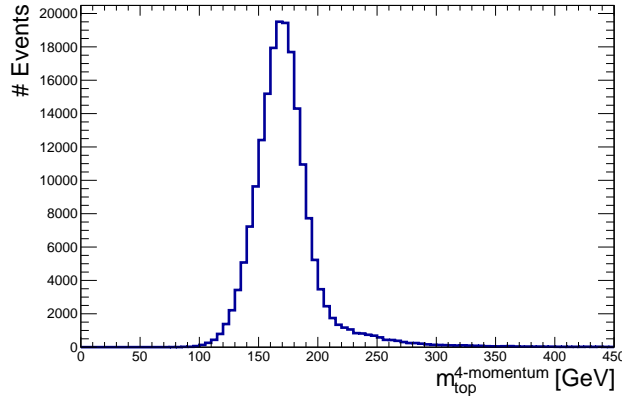


Figure 22: 4-momentum invariant mass of the hadronically decaying top quark reconstructed with jet-parton matching.

⁶ $\Delta R = \sqrt{(\Delta\Phi)^2 + (\Delta\eta)^2}$ where $\Delta\Phi$ and $\Delta\eta$ are the difference in η and ϕ coordinates of the jet and the parton.

8. The Top Quark Mass Estimator $m_{\text{top}}^{\text{angle}}$

The top quark mass is always measured using a variable which is sensitive to the top quark mass. This variable is called the top quark mass estimator. In this thesis, an estimator is employed which is based on entirely geometric considerations: the top quark mass estimator is only dependent on the angles between the top quark decay products. This is motivated by the fact that the measured jet directions reflect very well the direction of the initial quarks. Therefore, the angles can be determined very precisely and with a higher precision than the jet energies [1]. In this section, the top quark mass estimator this analysis is based on is introduced and derived intuitively on the basis of geometrical assumptions. For a derivation using energy and momentum constraints, see [58].

In the top quark rest frame, the 3-momentum vectors of the three top quark decay products span a plane as all momenta have to be balanced. This is visualized in Fig. 23:

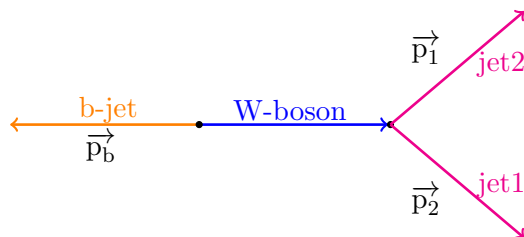


Figure 23: Illustration of the decay of a top quark at rest (not to scale). Due to kinematic constraints (see text), the decay products are emitted in the same plane.

The resting top quark decays in a two-body decay into a b-quark and a W-boson emitting the decay products back-to-back and the W-boson subsequently decays in another two-body decay into either two jets or a lepton and the corresponding neutrino.

Note that in this analysis, only the hadronic top quark decay is considered. For a leptonic decay, the missing transverse energy is correlated to the jet energy. If varying the jet energy (JSF variation studies, see section 5.4.3), the missing transverse energy has to be varied accordingly. An incorrect correction would distort the geometry of the leptonic decay and therefore alter the result.

Momentum conservation implies momentum balance (equation (17)) and equation (18) states energy conservation:

$$\vec{p}_{\text{jet1}} + \vec{p}_{\text{jet2}} + \vec{p}_{\text{jetb}} = 0 \quad (17)$$

$$E_1 + E_2 + E_b = m_{\text{top}} \quad (18)$$

where \vec{p}_i , $i \in \{\text{jet1}, \text{jet2}, \text{jetb}\}$ denote the momentum 3-vectors of light jet 1 and 2 and the b-jet, respectively and E_j , $j \in \{1, 2, b\}$ are the energies of the light jets and the

b-jet.

Due to the constraint of momentum balance in all directions in space (equation (17)), the top quark is situated in the center of gravity of the triangle spanned by the three top quark decay products. The decay products' momentum vectors reside on the median line of the triangle (illustration: see Fig. 24)⁷.

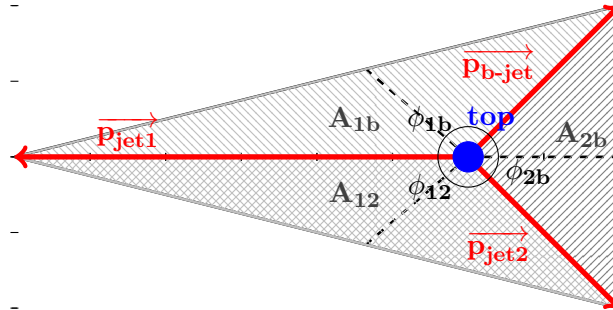


Figure 24: Illustration of the geometrical properties of the triangle spanned by the top quark decay products' momentum vectors. The top quark (blue dot) resides in the center of gravity of the triangle and the momentum vectors \vec{p}_i , $i \in \{1, 2, b\}$ (thick red arrows) are in line with the median lines of the triangle (dashed black lines). The momentum vectors divide the triangle into 3 parts of equal area A_{12} , A_{1b} and A_{2b} . The angles ϕ_j , $j \in \{12, 1b, 2b\}$ denote the angles between the decay products, the angles this analysis is based on.

In such a constellation, the momentum vectors divide the triangle into three sub-triangles of equal area (differently hatched areas A_{12} , A_{1b} and A_{2b} in Fig. 24) [60]. A calculation of these areas using the angles between the decay products' 3-momentum vectors \vec{p}_i , $i \in \{1, 2, b\}$ and the absolute values of the momentum vectors, which are equal to the energies E_i , $i \in \{1, 2, b\}$ if neglecting the jet masses, yields [59]:

$$2 \cdot A_{12} = E_1 E_2 \sin \phi_{12} \quad (19)$$

$$2 \cdot A_{1b} = E_1 E_b \sin \phi_{1b} \quad (20)$$

$$2 \cdot A_{2b} = E_2 E_b \sin \phi_{2b} \quad (21)$$

where ϕ_k , $k \in \{12, 1b, 2b\}$ denotes the angles introduced in Fig. 24.

Considering that all the areas A_j are equal, the energies E_1 and E_2 can be written using equations (19)-(21) as

$$E_1 = \frac{\sin \phi_{2b}}{\sin \phi_{12}} \cdot E_b \quad (22)$$

$$E_2 = \frac{\sin \phi_{1b}}{\sin \phi_{12}} \cdot E_b \quad (23)$$

⁷By definition, the median lines intersect at the center of gravity [59].

Calculating the top quark mass using equation (18) and inserting equations (22) and (23) yields equation (26), but the expressions in equation (24) and (25) can be derived analogously:

$$E_1 = m_t * \frac{\sin \Phi_{2b}}{\sin \Phi_{12} + \sin \Phi_{1b} + \sin \Phi_{2b}} \quad (24)$$

$$E_2 = m_t * \frac{\sin \Phi_{1b}}{\sin \Phi_{12} + \sin \Phi_{1b} + \sin \Phi_{2b}} \quad (25)$$

$$E_b = m_t * \frac{\sin \Phi_{12}}{\sin \Phi_{12} + \sin \Phi_{1b} + \sin \Phi_{2b}} \quad (26)$$

A calculation of the W-boson mass m_W yields (neglect light quark mass):

$$(m_W)^2 = \left[\left(\frac{E_1}{p_1} \right) + \left(\frac{E_2}{p_2} \right) \right]^2 = 2E_1E_2(1 - \cos(\Phi_{12})) \quad (27)$$

After plugging in (24) and (25) in (27), one obtains the top quark mass estimator $m_{\text{top}}^{\text{angle}}$:

$$\left(\frac{m_W}{m_{\text{top}}^{\text{angle}}} \right)^2 = \frac{2 \sin(\Phi_{1b}) \sin(\Phi_{2b}) [1 - \cos(\Phi_{12})]}{[\sin(\Phi_{12}) + \sin(\Phi_{1b}) + \sin(\Phi_{2b})]^2} \quad (28)$$

Note that the top quark mass estimator (equation (28)) only depends on the angles between the decay products and doesn't hold any dependence on the jet energies. It should therefore be independent on the jet scale factor (see section 5.4.3). Latter statement can be proven intuitively: A variation of the jet energies only changes the length of the vectors in Fig. 24 but not their directions. The angles consequently stay invariant.

The derivation of equation (28) shown above affirms that it is indeed important for the validity of the method that the top quarks are at rest. Without this requirement, the top quark is not located in the center of gravity of the triangle spanned by its decay products and the decay products are not emitted in the same plane and the assumptions used in the derivation (equations (17)-(23)) cannot be employed.

Therefore, a Lorentz-Transformation has to be applied first on all top quarks if calculating their mass using this method. But a Lorentz-Transformation requires the jet energies, or, rather the Lorentz-factor $\beta\gamma$ as input (see appendix B). The factor β is defined as $\frac{|\vec{p}|}{E}$ where $|\vec{p}|$ is the top quark momentum and E its energy. The jet energy is proportional to the factor γ where γ is defined as $\frac{1}{\sqrt{1-\beta^2}}$. In this thesis, the factor $\beta\gamma$ is defined as negative, if the momentum points in the negative z-direction according to the definition of the ATLAS coordinate system and positive, if pointing in the positive z-direction.

In the following sections, an analysis strategy is developed in order to calculate the top quark mass using this estimator and the impact of the Lorentz-Transformation on the estimator is examined.

9. Monte-Carlo Studies on the Angle Method

In the previous section, the top quark mass estimator $m_{\text{top}}^{\text{angle}}$ was introduced. In this section, the angle method is applied to $t\bar{t}$ -pairs which were generated by Monte-Carlo simulation and reconstructed using jet-parton matching (see section 7.3). Thus, the $m_{\text{top}}^{\text{angle}}$ distributions obtained with equation (28) are devoid of influence of combinatorial background, incorrectly reconstructed top-antitop quark pairs.

The estimator introduced in section 8 was constructed under the assumption that the top quarks are produced at rest. In this section, the behaviour of the angle method for boosted top quarks is examined and an analysis strategy is developed to measure the top quark mass using jet angles beginning from the method as described in Katharina Behr's thesis [58] who performed first studies on this method.

In [58], a functional dependence of the top quark mass estimator on $\beta\gamma$ was observed. The investigation of this dependence is one of the main aims of this thesis.

9.1. The Functional Dependence of $m_{\text{top}}^{\text{angle}}$ on $\beta\gamma$

The angle method as described in section 8, equation (28), should be independent on the jet energies. However, equation (28) is only valid for top quarks which are produced at rest. For top quarks with⁸ $\beta\gamma \neq 0$, a Lorentz-transformation (see appendix B) has to be applied first which requires the knowledge of the energies and momenta of the top quarks. Consequently, the Lorentz-transformation introduces a residual dependence on the jet energies. In [58], a functional dependence of $m_{\text{top}}^{\text{angle}}$ on the factor $\beta\gamma$ was observed in simulated 2011 data ($\sqrt{s} = 7 \text{ TeV}$).

In Fig. 25, the dependence of the top quark mass estimator on the factor $\beta\gamma$ is shown for simulated 2012 data ($\sqrt{s} = 8 \text{ TeV}$). Note that for all the studies described in this section, unless otherwise stated, events generated with a simulated top quark mass of $m_{\text{top}}^{\text{MC}} = 172.5 \text{ GeV}$ were used.

⁸For a definition of β and γ see section 8.

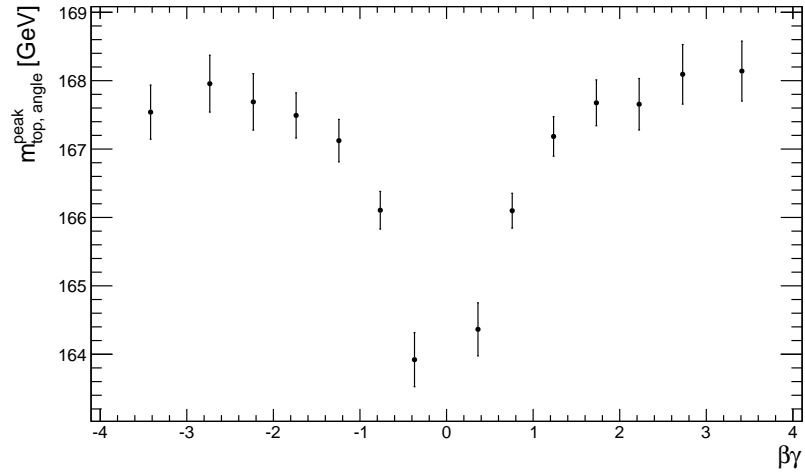


Figure 25: Functional dependence of the peak position of the $m_{\text{top}}^{\text{angle}}$ -estimator distribution on $\beta\gamma$.

In Fig. 25, the top quark mass estimator is shown for different bins of $\beta\gamma$ of the reconstructed top quark. For each bin, the jet 4-momentum vectors are transformed into the top quark rest frame and $m_{\text{top}}^{\text{angle}}$ is calculated for each event in the corresponding bin according to equation (28). The resulting distributions are fitted with a Crystal Ball Function (see appendix A). For each $\beta\gamma$ bin, the peak position $m_{\text{top, angle}}^{\text{peak}}$ is extracted (see Fig. 26). In the following, $m_{\text{top, angle}}^{\text{peak}}$ is used as top quark mass estimator.

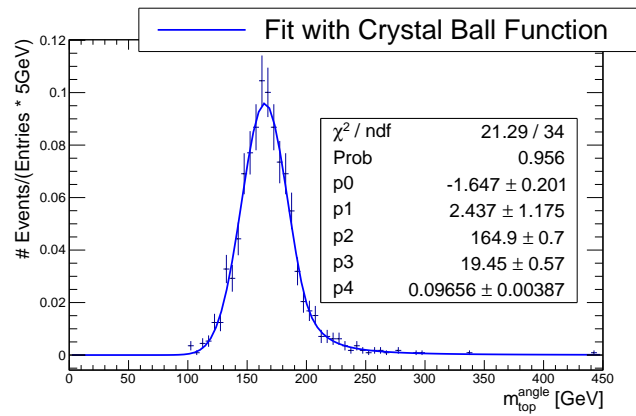


Figure 26: Example of a fit of the Crystal Ball function to the $m_{\text{top}}^{\text{angle}}$ -distribution.

9.2. Analysis using low- $\beta\gamma$ Top Quarks

Using only top quarks produced at rest, one could measure the top quark mass directly without applying a Lorentz-transformation to the top quark rest frame and therefore avoid introducing the residual dependence on the jet energies due to the Lorentz-transformation. However, as a consequence of the object selection cuts (see section 7.2), top quarks with low boost are disfavoured: For top quarks at rest, the energy of each of the three jets would be approximately $170:3 \approx 60$ GeV. Not all of this energy or momentum would be transversal and a cut is applied at a transverse momentum of 30 GeV (Cut C14, see section 7.2). This explains the drop of statistics at low $\beta\gamma$ in the $\beta\gamma$ -distribution of the top quarks in the samples indicated in Fig. 27 (a).

Fig. 27 (b) shows a zoom on the top quark $\beta\gamma$ -distribution at low values of $\beta\gamma$.

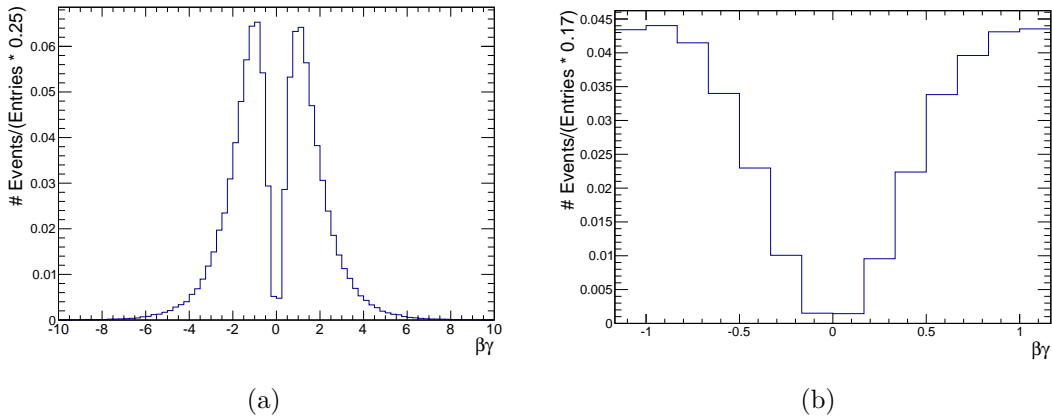


Figure 27: Distribution of $\beta\gamma$ -values of the reconstructed top quarks in the $m_{\text{top}}^{\text{MC}} = 172.5$ GeV Monte-Carlo sample after applying cuts C1-C21. Right: Same as left but zoom on low $\beta\gamma$ -values.

Fig. 28 shows the dependence of the top quark mass estimator on the jet scale factor (JSF, see section 5.4.3) using only low- $\beta\gamma$ top quarks. The top quark mass estimator $m_{\text{top, angle}}^{\text{peak}}$ is defined as the peak value of the Crystal Ball fit to the $m_{\text{top}}^{\text{angle}}$ distribution (see Fig. 26). For a qualitative proof of the independence of the $m_{\text{top, angle}}^{\text{peak}}$ -estimator on the JSF, the 4-momenta of the jets are multiplied by a factor (JSF) within the range of 0.94 and 1.06 and the top quark mass estimator $m_{\text{top, angle}}^{\text{peak}}$ is calculated as a function of the JSF.

Since there are barely top quarks produced at rest (Fig. 27), in these studies top quarks with $\beta\gamma < |0.3|$ are used in order to increase the statistics⁹.

The result can be seen in Fig. 28.

⁹A Lorentz-Transformation is applied here as well in order to boost to the top quark rest frame.

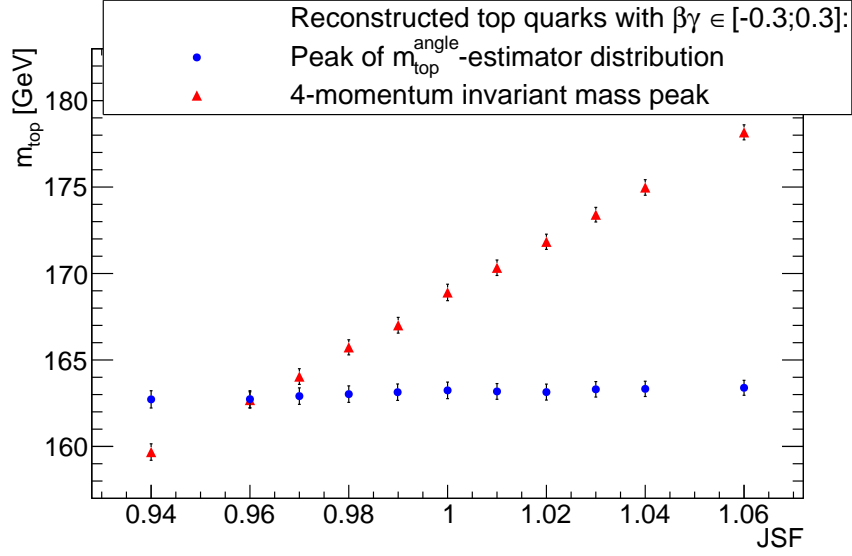


Figure 28: The peak position of the $m_{\text{top}}^{\text{angle}}$ -estimator distribution of low- $\beta\gamma$ top quarks (blue dots) as a function of the JSF. For comparison, the peak position of the 4-momentum invariant mass distribution is plotted using red triangles.

For comparison, the peak position of the 4-momentum invariant mass distribution of the decay products¹⁰ obtained for different JSFs is superimposed. The dependence on the JSF is significantly reduced when using the angle method. A small dependence on the JSF is still visible which is due to the fact that all top quarks in that reduced sample are slightly boosted (see Fig. 29).

In fact, a fit of a linear function yields better results than a fit with a constant function: the uncertainty on the slope parameter in Fig. 29 (see statistics box) is smaller than the absolute value of the slope parameter.

¹⁰Calculation of 4-momentum invariant mass m : $m^2 = \frac{1}{c^4} \cdot (E^2 - \vec{p}^2 c^2)$ where c is the speed of light, E is the energy of the top quark and \vec{p} is the 3-momentum of the top quark.

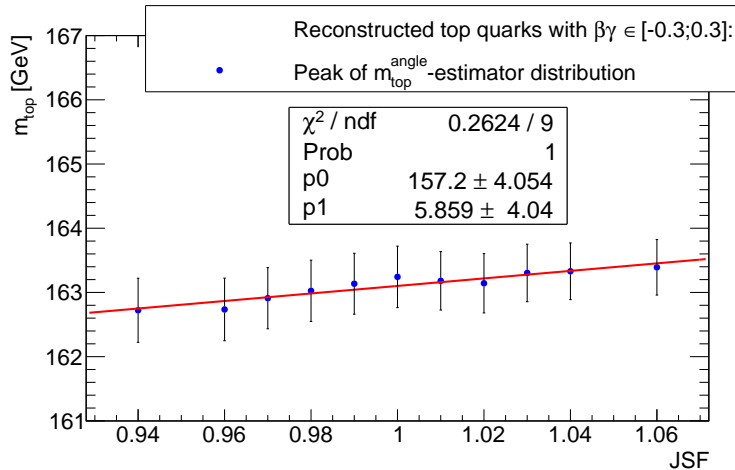


Figure 29: Illustration of the slight dependence of the peak position of $m_{\text{top}}^{\text{angle}}$ on the JSF for low- $\beta\gamma$ top quarks.

Given the small statistics in case of top quarks at rest or with low boost (see Fig. 27 (b)), it is not recommendable to perform the analysis only with top quarks with a small boost. Therefore, a dedicated procedure needs to be developed to handle the dependence of the measured top quark mass on the factor $\beta\gamma$.

9.3. The Angle Method for Top Quarks with Non-Zero Boost

The low dependence of the measured top quark mass on the JSF was shown qualitatively for top quarks with a small boost. The method can thus be assumed to work for top quarks with $\beta\gamma=0$, top quarks at rest, for which the method was developed.

The concept must now be transferred to the case of top quarks with $\beta\gamma \neq 0$. In section 9.1, Fig. 25, a functional dependence of $m_{\text{top}}^{\text{angle}}$ on $\beta\gamma$ can be noted. If this functional dependence could be parametrized, the value for the top quark mass estimator could be extrapolated to $\beta\gamma=0$, i.e. to the case of top quarks at rest and for top quarks at rest, the method works according to section 9.2. In order to find a function which parametrizes the $m_{\text{top, angle}}^{\text{peak}}(\beta\gamma)$ -distribution (Fig. 25, section 9.1) best, the origin or the cause of this functional dependence has to be found.

9.4. Studies on Parton Level

Studies are performed to investigate the origin of the dependence of the $m_{\text{top}}^{\text{angle}}$ estimator on $\beta\gamma$. According to equation (28) (section 8), no dependence of the estimator on $\beta\gamma$ should be visible if the system was transformed to the correct frame (i.e. top quark rest frame). On parton level, only the quarks and their decays are simulated, object kinematics and decay geometry are not yet altered by hadronization effects or detector effects. Thus, studies on parton level are performed. Fig. 30 is obtained analogously to Fig. 25 (section 9.1) but using parton 4-momenta instead of detector jet 4-momenta.

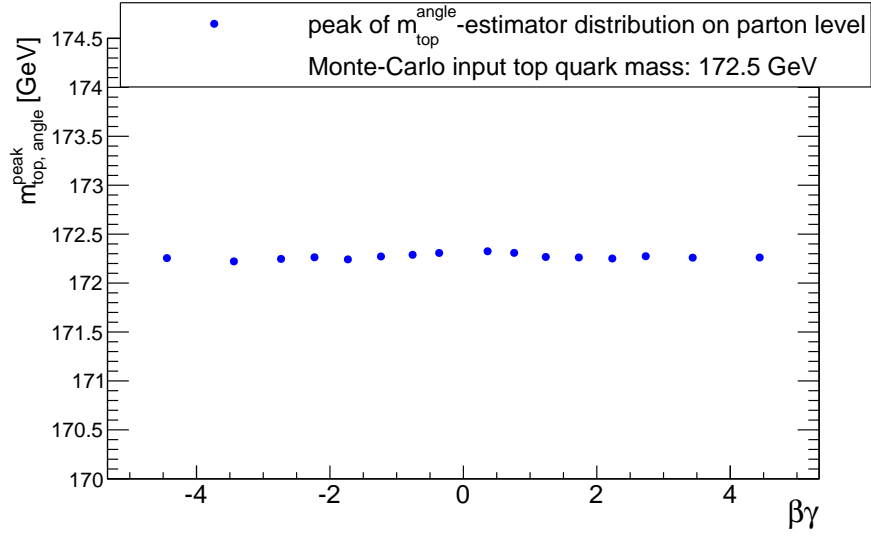


Figure 30: Dependence of $m_{\text{top, angle}}^{\text{peak}}$ on $\beta\gamma$ in case of a parton-level analysis.

No dependence of the estimator $m_{\text{top, angle}}^{\text{peak}}$ on $\beta\gamma$ is observed according to Fig. 30. Note that, although a top quark mass of 172.5 GeV is simulated, an offset in the measurement of a few 100 MeV with respect to the simulated top quark mass is observed in Fig. 30.

The effect accounting for the offset can issue from the finite decay width of the top quark. It was already mentioned in section 3, that gluon-fusion is the dominant top-antitop production channel. The parton distribution function (see section 3.1, Fig. 5) indicates that gluons in the protons preferably carry a small fraction of the proton's energy. Therefore, predominantly top quarks with a mass at the lower end of the decay peak width are produced.

The absence of a $\beta\gamma$ -dependence on parton level can either mean that the functional dependence is introduced during the process of hadronization or during the energy measurement in the detector.

To examine how physics effects like hadronization and detector effects alter the momentum of the top quark, the top quark momentum distributions on parton and on detector level are compared component-wise. Fig. 31 shows the longitudinal momentum (p_1) distribution of the top quark on parton level (red) and on detector level (black), normalized and scaled to the same height, superimposed.

For a quantitative evaluation of the change of the top quark longitudinal momentum from parton to detector level, the momentum dependent factor $\frac{p_{1, \text{parton level}}}{p_{1, \text{detector level}}}$ is calculated by which the detector level longitudinal momentum has to be multiplied in order to make it coincide with the parton level longitudinal momentum distribution. In other words, the factor is calculated by which the detector level p_1 -distribution has to be compressed

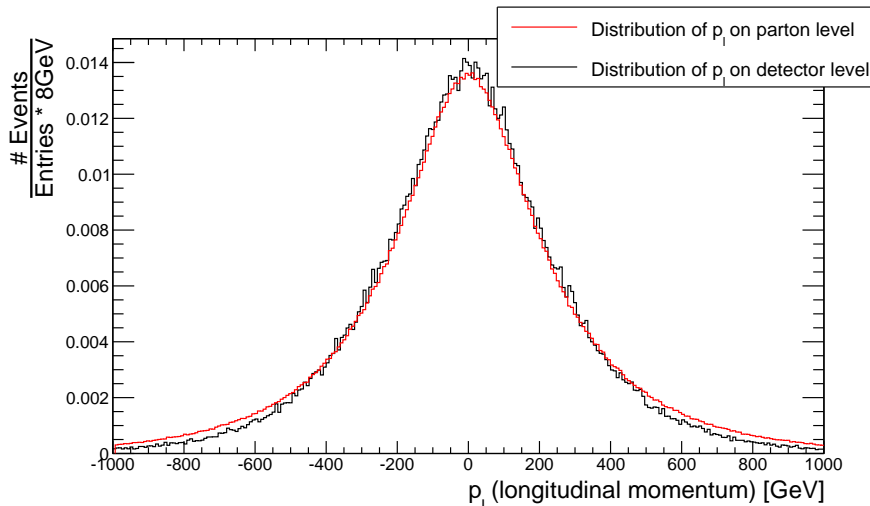


Figure 31: Normalized longitudinal momentum (p_l) distribution of the reconstructed top quarks on parton level (red) and on detector level (black), scaled to the same height.

or stretched in order to make it coincide with the parton-level top quark p_l -distribution. The factor $\frac{p_{l, \text{parton level}}}{p_{l, \text{detector level}}}$ is plotted in Fig. 32 as a function of the longitudinal momentum of the reconstructed top quark at parton level.

The shape of the distribution in Fig. 32 looks very similar to the distribution of $m_{\text{top, angle}}^{\text{peak}}$ as a function of $\beta\gamma$ on detector level (see Fig. 25, section 9.1). The systematic shift of the p_l -distribution, which happens during the transition from parton to detector level, depends on the value of the longitudinal component of the top quark momentum. This indicates that the effect most probably issues from systematics in the jet energy measurement in the detector. The shape of the distribution in Fig. 32 suggests a correlation to the rapidity y which is related to the longitudinal coordinate:

$$y = \text{ASinh}(\beta_z \gamma) \quad (29)$$

with $\beta_z = \frac{p_z}{E}$ and E being the energy and p_z the longitudinal momentum.

An ASinh-function indeed parametrizes the distribution in Fig. 32 very well (see Fig. 33).

Similarly, the top quark transverse momentum (p_T) distribution is studied at parton and detector level (see Fig. 34).

The factors $\frac{p_{T, \text{parton level}}}{p_{T, \text{detector level}}}$ needed to correct the detector level top quark transverse momentum distribution to parton level are shown in Fig. 35 as a function of the parton level top quark transverse momentum.

This shape does not clearly mirror any feature of the $m_{\text{top, angle}}^{\text{peak}}(\beta\gamma)$ -distribution as a function of $\beta\gamma$ (Fig. 25) and thus, no conclusion can be drawn from Fig. 35. Therefore, to examine the dependence of the estimator on the top quark p_T , another approach has

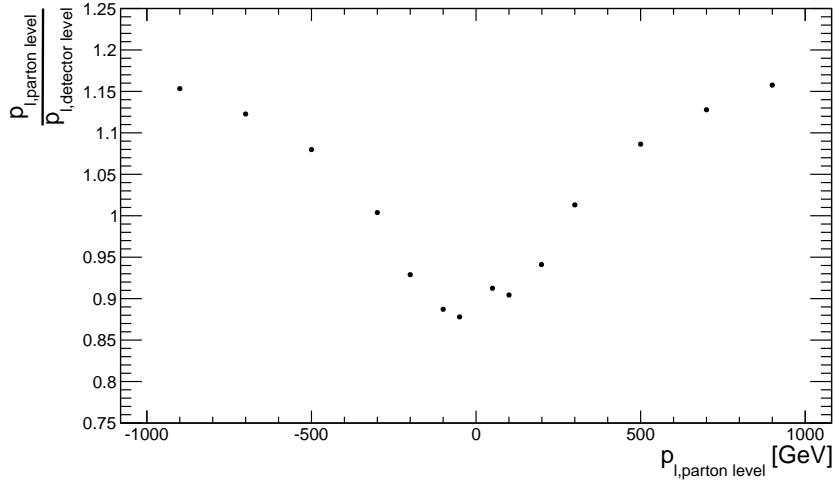


Figure 32: The factor $\frac{p_{l, \text{parton level}}}{p_{l, \text{detector level}}}$ as a function of the parton level longitudinal momentum $p_{l, \text{parton level}}$ of the top quark. Note that the result was obtained by fitting the distributions in Fig. 31 and making coincide the fitting functions.

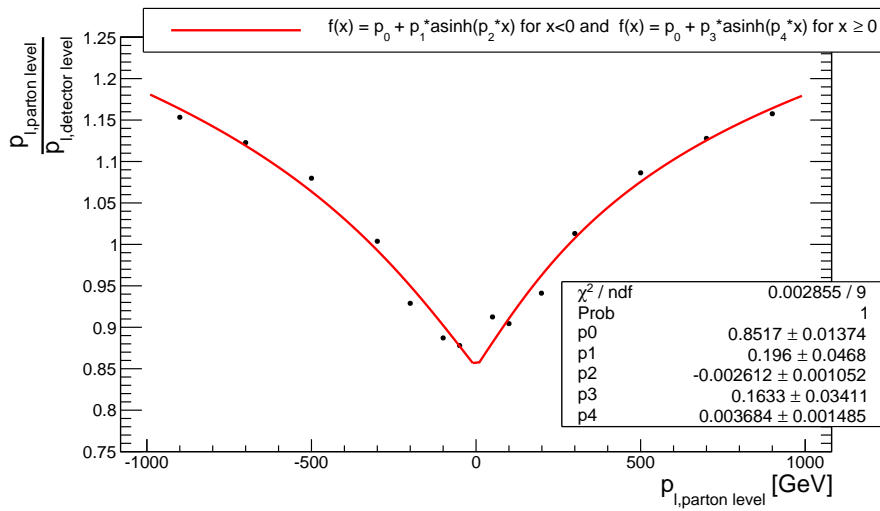


Figure 33: Fit of a ASinh-function to the data points in Fig. 32 for $p_{l, \text{parton level}} < 0$ and $p_{l, \text{parton level}} \geq 0$, respectively, with the boundary condition that the ASinh-functions intersect at $p_{l, \text{parton level}} = 0$.

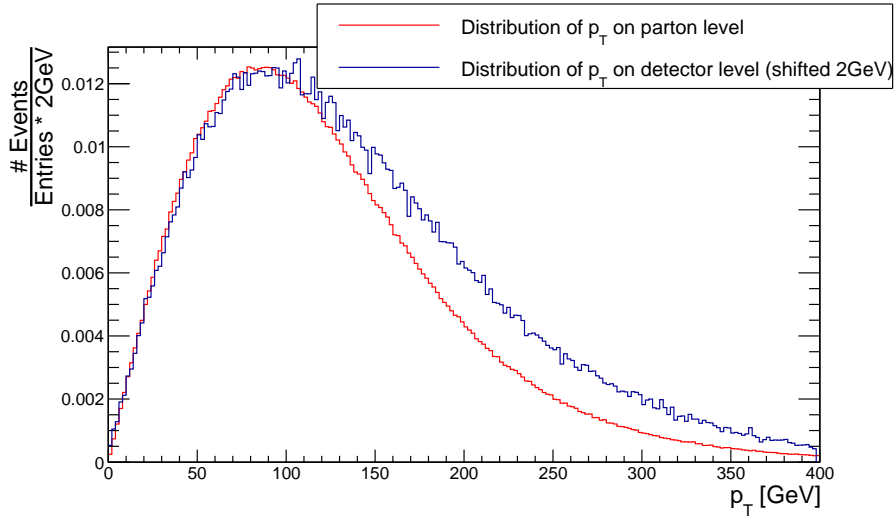


Figure 34: Comparing the top quark p_T -distribution at detector level (blue) and at parton level (red). Note: The distribution at detector level is shifted by 2 GeV towards lower momenta to make the distribution coincide at low momenta. This can be justified by a correction of systematic offset in the calibration (for example: too much overlap removal).

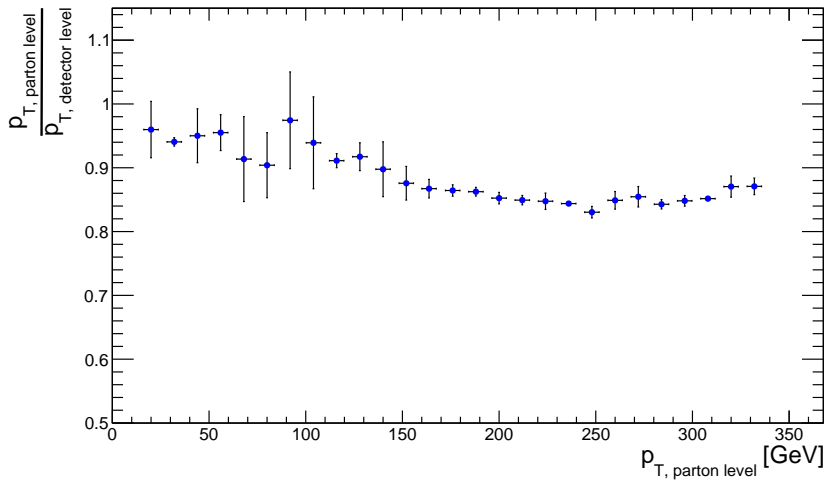


Figure 35: Factor $\frac{p_{T, \text{parton level}}}{p_{T, \text{detector level}}}$ by which the detector level p_T -distribution has to be compressed in order to correct it back to parton level, calculated for different bins of the parton-level p_T .

to be chosen: Fig. 36 shows the $m_{\text{top, angle}}^{\text{peak}}$ -distribution as a function of the top quark p_T . The top quarks were divided into bins of top quark p_T and the peak position of the $m_{\text{top}}^{\text{angle}}$ -distribution was calculated separately for each of the p_T -bins.

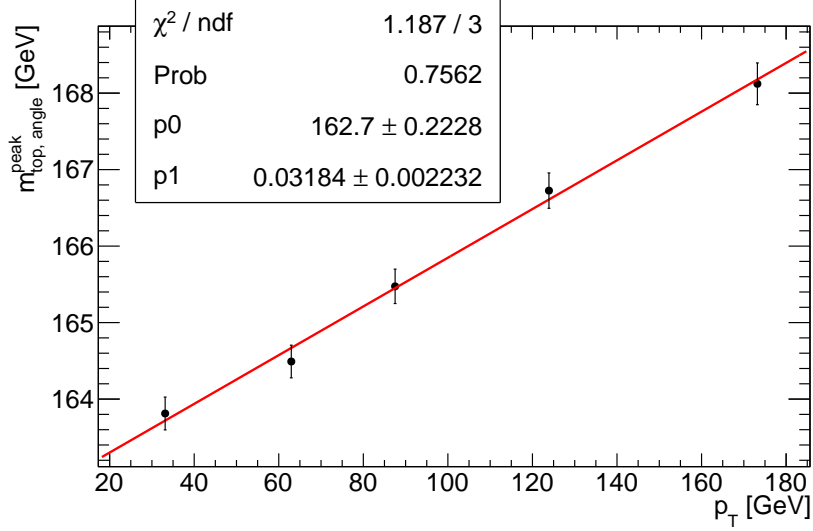


Figure 36: Plotting the peak position of the $m_{\text{top}}^{\text{angle}}$ -estimator distribution as a function of the top quark p_T . For this study, the sample is divided into bins of top quark p_T .

It is visible from Fig. 36, that a dependence on p_T exists which is assumed to be approximately linear according to Fig. 36.

The dependence of the peak position of the $m_{\text{top}}^{\text{angle}}$ -distribution on the transverse and longitudinal components motivates the analysis approach which will be introduced in the next subsection.

9.5. Analysis Strategy

In section 9.1-9.4, studies have been performed to parametrize the peak position of the $m_{\text{top}}^{\text{angle}}$ -distribution ($m_{\text{top, angle}}^{\text{peak}}$) as a function of $\beta\gamma$ allowing to apply the angle method to top quarks with $|\beta\gamma| > 0$. It was shown that on parton level, the peak position of the $m_{\text{top}}^{\text{angle}}$ -estimator distribution yields no dependence on $\beta\gamma$ and therefore, the dependence is most likely introduced by a Lorentz-transformation into the incorrect frame. Consequently, studies were performed on how the top quark momentum distribution on detector level changes with respect to parton level. The studies described in section 9.4 indicate an ASinh-dependence of $m_{\text{top, angle}}^{\text{peak}}$ on the longitudinal top quark momentum p_l pointing to a correlation to the rapidity. Plotting $m_{\text{top, angle}}^{\text{peak}}$ as a function of $\text{ASinh}(\beta_z\gamma)$ can therefore be parametrized by a linear function.

There is also a dependence on the transverse top quark momentum which has to be taken into account. But this dependence could not be determined on the base of a comparison between the top quark p_T on parton and detector level. Fig. 36 in section 9.4 leads to the assumption, that this dependence can be parametrized using a linear function.

The possibility to treat the top quark momentum components separately motivates a 2-step analysis.

The sample is divided into top quark p_T -bins like illustrated in Fig. 37. The bins are chosen such that the p_T -range in the bins is not too large whereas high values of p_T are not included due to expected effects of gluon radiation¹¹ and because of the low statistics. Furthermore, the bins should have approximately equal statistics.

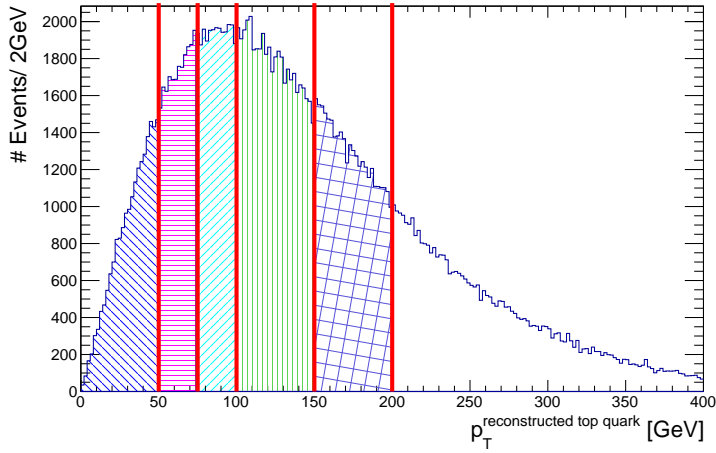


Figure 37: Illustration of the top quark p_T -bins used in the analysis. Each of the relevant bins is colour-coded.

Each of the top quark p_T -bins is subsequently divided into bins of $\beta_z \gamma$. The peak position of the $m_{\text{top}}^{\text{angle}}$ -estimator distribution is evaluated for each of these $\beta_z \gamma$ -bins and plotted as a function of $A \text{SinH}(\beta_z \gamma)$. An example of the resulting distribution can be seen in Fig. 38.

By extrapolating to $A \text{SinH}(\beta_z \gamma) = 0$, which is equivalent to an extrapolation to $\beta_z \gamma = 0$, $m_{\text{top, angle}}^{\text{peak}}$ is corrected in longitudinal direction. This is done by fitting two linear functions to $m_{\text{top, angle}}^{\text{peak}}(A \text{SinH}(\beta_z \gamma))$ with the constraint that these two linear functions intersect at $A \text{SinH}(\beta_z \gamma) = 0$ (see Fig. 38). Note that the fluctuations in Fig. 38 issue from the limited statistics due to the frequent binning of the sample.

¹¹Initial state radiation might cause an additional boost in transverse direction and a loss of virtual mass of the top quark. Then, it is possible, that the top quark becomes virtual which leads to a systematic shift towards lower top quark masses.

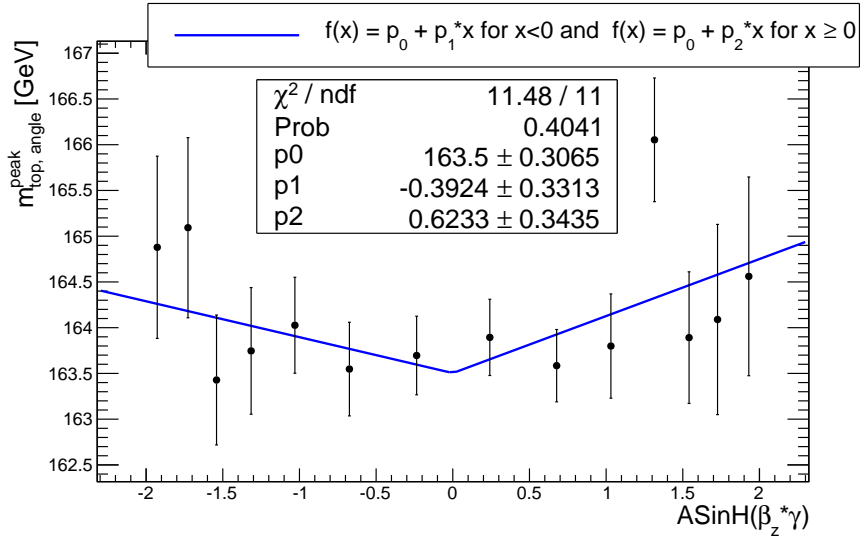


Figure 38: $m_{\text{top, angle}}^{\text{peak}}$ as a function of $\text{ASinh}(\beta_z \gamma)$. The fluctuations originate from the low statistics in each top quark $\beta_z \gamma$ - p_T bin due to the high number of bins necessary in this analysis.

This procedure is applied to all p_T -bins. Thus, for each top p_T -bin, one $m_{\text{top, angle}}^{\text{peak}}$ -value corrected in longitudinal direction, $m_{\text{top, angle}}^{\text{peak}} @ \beta_z \gamma = 0$, is obtained. This value is plotted as a function of the corresponding value of the top p_T as demonstrated in Fig. 39¹².

A linear function is fitted to $m_{\text{top, angle}}^{\text{peak}} @ \beta_z \gamma = 0$ as a function of p_T of the top quark. By extrapolating to $p_T = 0$, a correction of the effects of the Lorentz-Transformation in transverse direction is achieved.

Combining an extrapolation to $\beta_z \gamma = 0$ with an extrapolation to $p_T = 0$ yields an overall extrapolation to $\beta \gamma = 0$ and thus, to top quarks at rest. Consequently, the extrapolated value of $m_{\text{top, angle}}^{\text{peak}} @ \beta_z \gamma = 0$ to $p_T = 0$ is the obtained value of $m_{\text{top}}^{\text{angle}}$ for top quarks at rest.

Note that this value still needs to be calibrated to the simulated top quark mass. This procedure is described later in the text (section 10.3).

9.6. Results Obtained with Jet-Parton Matched Objects

According to Fig. 39 in the previous section, for a MC input top quark mass of 172.5 GeV, an estimator value of $m_{\text{top, angle}}^{\text{est.}} = 162.4 \pm 0.4$ GeV is obtained¹³. Note that the given uncertainty on $m_{\text{top, angle}}^{\text{est.}}$ is the uncertainty on the parametrization.

There are two main effects which can lead to the low value of the extrapolated estimator which is of the order of 10 GeV smaller than the MC input top quark mass. Initial state

¹²Note that the plotted values on the abscissa correspond to the mean value of p_T in that bin.

¹³Note that in order to translate the value of $m_{\text{top, angle}}^{\text{est.}}$ to terms of top quark mass, a calibration on the basis of the MC input top quark mass needs to be performed.

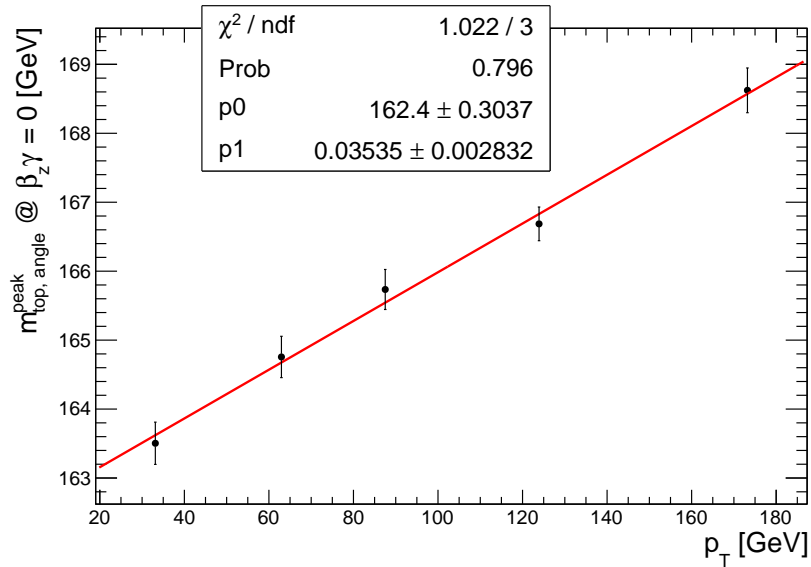


Figure 39: The extrapolated ($\beta_z \gamma = 0$) value of $m_{\text{top, angle}}^{\text{peak}}$ of each top quark p_T -bin as a function of the top p_T . Extrapolation to $p_T = 0$ is done by fitting a linear function to the data points.

radiation might cause a former real top quark to become a virtual top quark prior to its decay. As a consequence, the estimator might be shifted towards lower values. Final state radiation might cause an energy loss of the decay products as well as a distortion of the geometrical alignment of the decay products.

To examine whether effects of initial and final state radiation play a role, the analysis procedure is repeated but only events which contain exactly 4 jets are considered in the analysis. Initial and final state radiation cause supplementary jets issuing from the radiated gluons. In event selection cut C16 (see section 7.2) a jet multiplicity of 4-6 jets is required whereas 4 jets is the lowest number of jets generated in a lepton+jets decay (see section 3.2) and two other objects identified as jets are allowed. Initial and final state radiation is a possible origin of these additional jets¹⁴. The p_T -extrapolation function fitting $m_{\text{top, angle}}^{\text{peak}} @ \beta_z \gamma = 0$ as a function of the top p_T obtained when requiring exactly 4 jets in each event is shown in Fig. 40.

¹⁴Note that a 4-jet signature can also result if 5 jets were generated but one jet was misidentified as electron. But due to the **tight++** criteria applied on the electrons and Cut C18 requiring exactly one lepton in the event, this effect should only play a minor role.

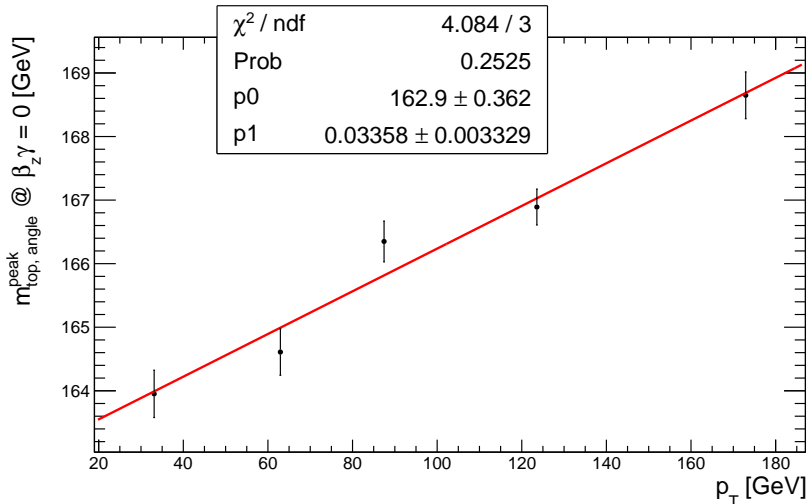


Figure 40: $m_{\text{top, angle}}^{\text{peak}} @ \beta_Z \gamma = 0$ as a function of the top p_T and the corresponding extrapolation function for the case of a required jet multiplicity of 4.

The extrapolated estimator extracted from Fig. 40 amounts to 162.9 ± 0.4 GeV and coincides within the uncertainty with the value obtained if processing the analysis with a required jet multiplicity of 4-6 jets (Fig. 39). Thus, initial and final state radiation do not contribute significantly to the shift towards lower values for the top quark mass estimators with respect to the input top quark mass.

In the process of deriving the top quark mass estimator (see section 8, equations (19)-(21) and (27)), the approximation of negligible jet masses was made. The jet rest energy is indeed much smaller than the total jet energy but could account for the shift of 5-6% towards lower top quark masses.

The extrapolated estimator of 162.4 ± 0.4 GeV is of course not the final result. For a top quark mass of 172.5 GeV in data, a measurement with this method would yield a result of 162.4 ± 0.4 GeV, therefore, the extrapolated estimator must be calibrated to the Monte Carlo input top quark mass. A so-called Calibration Curve is created plotting the extrapolated estimator as a function of various Monte Carlo input top quark masses in order to map the extrapolated estimator value to the simulated top quark mass. Top quark mass variation samples with $m_{\text{top}}^{\text{MC}}$ of 165.0 GeV, 167.5 GeV, 170.0 GeV, 172.5 GeV, 175.0 GeV, 177.5 GeV and 180.0 GeV are used in this analysis.

This Calibration Curve must be generated under analysis conditions equal to the condition of a data analysis. However, in data, no jet-parton matching is possible and therefore, a way must be found at first to handle the combinatorial background, which is detailed in section 10.

9.7. JSF-Variation Studies

In order to investigate the dependence of the resulting estimator on the jet energy scale, the analysis procedure is repeated but with different values of the jet scale factor JSF (see section 5.4.3). A JSF in the interval $[0.94;1.06]$ is multiplied to the jet 4-momentum vectors in order to simulate a variation of the jet energy scale. For each value of the JSF, the top quark mass estimator is calculated again and extrapolated to $\beta\gamma = 0$. The result is shown in Fig.41.

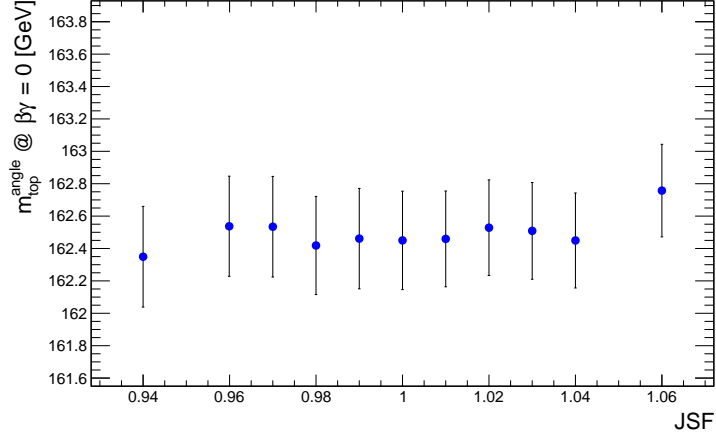


Figure 41: The extrapolated top quark mass estimator as a function of the jet scale factor JSF.

According to Fig.41, the extrapolated top quark mass estimator varies of the order of 200 MeV if varying the JSF by $\pm 6\%$. The data points even coincide within their error bars. This shows, that the extrapolated estimator $m_{\text{top}}^{\text{angle}} @ \beta\gamma = 0$ depends indeed very little on the jet energy scale and its uncertainty.

This is intuitive if visualizing the decay geometry (see section 8): A variation of the JSF which results in a variation of the jet energies only causes a variation of the momentum vectors' lengths but not of the geometry of the triangle spanned by the decay product as such: The angles are invariant to a change of the momentum vector length and thus, the estimator given by equation (28), section 8. The angle method is indeed largely independent on the jet energy scale as postulated.

10. Preparation of the Application of the Angle Method to ATLAS Data

In the previous section, studies were performed to test the general feasibility of the angle method. Now, steps are taken to prepare the method for an application to real ATLAS data. Unlike Monte-Carlo simulations, real data contain no information on the original partons. Therefore, object reconstruction cannot be done with jet-parton matching and one has to deal with combinatorial background. Bearing this in mind, the analysis procedure is transferred to the actual case.

10.1. Event Reconstruction Algorithm and Combinatorial Background

Previously, top quarks were reconstructed using the truth information in the Monte-Carlo samples. But truth information is no longer available in data. Top-quark pair reconstruction thus has to be done using properties of the top quark and its decay products.

Six objects are involved in the $t\bar{t}$ -decay: two b-jets, two light jets, one charged lepton and a neutrino.

Cut C18 requires exactly one lepton in the event, therefore, the assignment of the measured lepton to the lepton of the top quark decay is clear. In case of an event containing 4 jets, there are 24 possibilities of assigning the jets to the final-state-partons of the top quark decay. If requiring the light jets to be permutable, 12 possibilities remain¹⁵ and if including b-tagging, two possible assignments are still left. Considering that there are two solutions for the neutrino- p_z (see later), one ends up with 4 possible assignments. In case of an event with a jet multiplicity of 5, there are 12 possible solutions and for a 6-jet event, there are 24 possible solutions of assigning the objects (neutrino and jets). The event jet multiplicity distribution is shown in Fig. 42. Note that a cut (C16) was applied on the jet number requiring 4-6 jets in an event.

¹⁵The W-boson mass is indifferent under the exchange of the two light jets of its decay. An exchange of the two jets does neither affect the $m_{\text{top}}^{\text{angle}}$ -estimator.

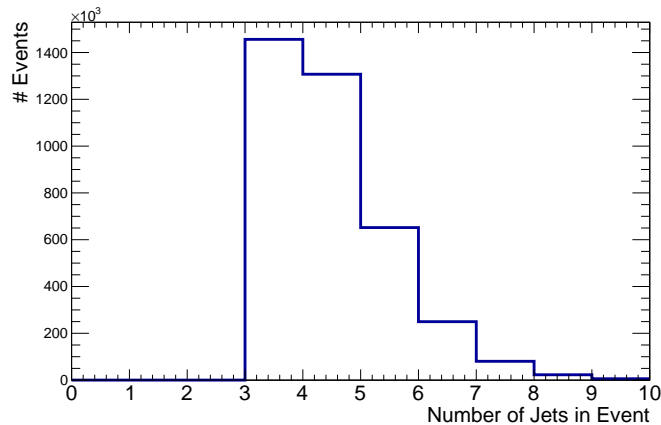


Figure 42: Histogram showing the jet multiplicity in the events of the sample.

Using the χ^2 -top-pair reconstruction algorithm (method of least squares), the most likely assignment is identified given the data [61].

The minimization of χ^2 makes use of the kinematic properties of the objects in order to reconstruct the $t\bar{t}$ -pair [16].

The kinematic properties of the most probable jet-parton assignment minimizes equation (30):

$$\chi^2 = \frac{(m_{b1,j1,j2} - m_{b2,l,\nu})^2}{\sigma_t^2} + \frac{(m_{j1,j2} - m_W)^2}{\sigma_W^2} + \frac{(m_{l,\nu} - m_W)^2}{\sigma_W^2} \quad (30)$$

[62]. The first term in equation (30) compares the 4-momentum invariant mass of the combination of a b-jet and two light jets to the 4-momentum invariant mass of the combination of another b-jet and the lepton and the neutrino. The underlying criterion is the equality of the top and the antitop quark masses.

The second and the third terms are minimal if the invariant masses of the combination of two light jets and of the combination of lepton and neutrino are closest to the W-boson mass¹⁶. All terms in equation (30) are weighted with either the width of the invariant mass peak of the W-Boson (σ_W) or of the top quark (σ_t) in order to account for the detector resolution. The values of σ_W and σ_t have been obtained by fitting a Crystal Ball function to the 4-momentum invariant mass distribution of the W-boson and the top quark which were reconstructed with jet-parton matching (see Fig. 43).

¹⁶PDG W-boson mass $m_W^{\text{PDG}} = (80.398 \pm 0.025) \text{ GeV}$ [63].

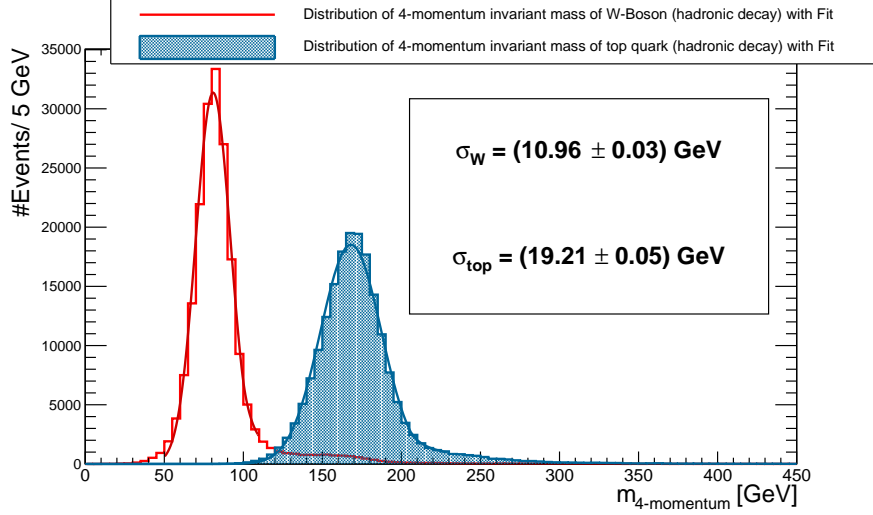


Figure 43: 4-momentum invariant mass distribution of the W-Boson (red) and of the top quark (coloured blue) and suitable parametrization (Crystal Ball function). W-Boson and top quark were reconstructed using jet-parton matching.

Note that b-tagging was used and the b-tagging efficiency was set to 70% [46]. Permutations with a non-b-tagged jet on a b-jet position were rejected whereas b-tagged jets were required not to be on a light-jet position.

The z-component of the neutrino momentum $p_{z,\nu}$ is necessary to obtain the neutrino 4-vector and was calculated assuming the W-boson mass:

$$m_W^2 = (E_l + E_{\nu,T})^2 - (p_{l,x} + p_{\nu,x})^2 - (p_{l,y} + p_{\nu,y})^2 - (p_{l,z} + p_{\nu,z})^2 \quad (31)$$

whereas m_W is the mass of the W-boson, E denotes the energy and p the momentum; the index T denotes the transverse component; the indices x,y and z are the coordinates in 3-dimensional Cartesian space and the index ν denotes the neutrino and l the lepton [64].

The election which solution for $p_{z,\nu}$ out of the two possible solutions of equation (31) corresponds to the neutrino was included in the χ^2 -minimization algorithm.

The resulting top quark invariant mass distributions can be seen in Fig. 44a and 44b. Fig. 44a shows the 4-momentum invariant mass distribution and Fig. 44b the $m_{\text{top}}^{\text{angle}}$ -distribution. Correct assignments are coloured orange and the combinatorial background, incorrect assignment, is hatched blue.

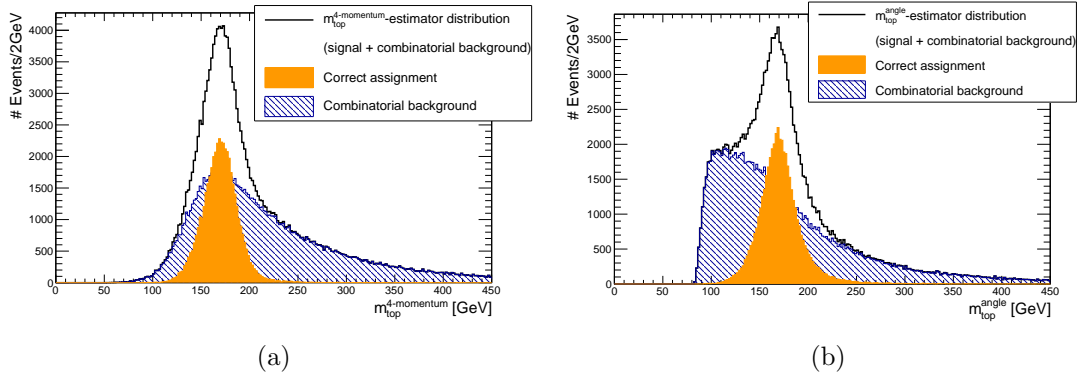


Figure 44: Distribution of the 4-momentum invariant top quark mass (Fig. 44a) and of the $m_{\text{top}}^{\text{angle}}$ -estimator (Fig. 44b) if reconstructing the top pair with the χ^2 -algorithm (black line). The coloured distributions visualize the share of correctly assigned events (smooth orange) and of the combinatorial background (hatched blue) on the total distribution (black line, no fill).

Signal efficiency and purity are quantities to evaluate the goodness of the reconstruction algorithm. The efficiency ϵ is the ratio of events which could be reconstructed successfully to the number of event which passed the selection cuts:

$$\epsilon = \frac{\text{Number of successfully reconstructed events}}{\text{Total number of events which passed the selection cuts}} \quad (32)$$

The purity π is the number of events with correctly assigned objects divided by the total number of successful reconstructions which consist of correctly assigned objects and combinatorial background:

$$\pi = \frac{\text{correct assignments}}{\text{correct assignments} + \text{combinatorial background}}. \quad (33)$$

Signal efficiency and purity in case of the χ^2 reconstruction algorithm are listed in Tab. 5.

ϵ	π
$(39.15 \pm 0.12)\%$	$(27.69 \pm 0.15)\%$

Table 5: Efficiency ϵ and purity π evaluated for the top pair reconstruction algorithm of equation (30).

Note that, however, the reconstruction algorithm is sensitive to the jet energy and therefore also to its uncertainty [16].

10.2. The adapted Top Quark Mass Estimator

In this analysis, ways must be found to deal with the combinatorial background. One way would be to apply cleaning cuts. Some possible cleaning cuts are described in [16]. This would further reduce the number of successfully reconstructed events, correct assignments would be affected as well. But a large number of successfully reconstructed events is essential in this method. As an alternative approach, one can make use of the fact that the combinatorial background also contains information on the top quark mass and include the combinatorial background in the analysis and define a new top quark mass estimator.

As a first step, the measured $m_{\text{top}}^{\text{angle}}$ -distribution shown in Fig. 44b must be parametrized with as few parameters as possible in order to guarantee a high stability of the fit. According to Fig. 44b, the distribution of the correct assignments (coloured orange) looks very much Gaussian-like whereas the combinatorial background (hatched blue) could be parametrized by a Landau distribution. This motivates a fit of a combination of a Landau and a Gauss distribution with the boundary condition that the peak position of the Gaussian is in the region where the distribution of the correct assignments peaks. The Landau has to approximate the peak at low values of $m_{\text{top}}^{\text{angle}}$. But the steep slope at the lower mass range and the slow decline at high values for $m_{\text{top}}^{\text{angle}}$ on the one hand and the peak on the other hand make it difficult to fit the distribution. Consequently, it is advisable to restrict the fit range. Studies were performed to find the most suitable fit range (examples: see Fig. 45a and 45b):

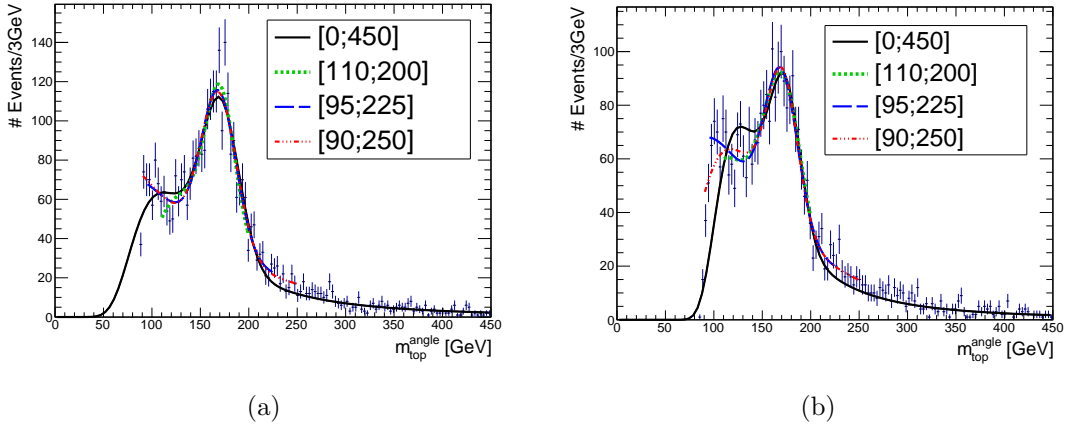


Figure 45: Examples of $m_{\text{top}}^{\text{angle}}$ distributions in a single $p_{\text{T}}\text{-}\beta_z\gamma$ -bin. Various fit ranges are tested in order to find the most reasonable fit range if parametrizing the distribution with a combination of a Landau and a Gauss function.

From Fig. 45a and 45b, it becomes obvious that the fit of the whole range is not reasonable as the steep slope at low $m_{\text{top}}^{\text{angle}}$ -estimator values cannot be described easily (see black line). A fit range which is slightly reduced (red dotted and dashed line) is still af-

ected too much by the steep slope at low $m_{\text{top}}^{\text{angle}}$ -values. If the range is too short like the case for the green dotted line in Fig. 45a and 45b, then, the shape of the combinatorial background in the low-mass regime is not approximated by the fit.

A good compromise is the blue dashed line (long dashes) which describes the distribution in the whole fit range reasonably well without restricting the range of the distribution too much. Later, it will be motivated, that a range as large as possible is indeed of advantage. For the following studies, a fit range of [95;225] is thus chosen.

A new top quark mass estimator is defined, including as well the information on the top quark mass provided by the combinatorial background. This is done to account for the possible correlation of the peak position of the Landau and of the Gaussian and for the correlation of the other fit parameters as well ¹⁷. The Gauss peak position will always be influenced to some degree by the combinatorial background. Furthermore, the distribution of the correctly assigned events is not entirely parametrized by the Gaussian and the Landau-function does not exclusively fit the background. This motivates the definition of the new top quark mass estimator $m_{\text{top, angle}}^{\text{weighted peak}}$ (equation (34)).

$$m_{\text{top, angle}}^{\text{weighted peak}} = \frac{I_L \cdot p_L + I_G \cdot p_G}{I_G + I_L} \quad (34)$$

where p_L and p_G are the peak positions of the Landau and the Gaussian and I_L and I_G are the integrals of the Landau and the Gaussian within the defined fit range. Note that the $m_{\text{top, angle}}^{\text{weighted peak}}$ -estimator is normalized and independent on the event number.

The correlation ρ describes the degree of linear dependence between two quantities. The correlation between two quantities x and y is calculated with equation (35) [65]

$$\rho = \frac{\langle xy \rangle - \langle x \rangle \langle y \rangle}{\sigma_x \sigma_y} \quad (35)$$

where the covariance is defined as

$$\text{cov}(x,y) = \langle xy \rangle - \langle x \rangle \langle y \rangle = \rho(x,y) \sigma_x \sigma_y \quad (36)$$

with σ_i , $i \in \{x,y\}$, standard deviation of x,y . ρ is a normalized quantity and can take values between -1 and +1 whereas the covariance also takes into account the variances of the quantities x and y . In case of a perfect linear dependence of the quantities x and y , ρ is equal to 1 (correlation) or -1 (anti-correlation). If x and y are independent, ρ equals to 0.

The coefficients of the correlation matrix $\rho_{m_{\text{top, angle}}^{\text{weighted peaks}}}$ specifying the correlation between the parameters of equation (34) denote to

¹⁷Direct investigation of the correlation of signal and combinatorial background is not possible due to lack of statistics in the samples with $m_{\text{top}}^{\text{MC}} \neq 172.5 \text{ GeV}$. Further details can be found later in the text.

$$\rho_{\text{m}_{\text{top, angle}}^{\text{weighted peaks}}} = \begin{pmatrix} \rho(\text{P}_G, \text{P}_G) & \rho(\text{P}_L, \text{P}_G) & \rho(\text{I}_G, \text{P}_G) & \rho(\text{I}_L, \text{P}_G) \\ \rho(\text{P}_G, \text{P}_L) & \rho(\text{P}_L, \text{P}_L) & \rho(\text{I}_G, \text{P}_L) & \rho(\text{I}_L, \text{P}_L) \\ \rho(\text{P}_G, \text{I}_G) & \rho(\text{P}_L, \text{I}_G) & \rho(\text{I}_G, \text{I}_G) & \rho(\text{I}_L, \text{I}_G) \\ \rho(\text{P}_G, \text{I}_L) & \rho(\text{P}_L, \text{I}_L) & \rho(\text{I}_G, \text{I}_L) & \rho(\text{I}_L, \text{I}_L) \end{pmatrix} =$$

$$\begin{pmatrix} 1 & 0.24 & 0.013 & 0.036 \\ 0.24 & 1 & -0.56 & -0.45 \\ 0.013 & -0.56 & 1 & 0.85 \\ 0.036 & -0.45 & 0.85 & 1 \end{pmatrix}$$

The component $\rho(\text{I}_G, \text{I}_L)$ sticks out immediately: With a correlation of 0.85, the value of the integral of the Gaussian and of the Landau distribution are very much correlated. All the other quantities are weakly to medium correlated.

Correlated parameters are inconvenient on the one hand, as strongly correlated quantities do not provide much new information due to their linear dependence and on the other hand, they introduce problems in the calculation of the uncertainties.

The uncertainty σ on a composite quantity g which is dependent on x and y , is calculated by $\sigma^2 = (\frac{\partial g}{\partial x})^2 \sigma_x^2 + (\frac{\partial g}{\partial y})^2 \sigma_y^2 + 2\rho \frac{\partial g}{\partial x} \frac{\partial g}{\partial y} \sigma_x \sigma_y$ whereas σ_x and σ_y are the standard deviations on the quantities x and y and ρ is the correlation coefficient between x and y . A strong correlation between x and y could therefore increase the uncertainty on the quantity g . A better idea would be to rewrite the expression in equation (34) to

$$\text{m}_{\text{top, angle}}^{\text{weighted peak}} = \frac{f \cdot \text{P}_L + \text{P}_G}{f + 1} \quad (37)$$

where $f = \frac{\text{I}_L}{\text{I}_G}$, and to obtain the parameter f directly from the fit.

The fitting function h_{fit} (equation (38)) must be slightly modified to include the parameter f in the fit:

$$h_{\text{fit}}(x) = N_G \cdot \text{Gaus}(x, \bar{x}_G, \sigma_G) + N_L \cdot \text{Landau}(x, \bar{x}_L, \sigma_L) \quad (38)$$

If normalizing the Gaussian and factoring out N_G (equation (39)), the integral over the Landau function equals the parameter f in equation (37).

$$h'_{\text{fit}} = N_G \cdot \left[\frac{1}{\sqrt{2 \cdot \pi \sigma_G^2}} \cdot \text{Gaus}(x, \bar{x}_G, \sigma_G) + \bar{N}_L \cdot \text{Landau}(x, \bar{x}_L, \sigma_L) \right] \quad (39)$$

$$f = \frac{\text{I}_L}{\text{I}_G} = \int_{95}^{225} \bar{N}_L \cdot \text{Landau}(x, \bar{x}_L, \sigma_L) \quad (40)$$

Equations (39) and (40) are based upon the fact that the integral over a normalized Gaussian yields 1.

But, this holds only true if the integral over the normalized Gaussian indeed yields 1, thus, the assumption has to be made, that the whole Gaussian is integrated in spite of the restricted fit range. Consequently, a too strict restriction of the fit range would not have been of advantage. In order to make sure that the whole Gaussian is within the fit range, the parameter range has to be restricted so that the peak position of the

Gaussian indeed coincides mostly with the distribution maximum.

An example of the fitting function according to equation (39) and the obtained fit parameters is shown in Fig. 46. The first line in the text box shows the result for the factor f obtained with the fitting function of equation (39) and in the second line the exact value for f (obtained by fitting a conventional Landau+Gauss, equation (38)) is printed for comparison, and in the third line, the ratio of the integral over the Gaussian in the restricted range to the integral over the Gaussian without a restriction of the fit range can be seen. Latter demonstrates, that the whole Gaussian can indeed assumed to be within the fit range.

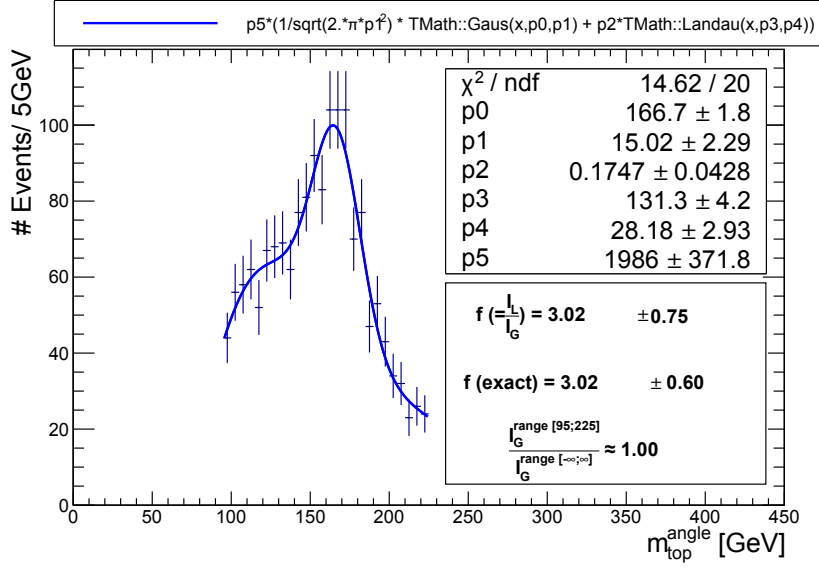


Figure 46: Example of the parametrization of the $m_{\text{top}}^{\text{angle}}$ -distribution. The value for the parameter f is given for the case of the approximation (equation (39)) in the first line of the text box. The exact value obtained with the conventional fit (equation (38)) is printed in line 2 of the text box. The last line gives information on the fraction of the area of the fitted Gaussian which is within the fit range.

Applying this new fitting function, the correlation between the components of the $m_{\text{top, angle}}^{\text{weighted peak}}$ -estimator could be reduced according to the correlation matrix ρ_{new} :

$$\rho_{\text{new}} = \begin{pmatrix} \rho(p_G, p_G) & \rho(p_L, p_G) & \rho(f, p_G) \\ \rho(p_G, p_L) & \rho(p_L, p_L) & \rho(f, p_L) \\ \rho(p_G, f) & \rho(p_L, f) & \rho(f, f) \end{pmatrix} = \begin{pmatrix} 1 & 0.12 & -0.014 \\ 0.12 & 1 & -0.086 \\ -0.014 & -0.086 & 1 \end{pmatrix}$$

According to the correlation matrix ρ_{new} , the Landau and Gauss peaks are weakly correlated ($\rho(p_L, p_G) \approx 0.12$). Therefore, the combinatorial background could probably be neglected in good conscience or given a much smaller weight in the calculation of the estimator since the top quark mass seems to be sensitive to the combinatorial background to a low degree due to the small correlation of p_L and p_G . But in order to do a quantitative evaluation of the correlation between signal and background, the dependence of the fit parameters of the Landau and the simulated top quark mass must be examined. An investigation yielding significant results cannot be done with the samples available due to the low statistics in the samples with $m_{\text{top}}^{\text{MC}} \neq 172.5$ GeV.

The covariance matrix element $\rho(p_L, p_G)$ was calculated in Fig. 47(a) as a function of the simulated top quark mass $m_{\text{top}}^{\text{MC}}$. By the means of that example it can be seen that the correlation between the signal peak (approximated by p_G) and the combinatorial background (approximated by p_L) is subject to large fluctuations and therefore, no reliable conclusions can be drawn for the correlation between the signal and the combinatorial background on the basis of the samples available.

Later, the analysis procedure has to be applied on other samples with $m_{\text{top}}^{\text{MC}} \neq 172.5$ GeV as well. The covariances (equation (36)) needed in order to calculate the uncertainty on the $m_{\text{top, angle}}^{\text{weighted peak}}$ -estimator are shown in Fig. 47 as a function of the simulated top quark masses.

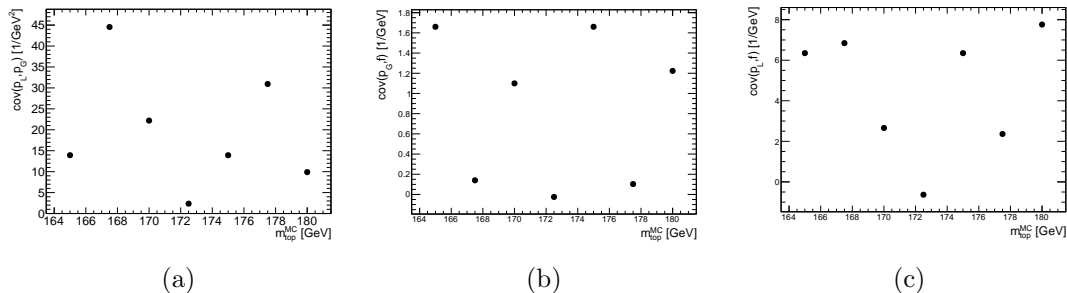


Figure 47: Covariance of the variables in equation (37) as a function of the simulated top quark mass $m_{\text{top}}^{\text{MC}}$.

Fig. 47 demonstrates the strong variability of the covariances with the simulated top quark mass. The magnitude of the covariance also depends on the standard deviations of the variables¹⁸, which are a measure of the fluctuations. The Monte-Carlo sample size determines how many entries are in the histograms and therefore is directly responsible for the stability of the fit of the $m_{\text{top}}^{\text{angle}}$ -distributions in the $\beta_z \gamma - p_T$ -bins. If the fits are less stable, the fit parameters will fluctuate more and this increases the covariance.

The sample with a simulated top quark mass of $m_{\text{top}}^{\text{MC}} = 172.5$ GeV contains the highest

¹⁸standard deviation of x : $\sigma_x = \sqrt{\frac{1}{n} \sum_{i=1}^n (x - \bar{x})^2}$ where \bar{x} denotes the expected value of x and n the number of data values [59].

number of top quarks which passed the pre-selection cuts (≈ 3.8 million) whereas all the other samples contain less than half that number (≈ 1.5 million). It is thus expected, that the covariances obtained with the $m_{\text{top}}^{\text{MC}} = 172.5$ GeV sample are more reliable than the covariances obtained with the other samples. Consequently, for all subsequent studies, the covariance matrix obtained with the $m_{\text{top}}^{\text{MC}} = 172.5$ GeV sample is used for the calculation of the uncertainties.

The proceeding of the analysis is the same as described in Section 9: The sample is divided into several p_{T} -bins (see Fig. 37 in section 9.5) and then, subsequently in bins of $\beta_z\gamma$. Then, the top quark mass estimator $m_{\text{top}}^{\text{angle}}$ (equation (28) in section 8) is calculated for each event in the $\beta_z\gamma$ - p_{T} -bin and the resulting distribution (see for example Fig. 46) is fitted with the modified Landau+Gauss function (see equation (39)).

For each of the p_{T} -bins, the resulting top quark mass estimator $m_{\text{top, angle}}^{\text{weighted peak}}$ is plotted as a function of $\text{ASinH}(\beta_z\gamma)$. Two examples are shown in Fig. 48.

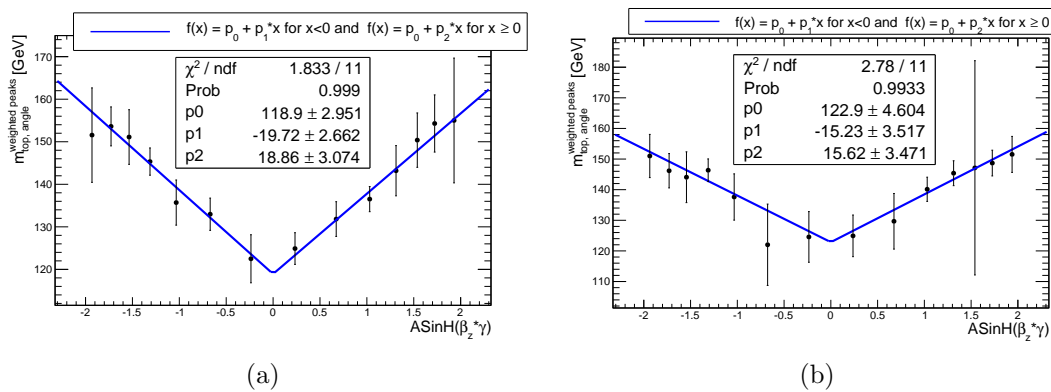


Figure 48: Example plots of the $m_{\text{top, angle}}^{\text{weighted peak}}$ estimator as a function of $\text{ASinH}(\beta_z\gamma)$. According to the fit statistics boxes, a fit of two linear functions intersecting at $\text{ASinH}(\beta_z\gamma) = 0$ turns out to be a reasonable fit.

A fit with two linear functions intersecting at $\text{ASinH}(\beta_z\gamma) = 0$ yields good results (see Fig. 48). As before, an extrapolation to $\text{ASinH}(\beta_z\gamma) = 0$ is done and the extracted value for $m_{\text{top, angle}}^{\text{weighted peak}}$ at $\text{ASinH}(\beta_z\gamma) = 0$ is plotted as a function of p_{T} (see Fig. 49).

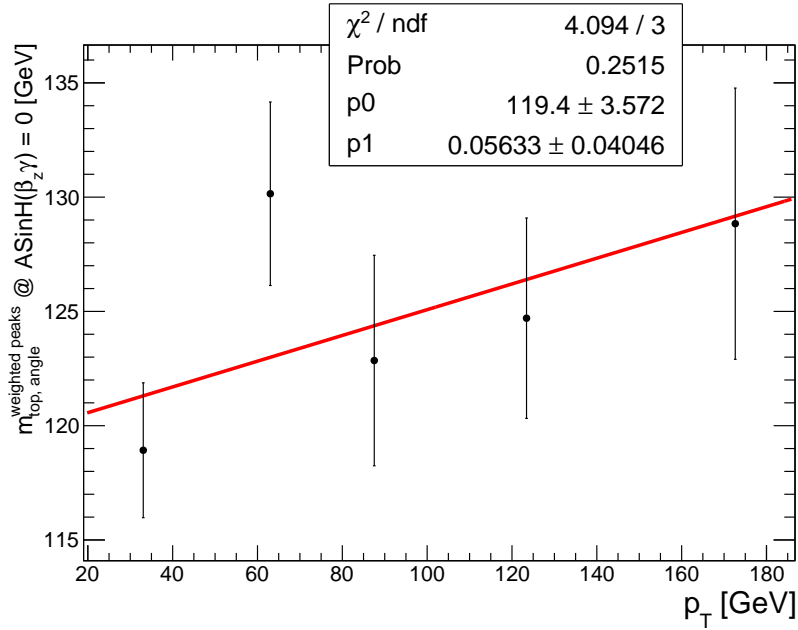


Figure 49: Resulting values for $m_{\text{top, angle}}^{\text{weighted peaks}}$ extrapolated to $\beta_z \gamma = 0$ as a function of p_T . The fit shows the linear extrapolation to $p_T = 0$ (see p0, fit statistics boxes).

According to Fig. 49, the measured top quark mass $m_{\text{top, angle}}^{\text{meas.}}$ in case of a simulated top quark mass of $m_{\text{top}}^{\text{MC}} = 172.5 \text{ GeV}$ is $m_{\text{top, angle}}^{\text{meas.}} = (119 \pm 4) \text{ GeV}$ (for a remark on this result, see section 10.3). Note that the uncertainty given includes only the uncertainty on the parametrization.

According to a previous comment, statistics in the top quark mass variation samples is not sufficient to investigate the feasibility of this estimator for an analysis. Within the scope of this thesis, it was not possible to generate further MC samples with larger statistics. Thus, in the following, the next analysis steps are presented and performed with the statistics available. In order to be able to do that analysis, some approximations have to be made in the course of the next subsections, whereas the first approximation is to fix the correlations to the values obtained with the $m_{\text{top}}^{\text{MC}} = 172.5 \text{ GeV}$ sample for the uncertainty calculation.

10.3. Calibration of the Angle Method

It was shown in the previous subsection, that a Monte-Carlo top quark input mass of $m_{\text{top}}^{\text{MC}} = 172.5 \text{ GeV}$ yields an extrapolated top quark mass estimator of $m_{\text{top, angle}}^{\text{weighted peaks}} = (119 \pm 4) \text{ GeV}$ if measuring the top quark mass with the presented approach.

As a next step, the Calibration Curve is generated in order to map the measured top quark mass estimator $m_{\text{top, angle}}^{\text{meas.}}$ onto the Monte-Carlo input top quark mass $m_{\text{top}}^{\text{MC}}$. If a measurement with data is performed, $m_{\text{top, angle}}^{\text{meas.}}$ can be related to the final result for the

top quark mass with the Calibration Curve.

Top quark mass variation samples are available simulating top quark masses of 165.0 GeV, 167.5 GeV, 170.0 GeV, 175.0 GeV, 177.5 GeV and 180.0 GeV. For each of these samples, the extrapolated top quark mass estimator $m_{\text{top, angle}}^{\text{weighted peaks}}$ is calculated. But these samples contain less produced top quarks than the $m_{\text{top}}^{\text{MC}} = 172.5$ GeV sample. In fact, statistics are reduced by more than a factor of 2: While the $m_{\text{top}}^{\text{MC}} = 172.5$ GeV sample contains about 3.8 Mio. events (after the pre-selection cuts), all the other samples contain around 1.5 Mio. events.

This directly affects the results: If the $m_{\text{top}}^{\text{angle}}$ -distributions of the top quarks in the $\beta_z\gamma$ - p_T -bins contain less events, the fits to the distributions are more unstable and/or yield entirely different fit parameters. Three examples of resulting $m_{\text{top, angle}}^{\text{weighted peak}}$ values as a function of $\text{ASinH}(\beta_z\gamma)$ are shown along with the extrapolation function in Fig. 50a, Fig. 50c and Fig. 50e.

Fig. 50a, Fig. 50c and Fig. 50e demonstrate that some of the fits to $m_{\text{top, angle}}^{\text{weighted peak}}(\text{ASinH}(\beta_z\gamma))$ are distorted by some outliers. These outliers are caused by fluctuations of the fits to the $m_{\text{top}}^{\text{angle}}$ -distributions which are due to the low statistics in the top quark mass variation samples. The examples in Fig. 48 of section 10.2 of $m_{\text{top, angle}}^{\text{weighted peak}}(\text{ASinH}(\beta_z\gamma))$ in case of the Monte-Carlo sample with higher statistics ($m_{\text{top}}^{\text{MC}} = 172.5$ GeV) demonstrate that the slope parameter takes values of around ± 15 GeV, whereas the slope parameters in Fig. 50a, 50c and 50e, are particularly low or even have the wrong sign. Fig. 50b, 50d and 50f indicate that outliers become less important if imposing limits on the slope parameters.

Examining the fits of the $m_{\text{top, angle}}^{\text{weighted peak}}(\text{ASinH}(\beta_z\gamma))$ distributions for all top quark mass variation samples showed that most reasonable fits have a slope parameter of at least $|7|$ GeV. It is not reasonable to set a stricter condition on the slope parameter as it is difficult to find a common trend among all the fits and one runs the risk of introducing a bias by forcing the slope parameter of the fit to be higher than given by the $m_{\text{top, angle}}^{\text{weighted peak}}(\text{ASinH}(\beta_z\gamma))$ distributions. In the following, the slope parameter must be greater than $|7|$ GeV as a second approximation made to account for the low statistics in the samples with $m_{\text{top}}^{\text{MC}} \neq 172.5$ GeV. Note that this supplementary boundary condition does not influence the result obtained with the $m_{\text{top}}^{\text{MC}} = 172.5$ GeV sample.

Before generating the Calibration Curve, another matter has to be considered: The offset parameter of the p_T extrapolation function is correlated to the slope, therefore the calibration of the top quark mass depends on the slope parameter as well as on the offset parameter of the p_T extrapolation function. These two parameters have to be included in the calibration. Although the statistics of the MC samples other than $m_{\text{top}}^{\text{MC}} \neq 172.5$ GeV are very low, it can be noted that the slopes of the p_T extrapolation functions do not scatter much and coincide in almost all cases within their error bars (see Fig. 51). Therefore, as a third approximation, the slope can be fixed to the value obtained with a constant fit (see Fig. 51).

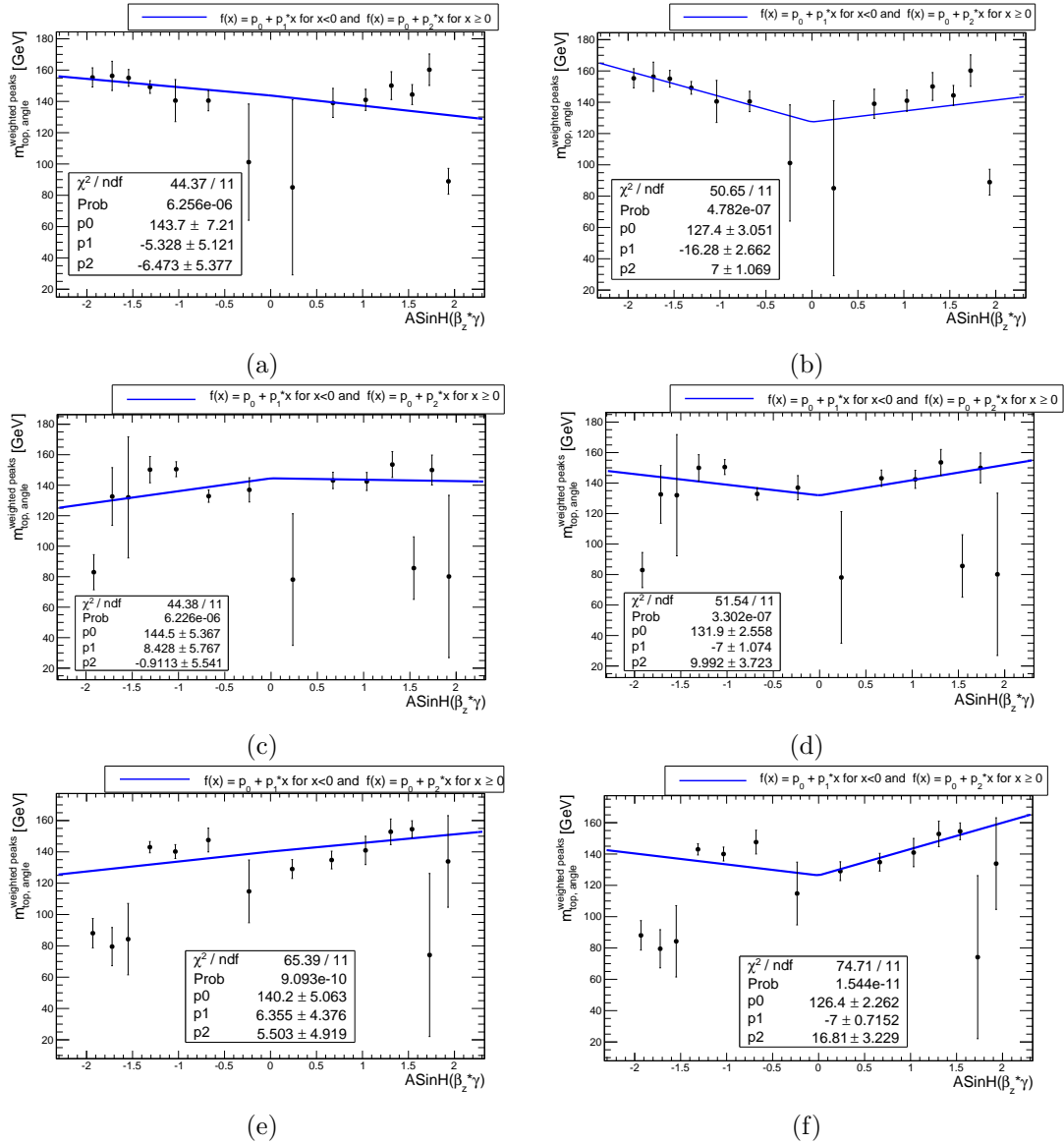


Figure 50: The panels (a) ($m_{\text{top}}^{\text{MC}} = 180.0$ GeV), (c) ($m_{\text{top}}^{\text{MC}} = 175.0$ GeV) and (e) ($m_{\text{top}}^{\text{MC}} = 175.0$ GeV) each show the extrapolation function to $\beta_z \gamma = 0$ without the restriction of the slope parameter range and the panels (b), (d) and (f) each show the fit requiring the slope parameters to be $> |7|$. In case of a non-restricted slope parameter, the fit is governed by fluctuations of the data points.

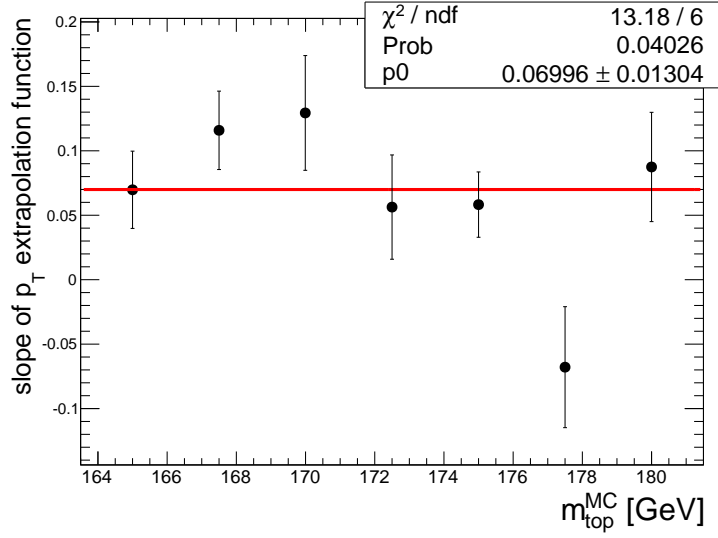


Figure 51: Slope of the p_T extrapolation function as a function of the MC input top quark mass $m_{\text{top}}^{\text{MC}}$. Fit of a constant function in order to evaluate the average slope under consideration of the uncertainties on the data points.

The results for the Calibration Curve are shown in Fig. 52a (variable slope of p_T extrapolation function) and Fig. 52b (fixed slope of p_T extrapolation function).

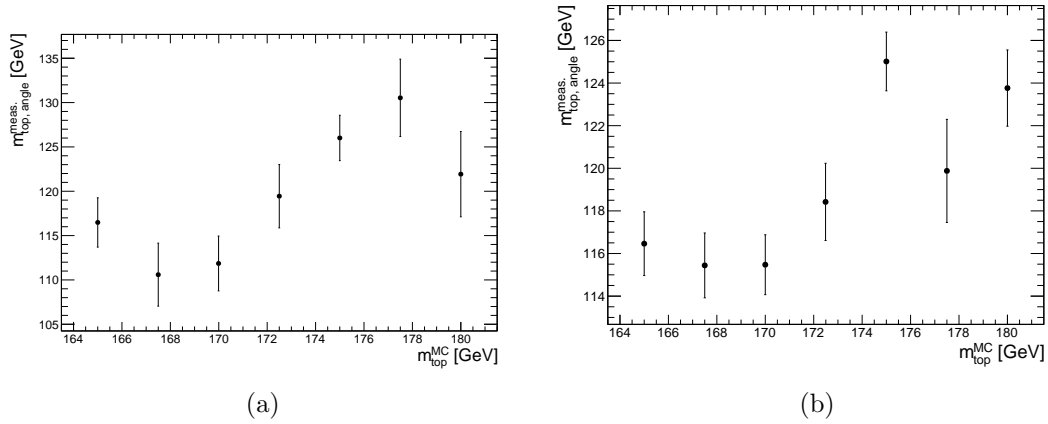


Figure 52: (a): Calibration curve obtained without fixing the slope parameter, (b): Calibration Curve obtained if fixing the slope parameter of the p_T extrapolation function.

For a quantitative proof that fixing the slope of the p_T extrapolation function also reduces the uncertainty on the calibration, the uncertainties on the calibrated final result due to the parametrization of the Calibration Curve for the case of a fixed and a variable p_T extrapolation function slope are compared. The measurement applied on data would

yield a resulting value $m_{\text{top, angle}}^{\text{meas}}$. This value is then translated using the Calibration Curve to the final result for the top quark mass. Considering the uncertainties on the parameters of a linear fit to the Calibration Curves (see Fig. 53a and 53b) and their correlation, the Gaussian uncertainty issuing from the parametrization is calculated if not fixing the slope $\sigma_{m_{\text{top}}; p_{\text{T}}\text{-slope free}}^2$ (Fig. 53a) and if fixing the slope ($\sigma_{m_{\text{top}}; p_{\text{T}}\text{-slope fixed}}^2$) (Fig. 53b).

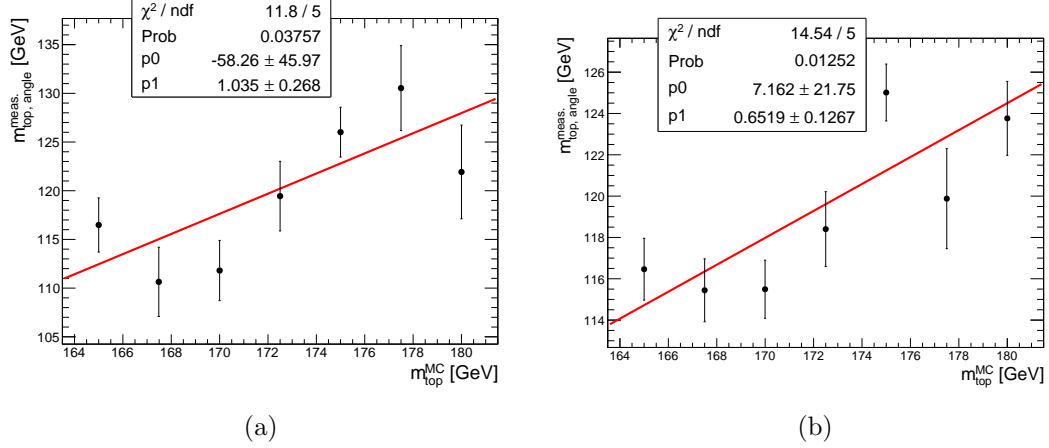


Figure 53: Linear fit to the data points of the Calibration Curves of Fig. 52a and 52b.

The uncertainties are compared by calculating the difference between these uncertainties, $\sigma_{m_{\text{top}}; p_{\text{T}}\text{-slope free}}^2 - \sigma_{m_{\text{top}}; p_{\text{T}}\text{-slope fixed}}^2$ (see Fig. 54). If the function value of $\sigma_{m_{\text{top}}; p_{\text{T}}\text{-slope free}}^2 - \sigma_{m_{\text{top}}; p_{\text{T}}\text{-slope fixed}}^2$ is positive, the uncertainty on the final result of the top quark mass due to the parametrization in case of a variable slope is bigger, if the uncertainty is negative, the uncertainty in case of a fixed p_{T} -slope is bigger. According to Fig. 54 and considering the fact that in case of a top quark mass around 172 GeV, the measured top quark mass is around 118-120 GeV, the uncertainty on the measured top quark mass issuing from the parametrization is smaller in case of a fixed p_{T} -slope.

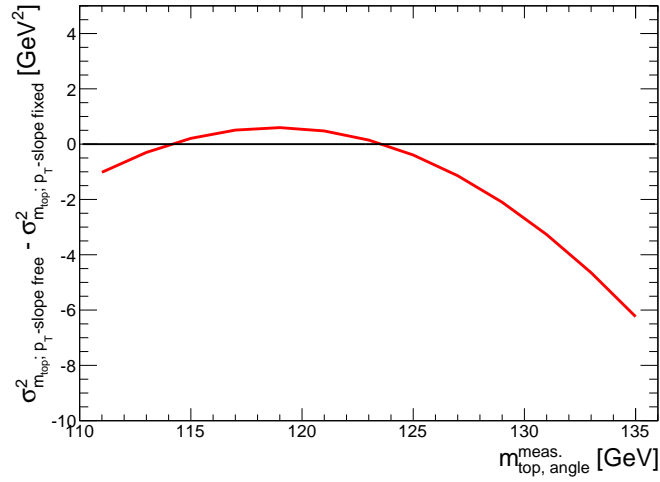


Figure 54: Comparison of the uncertainty on the calibrated result for the top quark mass due to the parametrization of the Calibration Curve as a function of the measured top quark mass estimator is shown. If the function returns a positive value, the uncertainty is bigger in case of a Calibration Curve obtained without fixing the slope of the p_T extrapolation function.

In Fig. 55, the absolute uncertainty $\sigma_{m_{top}}^{par}$ issuing from the uncertainty on the parametrization of the Calibration Curve in case of a fixed p_T -slope is plotted as a function of the measured top quark mass estimator.

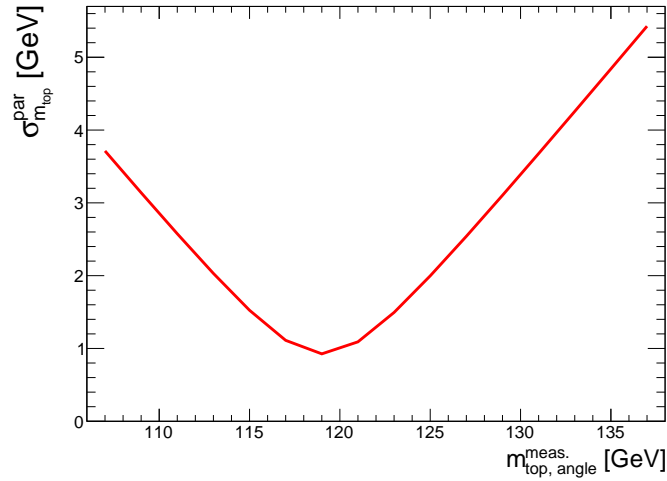


Figure 55: Absolute uncertainty on the calibrated value for the top quark mass due to the parametrization of the calibration curve as a function of the measured estimator.

The uncertainty due to the parametrization of the calibration is expected to be around 1.0-1.5 GeV.

In spite of the fact that the Calibration Curve does not have enough precision to calibrate a measurement, it could be shown, that fixing the p_T slope improves the result.

10.4. Evaluation of the Uncertainty due to the Jet Energy Scale

In the following, the impact of the uncertainty on the jet energy scale is examined. To evaluate the uncertainty due to the uncertainty on the jet energy scale, energies and momenta are varied by up to 6% by multiplying a factor in the interval [0.94;1.06] to the jet 4-momenta. The extrapolated top quark mass estimator $m_{\text{top, angle}}^{\text{weighted peaks}}$ is calculated for 11 intermediate values of the JSF and plotted as a function of the JSF. The result can be seen in Fig. 56a.

In Fig. 56b, a linear function is fitted to the data points. The light gray fitting function (dashed line) and the corresponding fit parameters (in gray) demonstrate the fit to all data point whereas the red fit and the corresponding fit parameters (in red) does not consider the outlier at JSF = 1.01 (light gray data point). This improves the fit (compare fit statistics box).

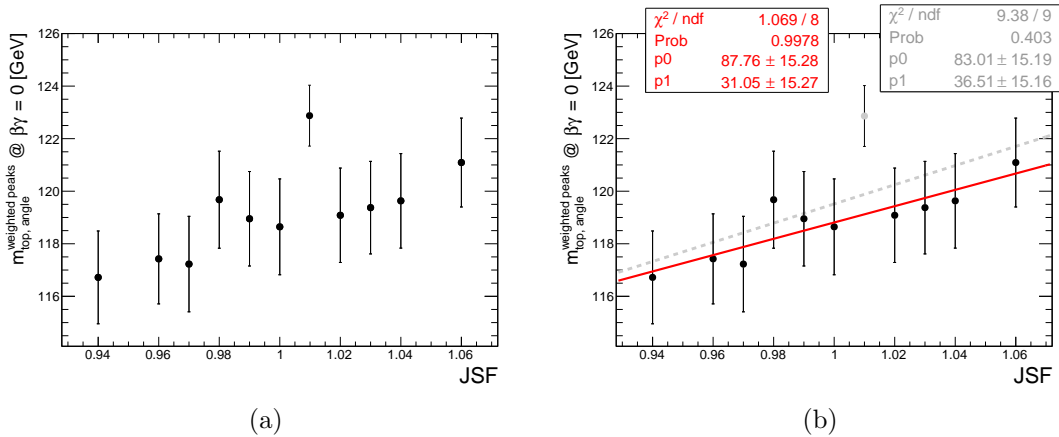


Figure 56: Variation of the extrapolated value of $m_{\text{top, angle}}^{\text{weighted peaks}}$ with the JSF. On panel (b), a fit to the data is performed. In order to improve the goodness of the fit, the outlier at JSF = 1.01 is not considered in the fit (red line). The light gray dashed line shows the fit if considering all the data points.

The uncertainty on the jet energy scale (JES) varies with the jet energy and the rapidity. The higher the energy and the more central the jet, the lower the uncertainty on the jet energy. For example, for central jets ($|\eta| < 1.2$) with a small transverse energy (≈ 17 GeV), the uncertainty was determined to 3% at $\sqrt{s} = 7$ TeV center-of-mass energy in [45], to 2% for jets with a transverse energy of ≈ 25 GeV and to 1% for jets with $55 < p_T^{\text{jets}} < 500$ GeV. The uncertainty for forward jets ($|\eta| > 1.2$) is higher, for example

for very forward jets ($p_T \approx 25 \text{ GeV}$ and $|\eta| \approx 4$), an uncertainty of 5% is observed. According to [45], the total JES uncertainty for an event sample of $t\bar{t}$ -pairs decaying in the lepton+jets channel of 2011 data, considering all detector and physics effects and background processes in the collider is below 3% for jets with $60 < p_T^{\text{jet}} < 1000 \text{ GeV}$.

Assuming an average uncertainty on the JSF of 3%, the uncertainty denotes to

$$\Delta m_{\text{top, angle}}^{\text{weighted peaks}} = 0.03 \cdot p1 = 0.03 \cdot (3 \pm 2) \cdot 10^1 = 0.9 \text{ GeV}$$

where $p1$ is the slope of the fitting function to $m_{\text{top, angle}}^{\text{weighted peaks}}$ as a function of the JSF in Fig. 56b.

10.5. Method Validation

Before a measurement on real data can be performed, the reliability of the method must be tested, that means whether the MC input top quark mass is consistent with the calibrated top quark mass. The so-called Method Validation gives information whether the method works as expected, whether a bias was introduced and that therefore the final result must be corrected by a constant offset or whether the method is entirely based on incorrect assumptions.

The developed approach in the angle method analysis, the 2-step analysis correcting for longitudinal and transverse effects of the jet energy measurement uncertainty, developed according to parton level studies, must be verified at first.

For this task, 500 pseudo-datasets are created for each of the mass points based on the available MC sample and the analysis is applied on these pseudo-datasets. In order to reproduce a realistic analysis, the datasets are scaled to the number of $t\bar{t}$ events expected in data based on the $m_{\text{top}}^{\text{MC}}$ -specific cross-section of $t\bar{t}$ -production, its k-factor and the luminosity (see Tab. 4, section 6). The number of events in these pseudo-data samples is varied according to Poissonian statistics. Randomly, pairs of values $(p_T, \beta_z \gamma)$ are drawn according to the distribution of $(p_T, \beta_z \gamma)$ -pairs in the samples. A value of $m_{\text{top}}^{\text{angle}}$ is drawn from the corresponding $m_{\text{top}}^{\text{angle}}$ -distribution. The histograms necessary for the analysis are created anew on the basis of the triples of values drawn.

Each of the created pseudo-datasets returns a value for the extrapolated top quark mass estimator ($= m_{\text{top, angle}}^{\text{weighted peaks}} @ \beta \gamma = 0$). So, in total, for each top quark mass variation sample, a distribution of extrapolated top quark mass estimators containing 500 entries results (example: see Fig. 57).

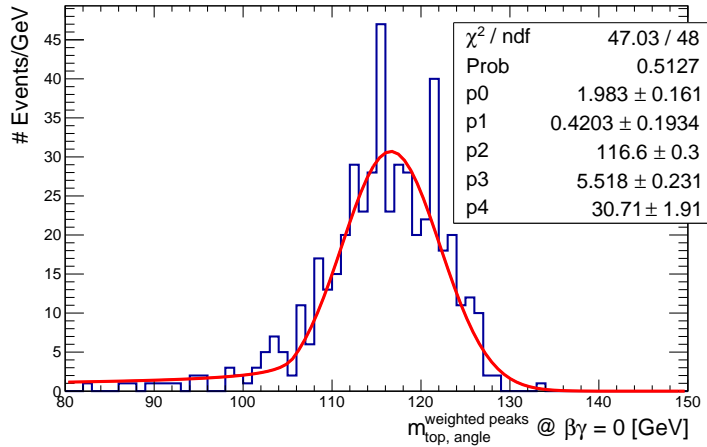


Figure 57: Distribution of extrapolated top quark mass estimators $m_{\text{top, angle}}^{\text{weighted peaks}}$ obtained by applying the analysis method on the 500 pseudo-data samples generated on the basis of the $m_{\text{top}}^{\text{MC}} = 172.5 \text{ GeV}$ Monte-Carlo sample.

The distribution in Fig. 57 looks like a slightly asymmetric Gaussian and is therefore fitted with a Crystal Ball Function. The top quark mass estimator obtained from the Method Validation procedure for the corresponding mass point is the peak position of the fit function. Considering the goodness of fit, the peak position uncertainty is scaled by the factor [8]

$$S = \sqrt{\frac{\chi^2}{\text{ndf} - 1}}. \quad (41)$$

The uncertainty has to be scaled yet with another factor accounting for the correlations between the pseudo-datasets: Selecting events with replacement in order to create the pseudo-datasets means that the same event may occur twice or more times in the pseudo-datasets. Drawing n events from a sample containing N events only yields N/n independent pseudo-datasets, which in this case amounts to only 4-10 independent datasets. This is considered by scaling the uncertainty σ on the resulting top quark mass estimator obtained by the method validation procedure by

$$\sigma_{\text{corrected}} = \sigma \cdot \sqrt{\frac{1}{N_{\text{samples}}} + (1 - e^{-n/N})} \quad (42)$$

whereas N_{samples} is the number of created pseudo-datasets, n the number of events drawn from a sample containing N events. A more detailed description and the derivation of this factor can be found in [66] and [67].

Fig. 58 compares the Calibration Curve (blue) and the underlying data points (blue triangles) with the results obtained with the Method Validation (red dots) and the corresponding fit (red).

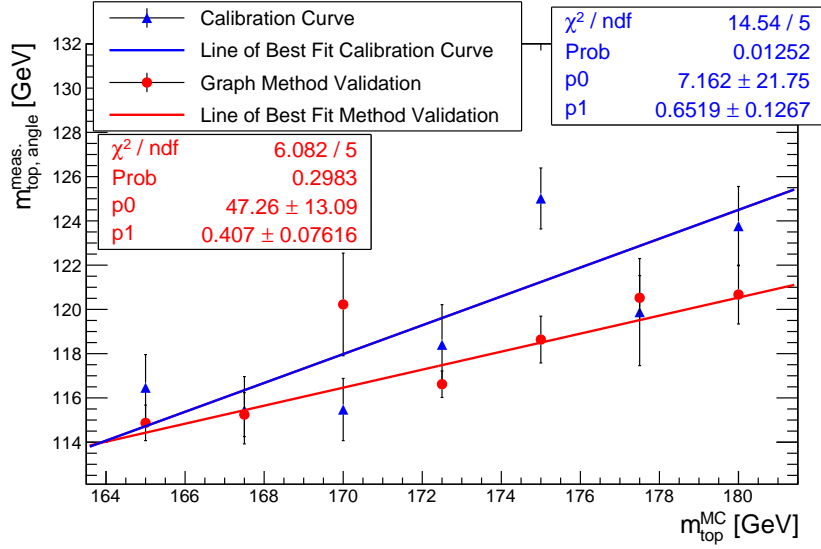


Figure 58: The Calibration Curve (blue) superimposed with the results obtained with the Method Validation (red). The data points on which the fit is based are drawn as red dots (Method Validation results) and blue triangles (Calibration Curve).

Comparing the Calibration Curve with the fit to the Method Validation data points leads to the conclusion that the Method Validation data points are systematically shifted towards lower top quark mass estimator values.

On the basis of the Calibration Curve, the top quark estimator values obtained with the Method Validation procedure, are converted to top quark masses and compared to the MC input top quark mass. The result can be seen in Fig. 59a plotted as a function of the MC input top quark mass. A fit of a constant (Fig. 59b) is applied to Fig. 59a visualizing the systematic shift towards lower top quark masses of the measured value with respect to the MC input top quark masses. Thus, the measured top quark mass which was obtained by converting the measured top quark mass estimator on the basis of the Calibration Curve has to be corrected towards higher top quark masses by (3.0 ± 0.5) GeV.

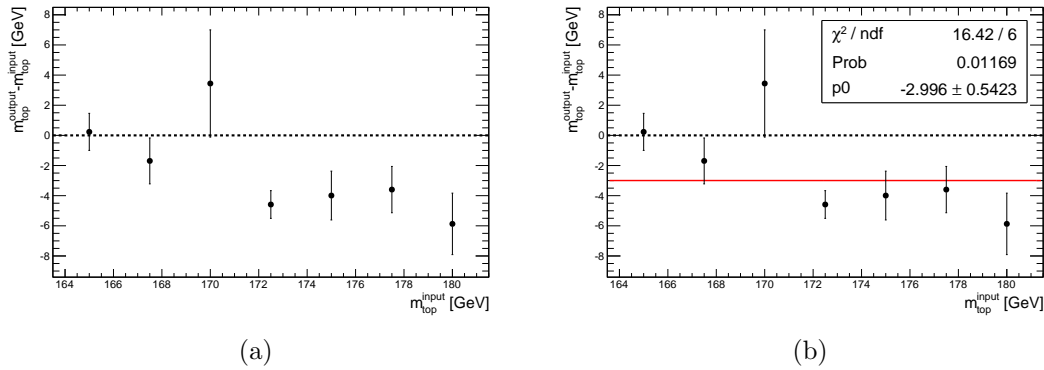


Figure 59: Comparison of the calibrated top quark masses obtained with the Method Validation with the MC input top quark mass. The deviation from the constant line intersecting the ordinate at zero gives information on the difference to the MC input top quark mass. Right panel: Fit to the residuals.

The method is reliable but yields results which are shifted systematically towards lower top quark masses and the obtained result for the top quark mass has to be corrected towards higher top quark masses by (3.0 ± 0.5) GeV.

The construction of the estimator as in equation (34) and (37) in section 10.2 was an attempt to include more statistics in the calculation of the estimator as well as to consider possible correlations of signal and combinatorial signal fraction. Unfortunately, the approach turned out to be not successful or not feasible due to lack of statistics: Qualitative studies on the correlation of signal and background (calculation of $\rho(p_L, p_G)$) showed, that p_L only depends very little on the top quark mass. But the correlation between the simulated top quark mass and the fit parameters of the Landau must be checked quantitatively if samples with higher statistics are available. Furthermore, the uncertainty of the calibrated top quark mass due to the uncertainty on the parametrization of the calibration is also expected to be too large as due to lack of statistics, the Calibration Curve is too imprecise. In order to decide if and to which degree the combinatorial signal fraction must be included in the calculation of the estimator, the correlation of the Landau peak position to the simulated top quark mass must be examined. To construct an improved estimator, the correlation of the Landau and the Gauss peak position to $m_{\text{top}}^{\text{MC}}$ could be examined and equation (34) could be modified such that the weights are given by the correlation to $m_{\text{top}}^{\text{MC}}$ instead of the relative integrals. But significant results for the correlation can only be archived with top quark mass variation samples which include a larger number of events. A preliminary conclusion drawn from the results of this section is that the weight of the combinatorial background in the estimators given by equations (34) and (37) is too large compared to the correlations calculated with the $m_{\text{top}}^{\text{MC}} = 172.5$ GeV sample. Therefore, in the next section, a new possible estimator is introduced which only considers the Gauss peak of the Landau+Gauss fit and therefore mainly includes information provided by correctly assigned combinations.

11. Improving the Analysis Method

Although the combinatorial background also yields a dependence on the top quark mass, it contains little information on the top quark mass compared to the signal peak. Nevertheless, due to the high fraction of combinatorial background (more than 70%), the contribution of the combinatorial background to the top quark mass estimator introduced in section 10 is very dominant.

As the $t\bar{t}$ -pairs were reconstructed using invariant mass information, the combinatorial background is largely dependent on the 4-momentum invariant mass of the reconstructed top quark and therefore on the JSF. The dependence on the JSF was also shown in section 10.4. To reduce on the one hand the dependence on the JSF introduced by the combinatorial background and on the other hand use to a full extent the information provided by the signal peak, studies using another approach are performed.

11.1. Improving the $t\bar{t}$ -pair Reconstruction Algorithm

Predominately the first term of the $t\bar{t}$ -pairs reconstruction algorithm in equation (30) (section 10.1) introduces combinatorial background. The other two terms, where the 4-momentum invariant mass of two light jets and of lepton and neutrino are compared with the mass of the W-boson, are not so much prone to introducing background as there is a strong constraint on their invariant mass. Combinations which are as close to the W-boson mass as possible are strongly favoured, also due to the larger weight on these terms.

On the other hand, there is no constraint on the invariant mass of the top quark. In the first term of equation (30), combinations with a small difference in the 4-momentum invariant mass of a b-quark combined with two light jets and another b-quark combined with the lepton and the neutrino, are favoured. Even though the W-boson can be reconstructed quite reliably, it is possible that even though the b-quark of the hadronic and leptonic top quark decay are swapped, the criterion of as little 4-momentum invariant mass difference as possible between the top and the antitop is met better.

One could try to reduce this combinatorial background caused by the exchange of the two b-quarks by introducing a constraint on the 4-momentum invariant mass of the top quark. Monte-Carlo samples available for this analysis are within a mass range of 165 GeV and 180 GeV and one could try to restrict the 4-momentum invariant mass of the combinations to an interval of [165,180] GeV when using a Monte-Carlo sample with a simulated top quark mass of 172.5 GeV.

The top quark mass estimator distribution $m_{\text{top}}^{\text{angle}}$, resulting of equation (28) (section 8) is plotted in Fig. 60.

Two options of a refined reconstruction method are plotted: To obtain the distribution indicated by the blue line, only a restriction on the hadronically decaying top quark is set. In case of the red distribution, combinations of the decay products of both top quarks have to have a 4-momentum invariant mass within the given range.

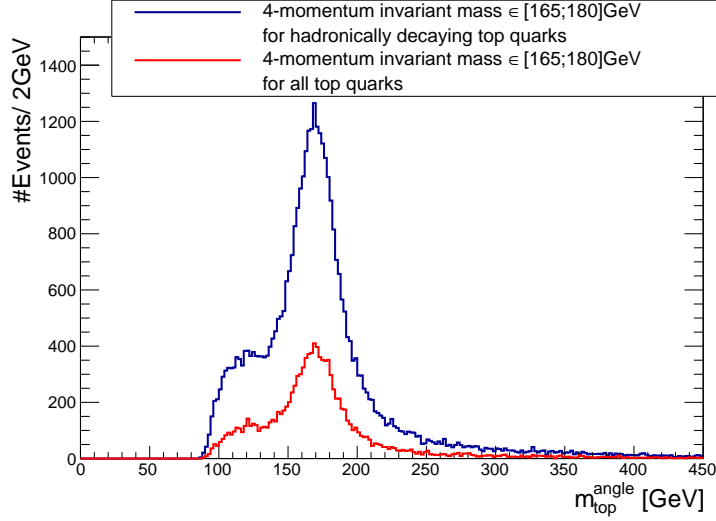


Figure 60: $m_{\text{top}}^{\text{angle}}$ invariant mass distribution if requiring the 4-momentum invariant top quark mass to be within a range of $[165;180]$ GeV. Red distribution: restrict top as well as antitop 4-momentum invariant mass, blue distribution: constraint only on hadronically decaying top quark mass.

From Fig. 60, it becomes obvious, given the large number of divisions of the sample necessary for this analysis, that the stricter condition resulting in the red distribution is not suitable for this analysis due to lack of statistics. Therefore, in continuation, the condition that only the decay products of the hadronically decaying top quark must have a 4-momentum invariant mass within the interval of $[165;180]$ GeV (blue distribution in Fig. 60) is applied.

Applying this supplementary condition, the signal purity (see equation (33), section 10.1) could be raised from $(27.69 \pm 0.15)\%$ to $(44.9 \pm 0.5)\%$ but with the cost of a reduced number of events passing the reconstruction algorithm - the number of available events was reduced by a factor of almost 4.5. The contribution of correct assignments and combinatorial background is shown in Fig. 61.

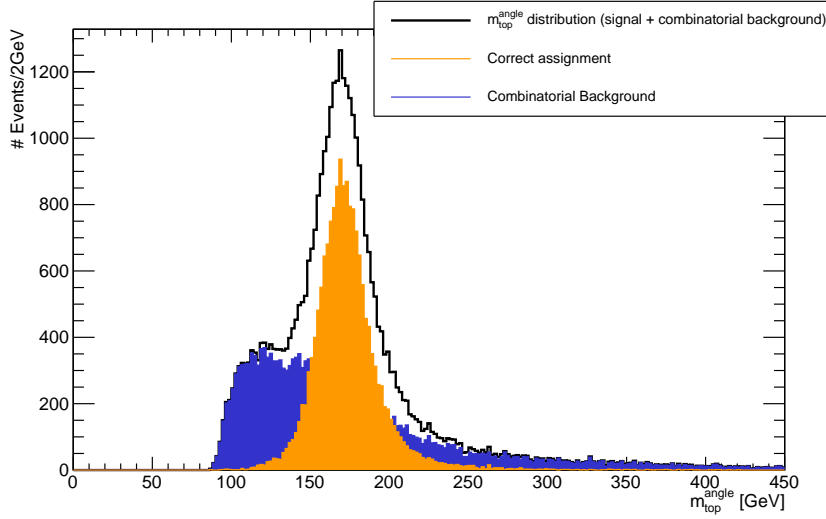


Figure 61: Visualization of the share of correct assignments (orange) to combinatorial background (blue) in the $m_{\text{top}}^{\text{angle}}$ distribution.

In order to keep statistical fluctuation of the parametrization at a reasonable level, one has to reduce the number of p_{T} and $\beta_z \gamma$ bins. Latter is reduced from 14 to 8 and former from 5 to 4 bins.

11.2. The New Top Quark Mass Estimator

With a fraction of 55% of the reconstructed events, the combinatorial background would still contribute to a high level to the top quark mass estimator introduced in section 10.2 as the Landau integral would, even after a restriction of the fit range, still be a large contribution to the total integral. Presumably, as already stated in section 10.1, it is the combinatorial background that introduces a dependence on the JSF so it is desirable to eliminate this contribution as far as possible. The combinatorial background also contains information on the top quark mass but not as much as the signal peak. An analysis approach therefore would be to fit the function like before with a Landau and a Gaussian function but to only consider the peak position of the Gaussian in the analysis. This new top quark mass estimator is denominated $m_{\text{top, angle}}^{\text{Gauss peak}}$.

As a first step, a suitable fit range has to be defined in order to approximate best the peak position of the Gaussian. In Fig. 62, a few examples of possible fit ranges are compared.

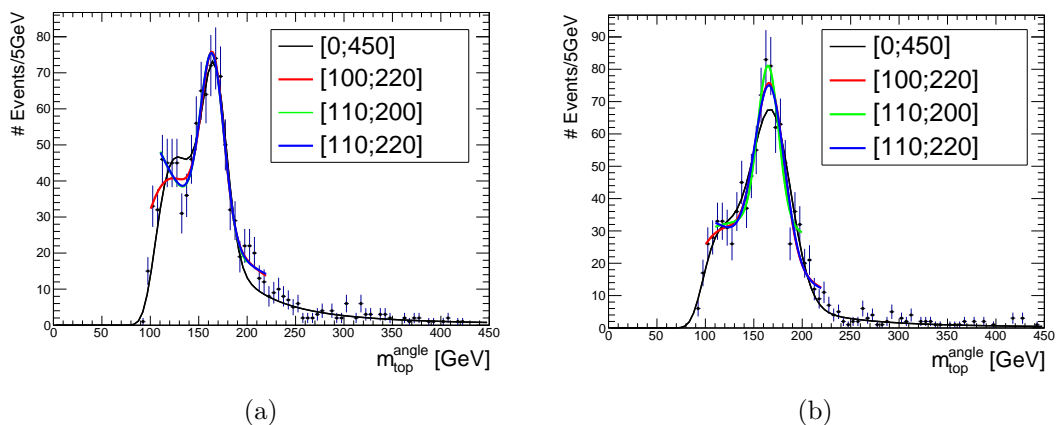


Figure 62: Examples of fits of a Landau+Gauss function to $m_{\text{top}}^{\text{angle}}$ distributions in $p_{\text{T}} - \beta_z \gamma$ bins fitting different ranges of the distribution.

In Fig. 62a and Fig. 62b, the fit of the whole range indicated by the black line has obvious difficulties to fit the steep slope at low masses. As it is required to fit at the same time the steep slope at low top masses and the slow decline at high masses and one peak, it is difficult for the function to fit all features of the distribution satisfactory at the same time and consequently, the distribution is not fitted very well.

Meanwhile, if the fit range is too small, as indicated by the green fit function in Fig. 62, the slow decline at large masses cannot be fit with a sufficient precision. This case is demonstrated in Fig. 62b.

If, on the other hand, the fit range extends too much to low masses, the fit is required to fit the steep slope and therefore, in many cases as for example in 62b and Fig. 62a, the Landau peak is not fitted well.

The blue function fitting the distribution in an interval of [110;220] GeV is the best trade-off in this case. The function extends sufficiently to low mass ranges but not too far while also describing to a good extent the high mass range important for the Gaussian fit.

The analysis is performed as already described in section 9.5: the sample is divided into p_{T} -bins and each of these p_{T} -bins is subsequently divided into bins of $\beta_z \gamma$. The $m_{\text{top}}^{\text{angle}}$ -distribution of each sub-bin is fitted with a combination of a Landau and Gauss function within the ideal fit range such that the Landau peak fits the combinatorial background while the Gauss peak position should be in the range of the top quark mass. An example of the resulting distribution of $m_{\text{top, angle}}^{\text{Gauss peak}}$ as a function of $\text{ASinh}(\beta_z \gamma)$ can be seen in Fig. 63 on the left, and of the extrapolated value of $m_{\text{top, angle}}^{\text{Gauss peak}}$ to $\beta_z \gamma = 0$ as a function of p_{T} is shown on the right panel of Fig. 63.

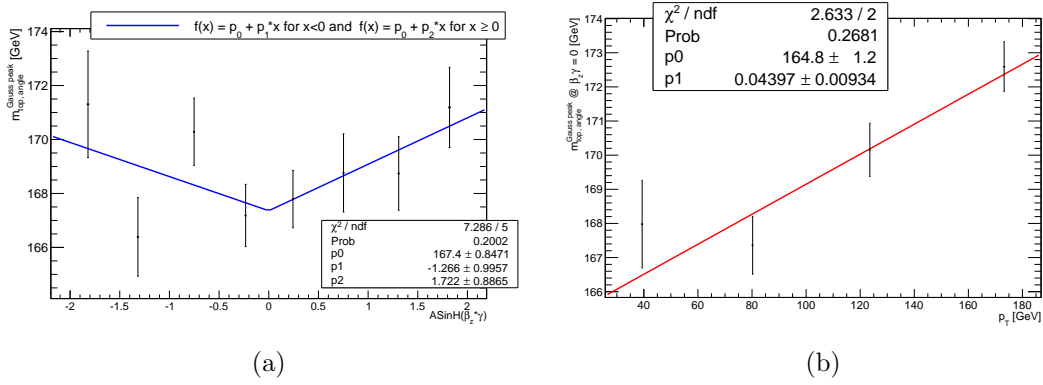


Figure 63: Left panel: example plot of an extrapolation of the $m_{\text{top, angle}}^{\text{Gauss peak}}$ estimator to $\beta_z \gamma = 0$. Right panel: extrapolation to $p_T = 0$ using the $m_{\text{top}}^{\text{MC}} = 172.5$ GeV sample.

As a next step, it is investigated, whether this method behaves better under a variation of the JSF than the method described in section 10. The impact on the top quark mass estimator $m_{\text{top, angle}}^{\text{Gauss peak}}$ if varying the JSF is demonstrated in Fig. 64:

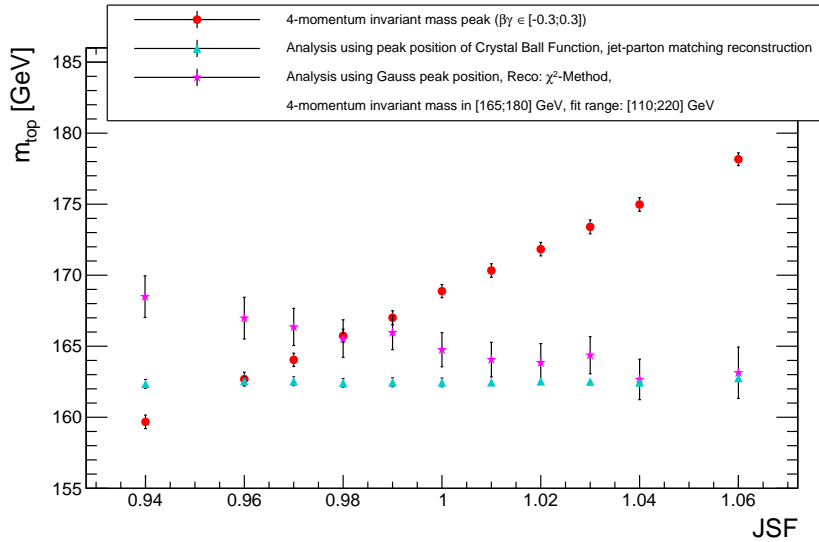


Figure 64: Investigation of the impact of a variation of the JSF on the $m_{\text{top, angle}}^{\text{Gauss peak}}$ estimator (represented by the purple stars). For comparison, the 4-momentum invariant mass peak (red dots) and the results of the angle method analysis if reconstructing the top pair using jet-parton matching (see section 9) (blue triangles) are shown.

The red dots show the 4-momentum invariant mass distribution peak of the reconstructed top quarks within a $\beta\gamma$ interval of $[-0.3;0.3]$ as a reference (see section 9.2).

The blue triangles indicate the case for the extrapolated $m_{\text{top, angle}}^{\text{peak}}$ -estimator using jet-parton matching as $t\bar{t}$ -reconstruction algorithm (section 9.7). The result obtained for the case of the new, constrained χ^2 reconstruction algorithm and an analysis using the peak position of the Gaussian is indicated by the purple stars.

Although the JSF-dependence is smaller than if using the 4-momentum invariant mass peak, the $m_{\text{top, angle}}^{\text{Gauss peak}}$ estimator shows some dependence on the JSF, significantly more than in case of the analysis method using jet-parton matching and Crystal Ball parametrization which is absent of influence of the combinatorial background (see section 9).

As demonstrated in section 9, the signal without the combinatorial background is approximately Gaussian-shaped¹⁹. The idea therefore was to fit that signal with a Gaussian and the combinatorial background with a Landau function as the contribution of the combinatorial background seems to be Landau-shaped. This point is underlined by Fig. 61.

But in the Gauss peak, there might be as well a contribution by the combinatorial background and vice versa, so Landau and Gauss functions are to some degree correlated. Moreover, the restriction of the fit range might as well lead to a distortion of the Gaussian and the Landau function. Due to the large slope at the lower end of the distribution and the fit range restriction, the peak of the Landau might be shifted and therefore change the Gaussian function.

This assumption can be checked by varying the fit range for example by taking into account the whole range in the fit of the Landau+Gauss function to the $m_{\text{top}}^{\text{angle}}$ -distribution. The resulting JSF-dependence can be seen in Fig. 65. The purple stars show as a reference the results obtained with a restricted fit range and the blue crosses show the results when taking into account the whole distribution range in the fit.

¹⁹The distribution was parametrized by a Crystal Ball function, which is mostly a Gaussian, see appendix A.

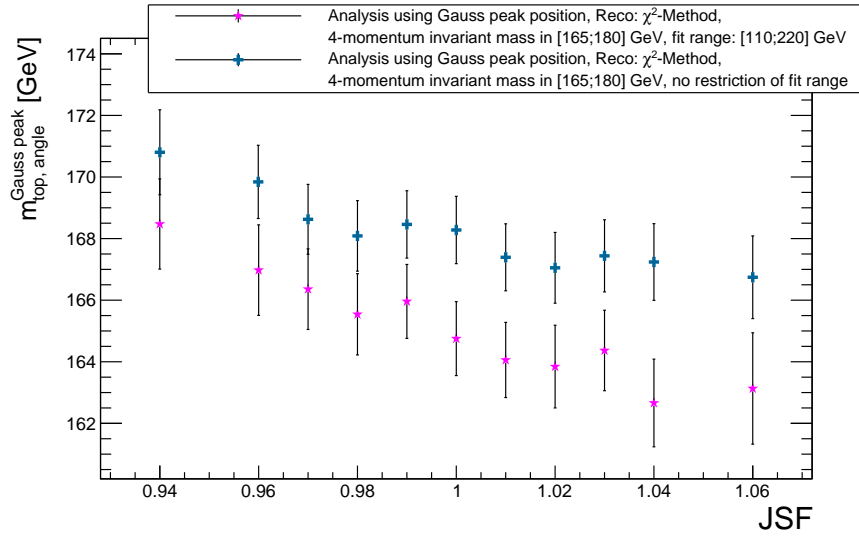


Figure 65: Investigation of the impact of the restriction on the fit range on the JSF dependence of the $m_{\text{top, angle}}^{\text{Gauss peak}}$ estimator. The purple stars show the results if restricting the fit range and the blue crosses demonstrate the results if not restricting the fit range of the Landau+Gauss function.

According to Fig. 65 a change in the fit range does not cause significant changes concerning the JSF dependence: Both distributions show a similar slope and are shifted with respect to each other but absolute values do not matter.

In order to check whether the dependence on the JSF has improved with this approach compared to the approach discussed in section 10 (weighted peaks position), the systematic uncertainties introduced by the JSF are compared. A linear function is fitted (see Fig. 66) to the extrapolated top quark mass estimator as a function of the JSF and an uncertainty on the JSF of 3% is assumed (see section 10.4).

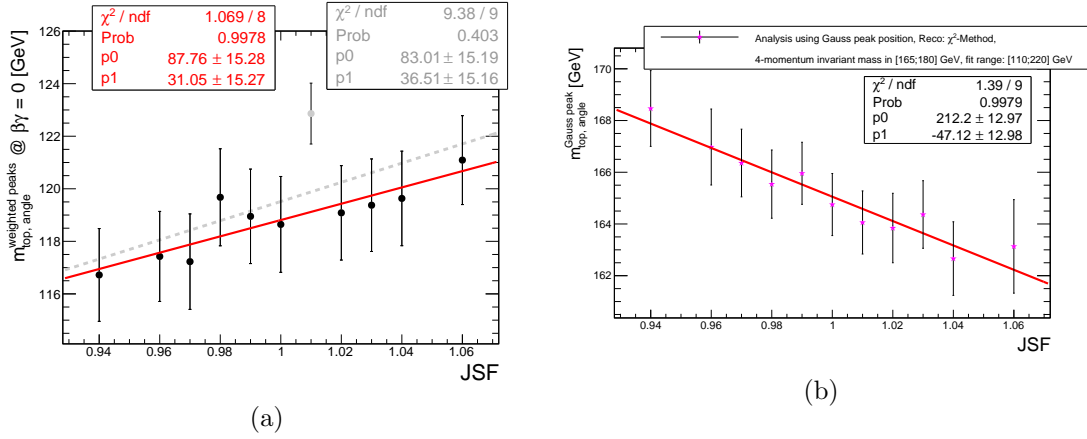


Figure 66: Comparison of the JSF dependence of the $m_{\text{top, angle}}^{\text{weighted peaks}}$ estimator (left panel) to the JSF dependence of the $m_{\text{top, angle}}^{\text{Gauss peak}}$ estimator (right panel).

The systematic uncertainty of the extrapolated estimator due to the uncertainty on the JSF can thus be calculated using:

$$\Delta m_{\text{top, angle}}^{\text{est.}} = \Delta p1 \cdot 0.03 \quad (43)$$

where p1 is the slope of the fit functions of Fig. 66. It must be considered that the central values of the two measured top quark mass estimators are very different, therefore, the relative systematic uncertainty $\frac{\Delta m_{\text{top, angle}}^{\text{est.}}}{m_{\text{top, angle}}^{\text{est.}}} @ (\text{JSF} = 1)$ is calculated. Resulting values for $\frac{\Delta m_{\text{top, angle}}^{\text{est.}}}{m_{\text{top, angle}}^{\text{est.}}} @ (\text{JSF} = 1)$ are calculated to $\frac{\Delta m_{\text{top, angle}}^{\text{weighted peaks}}}{m_{\text{top, angle}}^{\text{weighted peaks}}} (@ \text{JSF} = 1) = 0.8\%$ and

$\frac{\Delta m_{\text{top, angle}}^{\text{Gauss peak}}}{m_{\text{top, angle}}^{\text{Gauss peak}}} (@ \text{JSF} = 1) = 0.9\%$. These results stress that the JSF dependence of the estimators is indeed very small and similar in both cases.

Fig. 64 indicates that the dependence is still larger with respect to the results obtained with the analysis using jet-parton matching reconstruction. In the following, the influence of the 4-momentum invariant mass constraint in the χ^2 - $t\bar{t}$ reconstruction algorithm in the JSF dependence is evaluated. JSF variation studies are performed on the $m_{\text{top, angle}}^{\text{Gauss peak}}$ estimator but this time, the top pair is reconstructed without setting any restriction on the 4-momentum invariant mass of the reconstructed hadronically decaying top quark. Thus, the fraction of combinatorial background is the same as in the analysis in section 10. That way, the influence of the combinatorial background in the top quark mass estimator $m_{\text{top, angle}}^{\text{weighted peaks}}$ can also be examined.

The orange diamonds in Fig. 67, left panel, demonstrate, that the JSF dependence is slightly decreased when using the unconstrained χ^2 -reconstruction algorithm in case of the Gauss peak estimator with respect to the same analysis but with using the constrained χ^2 -reconstruction algorithm (purple stars). In comparison, the top quark mass measured with the peak position of the Crystal Ball function and with a jet-parton

matching reconstruction (blue triangles) is shown. It is obvious from Fig. 67 that the JSF dependence is smallest when there is no contribution of combinatorial background. In order to evaluate the JSF-dependence, again a linear function is fitted to the data in Fig. 67 on the right.

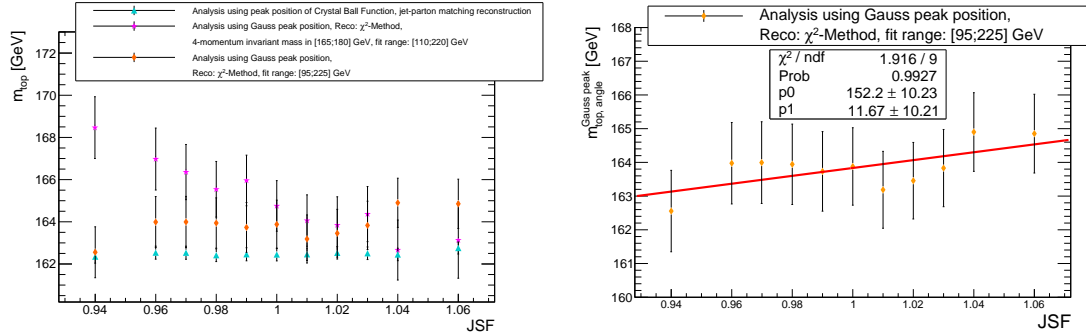


Figure 67: Left panel: Comparison of the JSF dependence of the $m_{\text{top}}^{\text{angle}}$ estimator using the jet-parton-matching-top-pair-reconstruction algorithm (blue triangles), the $m_{\text{top, angle}}^{\text{Gauss peak}}$ estimator without (orange diamonds) and with a constraint (purple stars) on the 4-momentum invariant mass of the hadronically decaying top quark. Right panel: evaluation of the JSF-dependence of the $m_{\text{top, angle}}^{\text{Gauss peak}}$ estimator for the case of the unconstrained χ^2 -reconstruction algorithm.

A calculation of the uncertainty introduced by the JSF using an average uncertainty on the JSF of 3% yields a result 0.2%. This shows, that indeed, the increased dependence on the JSF of the weighted peaks estimator $m_{\text{top, angle}}^{\text{weighted peaks}}$ is introduced by including the combinatorial background in the estimator which is sensitive to the jet energy scale. Moreover, the constraint on the 4-momentum invariant mass of the reconstructed top quark introduces also additional JSF-dependence.

Concluding this section, extracting the Gauss peak position of the $m_{\text{top}}^{\text{angle}}$ -estimator distribution and reconstructing the top quark without requiring any constraint on the top quark 4-momentum invariant mass, yields the result the least dependent on the JSF.

12. Conclusion and Outlook

Monte-Carlo studies showed that the top quark mass is indeed affected very little, to a degree of less than 200 MeV, by a variation of the jet energy scale according to Monte-Carlo samples simulating collisions at a center-of-mass energy of 8 TeV.

Also, first feasibility studies were made taking into account combinatorial background. Two examples for possible estimators considering combinatorial background have been examined: In the construction of the $m_{\text{top, angle}}^{\text{Gauss peak}}$ estimator, the combinatorial background is totally neglected while the $m_{\text{top, angle}}^{\text{weighted peaks}}$ estimator includes information on the signal and the combinatorial background weighted with the relative integrals. But, due to the large fraction of combinatorial background, latter enters with a very large weight. An estimator which depends to a much smaller degree on the combinatorial background is necessary.

In fact, in order to construct a suitable estimator, studies of the correlation of the combinatorial background and the signal have to be performed. First studies on the correlation of signal and background within the scope of this thesis turned out to be largely insignificant due to lack of statistics in the samples with $m_{\text{top}}^{\text{MC}} \neq 172.5 \text{ GeV}$. The knowledge of the signal to background correlation would help to construct a suitable estimator with regard to which degree the combinatorial background needs to be included in the estimator.

Simplified studies on the JSF-dependence of the $m_{\text{top, angle}}^{\text{Gauss peak}}$ estimator leads to the assumption of a systematic uncertainty due to variations of the JSF of about 0.2% while the $m_{\text{top, angle}}^{\text{weighted peaks}}$ estimator which considers the combinatorial background shows a larger sensitivity to the uncertainty on the jet energy scale.

As next steps, physics background must be considered in the analysis and the impact of a variation of the b-jet scale factor, a supplementary factor multiplied to the b-jet 4-momenta accounting for supplementary energy and momentum measurement uncertainties concerning b-jets, has to be examined. The calibration of the angle method needs to be redone including these components and then, the estimator could be applied on data.

After the long shut-down LS1 of the LHC, the LHC restarts in 2015 with an increased center-of-mass energy and increased luminosity resulting in larger $t\bar{t}$ production cross sections meaning larger data samples. In fact, the cross section of top quark processes will increase by a factor of 2.5 while physics background processes will increase by a factor of less than 2 [68]. More detailed studies which fail now due to lack of statistics could be carried out with larger data samples. With these prospects, pursuing this measurement method will yield promising results.

A. The Crystal Ball Function

The Crystal Ball function is an asymmetric function which consists of a Gaussian function and a power-law tail. In this thesis, the Crystal Ball function is used to describe asymmetric peaked distributions with one slowly declining tail. The Crystal Ball function is parametrized as follows [69], [70]:

$$f(x, \alpha, n, \bar{x}, \sigma) = \begin{cases} N \cdot \exp\left(-\frac{(x-\bar{x})^2}{2\sigma^2}\right) & \text{for } \frac{x-\bar{x}}{\sigma} > -\alpha \\ N \cdot \frac{\left(\frac{n}{|\alpha|}\right)^n \cdot \exp\left(-\frac{|\alpha|^2}{2}\right)}{\left(\frac{n}{|\alpha|} - |\alpha| - \frac{x-\bar{x}}{\sigma}\right)^n} & \text{for } \frac{x-\bar{x}}{\sigma} \leq -\alpha \end{cases} \quad (44)$$

where \bar{x} is the peak position of the Gaussian, σ is the width of the Gaussian and N is its height. The parameter n describes the slope of the power law function and the parameter α determines the position of the transition between the Gaussian function and the power law function.

The function resulting of the parametrization of equation (A) can be seen in Fig. 68.

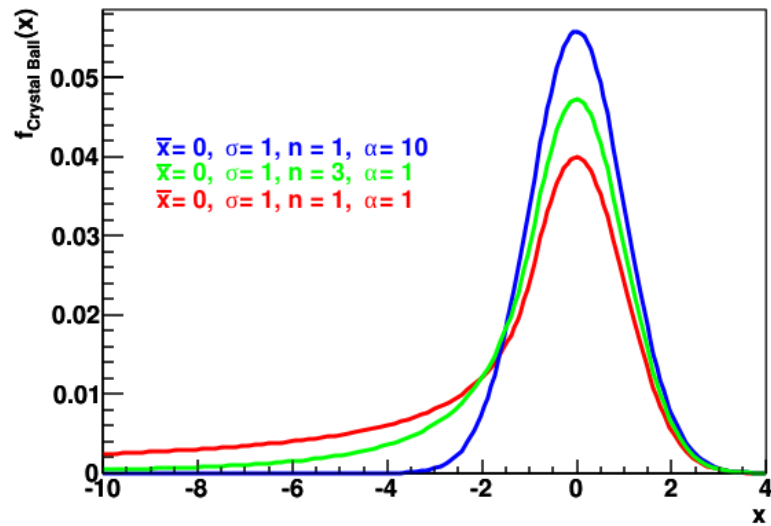


Figure 68: The Crystal Ball function shown for different parameter values, from [70].

B. The Lorentz-Transformation

The Lorentz-transformation which was applied to boost the top quark decay products into the top quark rest frame is of the following form [71]:

$$\Lambda_v = \begin{pmatrix} \gamma & -\gamma \cdot \frac{v_1}{c} & -\gamma \cdot \frac{v_2}{c} & -\gamma \cdot \frac{v_3}{c} \\ -\gamma \cdot \frac{v_1}{c} & & & \\ -\gamma \cdot \frac{v_2}{c} & & \delta_{ij} + \frac{v_i \cdot v_j \cdot (\gamma - 1)}{v^2} & \\ -\gamma \cdot \frac{v_3}{c} & & & \end{pmatrix}$$

The Lorentz-transformation can be performed separately in each direction, they are orthogonal and independent in the 3 spatial directions which is required due to the equivalence of all reference frames. This justifies the 2-step analysis of a separate treatment of the longitudinal and transverse component of the estimator: The uncertainties on the jet energy measurement which cause a Lorentz-transformation to the incorrect frame are corrected separately in transverse and longitudinal direction by extrapolation. The requirement of this approach is the possibility to decompose the Lorentz-transformation into components.

Hiermit erkläre ich, die vorliegende Arbeit selbständig verfasst zu haben und keine anderen als die in der Arbeit angegebenen Quellen und Hilfsmittel benutzt zu haben.

München, 30.03.2015

Datum,

Unterschrift

Acknowledgements

Am Ende möchte ich mich bei all den Leuten bedanken, die mich während meiner Masterarbeit so hervorragend unterstützt haben.

- Ganz herzlich möchte ich mich bei **Prof. Dr. Otmar Biebel** bedanken für seine Unterstützung und die Betreuung der Arbeit, dass er bei Fragen immer zur Verfügung stand und sich stets Zeit genommen hat. Danke für die vielen hilfreichen Ratschläge und Diskussionen, die die Arbeit maßgeblich vorangebracht haben.
- Vielen Dank an **Prof. Dr. Dorothee Schaile** für die Möglichkeit, die Masterarbeit an Ihrem Lehrstuhl anzufertigen und den hilfreichen Input bei Vorträgen in den Gruppenseminaren.
- Mein besonderer Dank gilt auch **Dr. Stefanie Adomeit** für die gute und kompetente Betreuung der Arbeit und die zahlreichen nützlichen Ratschläge und Hinweise.
- Bei meinem Bürokollegen **Michael Bender** möchte ich mich für die Unterstützung bei Programmier- und Softwarefragen bedanken und vor allem für das gute Arbeitsklima im Büro.
- **Christopher Unverdorben** hat mir die Monte-Carlo samples zur Verfügung gestellt und mir sämtliche Fragen zu den Samples beantwortet und mir zahlreiche Hinweise gegeben. Herzlichen Dank dafür!
- Herzlichen Dank nochmals an alle Mitglieder der **Topgruppe** des Lehrstuhls für die hilfreichen Ratschläge und Hinweise zur Analyse.
- Bedanken möchte ich mich auch bei **Katharina Behr** für die hervorragende Vorarbeit der Analyse in ihrer Masterarbeit und dafür, dass sie stets für Fragen zu ihrer Masterarbeit zur Verfügung stand.
- **Frau Elke Grimm-Zeidler** möchte ich für ihre kompetente und freundliche Hilfe bei administrativen Angelegenheiten danken.
- Herzlichen Dank an **alle Mitarbeiter und Studenten des Lehrstuhls** für das gute Arbeitsklima und die unterhaltsamen Mittagspausen und Kaffeepausen!
- Ganz besonderer Dank gilt **meinen Eltern Christina und Norbert Burger** dafür, dass sie in jeder Situation für mich da waren und mich während des Studiums und auch in allen anderen Situationen unterstützt haben und besonders für ihre Liebe und stetigen Ermunterungen!

References

References

- [1] Frank Fiedler. Precision Measurements of the Top Quark Mass. 2010. Comments: Habilitation thesis at Munich University (2007).
- [2] Fedor Bezrukov and Mikhail Shaposhnikov. Why should we care about the top quark Yukawa coupling? Technical Report arXiv:1411.1923. CERN-PH-TH-2014-218, Nov 2014.
- [3] First combination of Tevatron and LHC measurements of the top-quark mass. Technical Report arXiv:1403.4427. ATLAS-CONF-2014-008. CDF-NOTE-11071. CMS-PAS-TOP-13-014. D0-NOTE-6416, CERN, Geneva, Mar 2014.
- [4] Donald Hill Perkins. *Introduction to high-energy physics; 4th ed.* Cambridge Univ. Press, Cambridge, 2000.
- [5] David J Griffiths. *Introduction to elementary particles; 2nd rev. version.* Physics textbook. Wiley, New York, NY, 2008.
- [6] Dorothee Schaile. Script to the lecture "Advanced Particle Physics" at the LMU, SoSe 2013.
- [7] Picture taken from: <https://indico.cern.ch/event/316980/material/slides/1.pdf>, Lecture within the scope of the CERN Summer Student Programme, Dr. T. Shears.
- [8] K.A. Olive et al. (Particle Data Group). *Chin. Phys. C*, (38, 090001), 2014.
- [9] C.S. Wu et al. Experimental Test of Parity Conservation in Beta Decay. *Phys. Rev.*, (105), February 1957.
- [10] Otmar Biebel. Standardmodell der Teilchenphysik und Erweiterungen, Summer term 2005. Lecture course at the LMU within the scope of the diploma program in physics.
- [11] Stefanie Adomeit. *Measurement of the top quark mass in the fully hadronic top antitop decay channel with the ATLAS detector.* PhD thesis, Ludwig-Maximilians-Universitaet Muenchen, July 2013.
- [12] Daniel Wicke. Properties of the Top Quark. *Eur.Phys.J.*, C71:1627, 2011.
- [13] Joseph R. Incandela, Arnulf Quadt, Wolfgang Wagner, and Daniel Wicke. Status and Prospects of Top-Quark Physics. *Prog.Part.Nucl.Phys.*, 63:239–292, 2009.
- [14] Petra Haefner. Single Top Results by ATLAS and CMS. Technical Report ATL-PHYS-PROC-2012-019, CERN, Geneva, Jan 2012. Comments: Presented at the 2011 Hadron Collider Physics symposium (HCP-2011), Paris, France, November 14-18 2011.

- [15] The ATLAS collaboration. Measurement of jet shapes in top-quark pair events at $\sqrt{s} = 7$ TeV using the ATLAS detector. *Eur. Phys. J. C*, 73(arXiv:1307.5749. CERN-PH-EP-2013-067):2676. 20 p, Jul 2013.
- [16] E. Cogneras and D. Pallin. Top Mass measurement in the 2 b-tagged semileptonic $t\bar{t}$ channel. Technical Report ATL-PHYS-INT-2008-036-1. ATL-COM-PHYS-2008-044, CERN, Geneva, Apr 2008.
- [17] The CDF Collaboration. Measurement of the top quark mass from the leptons' p_T in the $t\bar{t} \rightarrow$ dilepton channel using b-tagging at 2.8 fb^{-1} , July 2009.
- [18] F Balli, G Compostella, G Cortiana, A Maier, R Nisius, and J Schwinding. Measurement of the Top Quark Mass in the $t\bar{t} \rightarrow$ lepton+jets and $t\bar{t} \rightarrow$ di-lepton channels from $\sqrt{s} = 7$ TeV ATLAS Data. Technical Report ATL-COM-PHYS-2014-900, CERN, Geneva, Jul 2014.
- [19] G. Aad et al. The ATLAS Experiment at the CERN Large Hadron Collider. *JINST*, 3:S08003, 2008.
- [20] Picture taken from http://lhc-beam-beam.web.cern.ch/lhc-beam-beam/bb-meeting/CAS/CAS2014_Chavannes/0606052-A4-at-144-dpi.jpg; January 2015.
- [21] The accelerator complex, November 2014. <http://home.web.cern.ch/about/accelerators>.
- [22] Lucio Rossi. The longest journey: the lhc dipoles arrive on time, October 2006. Published in the CERN Courier; <http://cerncourier.com/cws/article/cern/29723>.
- [23] Lyndon R. Evans. The Large Hadron Collider project. Sep 1996. LHC-Project-Report-53.
- [24] LHC yields data rapidly at new collision energy of 8 TeV. *CERN Courier*, April 2012. <http://cerncourier.com/cws/article/cern/49334>.
- [25] Cian O'Lunaigh. CERN announces LHC restart schedule, June 2014. <http://home.web.cern.ch/about/updates/2014/06/cern-announces-lhc-restart-schedule>.
- [26] Matthias Schott and Monica Dunford. Review of single vector boson production in pp collisions at $\sqrt{s} = 7$ TeV. *Eur.Phys.J.*, C74:2916, 2014.
- [27] Picture taken from: <http://en.wikipedia.org/wiki/Pseudorapidity>; January 2015.
- [28] Vasiliki A. Mitsou. The ATLAS transition radiation tracker. pages 497–501, Nov 2003. In: 8th Conference on Astroparticle, Particle, Space Physics, Detectors and Medical Physics Applications, Como, Italy, 6 - 11 Oct 2003.
- [29] Akiya Miyamoto, Marcel Stanitzki, Harry Weerts, and Lucie Linssen. Physics and Detectors at CLIC: CLIC Conceptual Design Report. Technical Report arXiv:1202.5940, Geneva, 2012. Comments: 257 p, published as CERN Yellow Report CERN-2012-003.

- [30] C. Joram. Academic training lecture for postgraduate students: Particle detectors - principles and techniques (4/5) calorimetry, April 2005. <http://indico.cern.ch/event/a042932/>.
- [31] P. Jenni. The ATLAS experiment entering operation: Overview, motivation and status. Technical Report ATL-GEN-PROC-2009-003. ATL-COM-GEN-2009-003, CERN, Geneva, 2009.
- [32] Bryan Dahmes. Trigger For LHC Physics (Lecture of the CERN Summer Student Programme 2014), July 2014.
- [33] Sebastian Wahrmund, Arno Straessner, and Dominik Stöckinger. *Underlying event studies using calorimeter jets with the ATLAS detector at LHC*. PhD thesis, TU Dresden, 2010. Presented on 15 Jan 2010.
- [34] Picture taken from (talk by Sven Menke, Max-Planck-Institute for physics, Munich): <https://www.mppmu.mpg.de/~menke/pdf/boost2013.pdf>.
- [35] The ATLAS collaboration. Pile-up subtraction and suppression for jets in ATLAS. Technical Report ATLAS-CONF-2013-083, CERN, Geneva, Aug 2013.
- [36] John Alison and I. J. Kroll. *The Road to Discovery: Detector Alignment, Electron Identification, Particle Misidentification, WW Physics, and the Discovery of the Higgs Boson*. PhD thesis, Pennsylvania U., Pennsylvania U., Dec 2012. Presented 08 Nov 2012.
- [37] The ATLAS Collaboration. Electron reconstruction and identification efficiency measurements with the ATLAS detector using the 2011 LHC proton-proton collision data. *Eur. Phys. J. C*, (arXiv:1404.2240. CERN-PH-EP-2014-040):74. 38 p, Apr 2014.
- [38] Acharya et al. Object selection and calibration, background estimations and MC samples for top quark analyses using the full 2012 data set. Technical Report ATL-COM-PHYS-2013-1016, CERN, Geneva, Jul 2013.
- [39] B. Resende. Muon identification algorithms in ATLAS. Technical Report ATL-PHYS-PROC-2009-113, CERN, Geneva, Sep 2009.
- [40] R. Nicolaidou, L. Chevalier, S. Hassani, J.F. Laporte, E. Le Menedeu, et al. Muon identification procedure for the ATLAS detector at the LHC using Muonboy reconstruction package and tests of its performance using cosmic rays and single beam data. *J.Phys.Conf.Ser.*, 219:032052, 2010.
- [41] Georges Aad et al. Jet energy measurement and its systematic uncertainty in proton-proton collisions at $\sqrt{s} = 7$ TeV with the ATLAS detector. *Eur.Phys.J.*, C75(1):17, 2015.
- [42] Peter Loch (on behalf of the ATLAS Collaboration). Jet measurements in ATLAS. *Journal of Physics: Conference Series*, 323, 2011. http://iopscience.iop.org/1742-6596/323/1/012002/pdf/1742-6596_323_1_012002.pdf.

- [43] Matteo Cacciari, Gavin P Salam, and Gregory Soyez. The anti- k_t jet clustering algorithm. *J. High Energy Phys.*, 04(arXiv:0802.1189. LPTHE-07-03):063. 12 p, Feb 2008.
- [44] G. Cortiana. Physik der Schweren Quarks, Lecture at the Ludwig-Maximilians-Universitaet Muenchen, Summer Term 2013, 2013. http://www.physik.uni-muenchen.de/lehre/vorlesungen/sose_13/Physik_Der_Schweren_Quarks/index.html.
- [45] Jet energy scale and its systematic uncertainty in proton-proton collisions at $\sqrt{s}=7$ TeV with ATLAS 2011 data. Technical Report ATLAS-CONF-2013-004, CERN, Geneva, Jan 2013.
- [46] ATLAS Twiki pages. Flavour tagging calibration results in 2014, February 2015. ATLAS Twiki pages, <https://twiki.cern.ch/twiki/bin/viewauth/AtlasProtected/BTagCalib2014>.
- [47] ATLAS Collaboration. Commissioning of the ATLAS high-performance b-tagging algorithms in the 7 TeV collision data. Technical Report ATLAS-CONF-2011-102, CERN, Geneva, Jul 2011.
- [48] M Testa. Refined reconstruction and calibration of the missing transverse energy in the ATLAS detector. Technical Report ATL-PHYS-PROC-2012-026, CERN, Geneva, Jan 2012.
- [49] Joao Pequenao and Paul Schaffner. An computer generated image representing how ATLAS detects particles. Jan 2013.
- [50] T Sjöstrand, S Mrenna, and P Z Skands. PYTHIA 6.4 Physics and Manual. *J. High Energy Phys.*, 05(hep-ph/0603175. FERMILAB-Pub-2006-052-CD-T. LUTP-2006-13):026. 570 p, Mar 2006.
- [51] ATLAS Top Working Group. TopMC12DiTopSamples, March 2015. <https://twiki.cern.ch/twiki/bin/viewauth/AtlasProtected/TopMC12DiTopSamples>.
- [52] Stefano Frixione, Paolo Nason, and Giovanni Ridolfi. A Positive-Weight Next-to-Leading-Order Monte Carlo for Heavy Flavour Hadroproduction. *J. High Energy Phys.*, 09(arXiv:0707.3088. BICOCCA-FT-07-12. GEF-TH-19-2007):126. 18 p, Jul 2007.
- [53] GEANT4 web, March 2015. <https://twiki.cern.ch/twiki/bin/view/Geant4/WebHome>.
- [54] Rudolf K. Bock. K-factor, April 1998. <http://rd11.web.cern.ch/RD11/rkb/PH14pp/node92.html>, downloaded in March 2015.
- [55] Christopher Unverdorben. *Measurement of the CKM matrix element V_{ts}* . PhD thesis, Ludwig-Maximilians-Universitaet Muenchen, March 2015.
- [56] ATLAS Top Working Group. TopCommonObjects, February 2015. ATLAS Twiki pages, <https://twiki.cern.ch/twiki/bin/view/AtlasProtected/TopCommonObjects>.

- [57] Atlas muon combined performance guidelines for analyses of 2012 data, February 2015. <https://twiki.cern.ch/twiki/bin/viewauth/AtlasProtected/MCPAnalysisGuidelinesData2012>.
- [58] Janna Katharina Behr. Measurement of the Top-Quark Mass in the Semileptonic Decay Channel at the ATLAS Experiment. diploma thesis, Ludwig-Maximilians-Universitaet Muenchen, Maerz 2012.
- [59] Musiol Mühlig Bronstein, Semendjajew. *Taschenbuch der Mathematik*. Verlag Harri Deutsch, 7 edition, 2008.
- [60] Eric W. Weisstein. Triangle median, February 2015. From MathWorld—A Wolfram Web Resource. <http://mathworld.wolfram.com/TriangleMedian.html>.
- [61] Martin Kerscher. Skript zur Numerischen Mathematik fuer Studierende der Physik, SoSe 2014. <http://www.mathematik.uni-muenchen.de/~kerscher/vorlesungen/numeriksose14/skript/>.
- [62] Thomas McCarthy. Top quark mass measurement in the all-hadronic $t\bar{t}$ channel @ $\sqrt{s} = 8$ tev, February 7th 2014. Analysis Update presented in the ATLAS top mass group meeting on the 7th of February 2014.
- [63] Particle Data Group. Particle physics booklet, July 2008. Website: <http://pdg.lbl.gov>.
- [64] R. Moles-Valls and S. Marti-Garcia. Measurement of the top-quark mass with the Global χ^2 method. Technical Report ATL-COM-PHYS-2013-443, CERN, Geneva, Apr 2013.
- [65] D. Segransan. Covariance and Correlation. Lecture notes to a statistics lecture of the University of Geneva, downloaded in February 2015, http://www.unige.ch/sciences/astro/files/5413/8971/4090/2_Segransan_StatClassUnige.pdf.
- [66] Roger Barlow. Application of the Bootstrap resampling technique to particle physics experiments. *Manchester Particle Physics*, 4(99), April 2000.
- [67] Stefan Guindon. *A Top Quark Mass Measurement Using the Stabilized R_{32} Variable with the ATLAS Detector*. PhD thesis, Georg-August Universitaet Goettingen, July 2012.
- [68] Thorsten Chwalek. Top-Quark-Physik - von der Entdeckung am Tevatron zu Praezisionsmessungen am LHC, March 2015. Talk given at the spring conference of the DPG (Deutsche Physikalische Gesellschaft) of 2015 in Wuppertal.
- [69] Fergus Wilson Adrian Bevan. AFit User Guide, December 2010. From: <http://pprc.qmul.ac.uk/~bevan/afit/afit.pdf>.
- [70] Crystal Ball function, December 2013. From: http://en.wikipedia.org/wiki/Crystal_Ball_function.
- [71] Torsten Fliessbach. *Mechanik - Lehrbuch zur Theoretischen Physik 1*. Spektrum Akademischer Verlag Heidelberg, 6 edition, 2009.